Phase Transitions and Ordering of Microphase Separated Block Copolymer Nanostructures in Electric Fields

Von der Fakultät für Mathematik, Informatik und Naturwissenschaften der RWTH Aachen University zur Erlangung des akademischen Grades eines Doktors der Naturwissenschaften genehmigte Dissertation

vorgelegt von M.Sc.
Christine Claudia Kathrein
aus Neuss, Deutschland

Berichter: Prof. Dr. Alexander Böker
Prof. Dr. Andrij Pich

Tag der mündlichen Prüfung: 22.04.2016
Diese Dissertation ist auf den Internetseiten der Hochschulbibliothek online verfügbar.

Acknowledgments

Zahlreiche hilfsbereite Personen haben zur Vervollständigung dieser Arbeit beigetragen. Mein besonderer Dank gebührt Prof. Dr. Alexander Böker, sowohl für die Möglichkeit an spannenden Themen in seinem Arbeitskreis zu forschen, als auch für den Freiraum eigene Ideen umzusetzen, seine stete Bereitschaft mich zu unterstützen, wenn Herausforderungen zu meistern waren, für die Chance im Rahmen der Promotion ins Ausland zu gehen und seine vertrauensvolle und gerechte Betreuungsweise. Prof. Dr. Caroline A. Ross bin ich dankbar für die Zeit, die ich am Massachusetts Institute of Technology verbringen durfte, die vielen hilfreichen Diskussionen und die herzliche Aufnahme in ihrer Gruppe. Prof. Dr. Andrij Pich danke ich für die Prüfung der Arbeit. PD Dr. Larisa Tsarkova möchte ich ebenfalls für die vielen Gespräche danken, ihre stete Hilfsbereitschaft bei Fragen jeder Art, und die vielen guten Tipps in Bezug auf Forschung und Veröffentlichungen. Besonderer Dank gilt auch meinen Stipendien Gebern: dem Fonds der chemischen Industrie und dem Deutschen Akademischen Austauschdienst (DAAD) für die Finanzierung der Projekte. Danke an Werner Heckler für die Ausleihe des Exicor 150AT und die Einweisung in die Doppelbrechungsmessungen. Christian Pester danke ich für die Hilfe bei der Einarbeitung in die Experimente zu den Bulk Messungen. Maike Jung, Dr. Mathias Meyer und Prof. Dr. Wim de Jeu danke ich für die Hilfe bei der Auswertung und Interpretation der SAXS Daten. Maike Jung danke ich ebenfalls für die schöne gemeinsame Zeit. Des weiteren möchte ich noch unseren lokalen Ansprechpartnern am ESRF Dr. Peter Bösecke und Dr. Johannes Möller für ihre Hilfe bei den Synchrotron SAXS Messungen danken. Danke an Wubin Bai für die Hilfe bei der Einarbeitung in die Block copolymer Dünnfilm Projekte, seine stete Hilfsbereitschaft und die lustige gemeinsame Zeit am MIT. Ebenfalls möchte ich John Linkhorst danken für die Hilfe bei Linux und anderen Computer Problemen. Guido Kirf, Bernd Huppertz und Christoph Herren danke ich für den Bau der Probenzellen und der Temperaturregelung, und das Schreiben der Labview Software. James Dayley, Elisabeth Shaw, Dr. Billy Putnam, Dr. Adam McCaughan und Ryan O'Keefe danke ich für die Einführung in unterschiedliche Messgeräte am MIT. Meiner besten Freundin Mai-Thi Nguyen-Kim danke ich für die schöne gemeinsame Zeit, sowohl innerhalb als auch auerhalb des Instituts und dafür, dass wir uns in schwierigen Zeiten immer wieder gegenseitig motivieren konnten. Weitere Menschen, die meine Zeit sowohl an der RWTH als auch am MIT,

vor allem in den Mittags- und Kaffeepausen bereicherten sind Dr. Enno Lage, Dr. Pin Ho , Dr. Ulrich Glebe, Lei Wu, Dr. Eduardo Martin und Christian Lewin, sowie die anderen Mitglieder der Arbeitskreise von Prof. Böker und Prof. Ross. Meinem Freund Mathias Schmieder danke ich für seine liebevolle Unterstützung und Motivation, und dafür dass er mir mit seiner entspannten Art geholfen hat auch in herausfordernden Situationen immer die Ruhe zu bewahren. Meiner Schwester Anne Kathrein danke ich für das Programmieren der Software, die eine schnellere Auswertung der SAXS Daten ermöglichte, sowie für ihre Unterstützung in sämtlichen Lebenslagen. Vor allem danke ich meinen Eltern Margret Kathrein und Dr. Hendrik Kathrein und dem Rest meiner Familie dafür, dass sie immer für mich da waren wenn ich ihre Hilfe benötigte, mich stets dabei unterstützten, meine Ziele zu erreichen und mich dazu ermutigten, auch schwierigere Herausforderungen anzupacken.

Contents

1. Introduction

Increasing miniaturization of electronic and data storage devices necessitates methods which enable large area structuring on a nanometer length scale at reasonable prices. Block copolymers (BCP) are prospective functional materials and promising candidates for soft matter nanotechnology due to their capability to readily self-assemble into highly ordered thermotropic or lyotropic phases on a length scale of 10 - 100 nm.

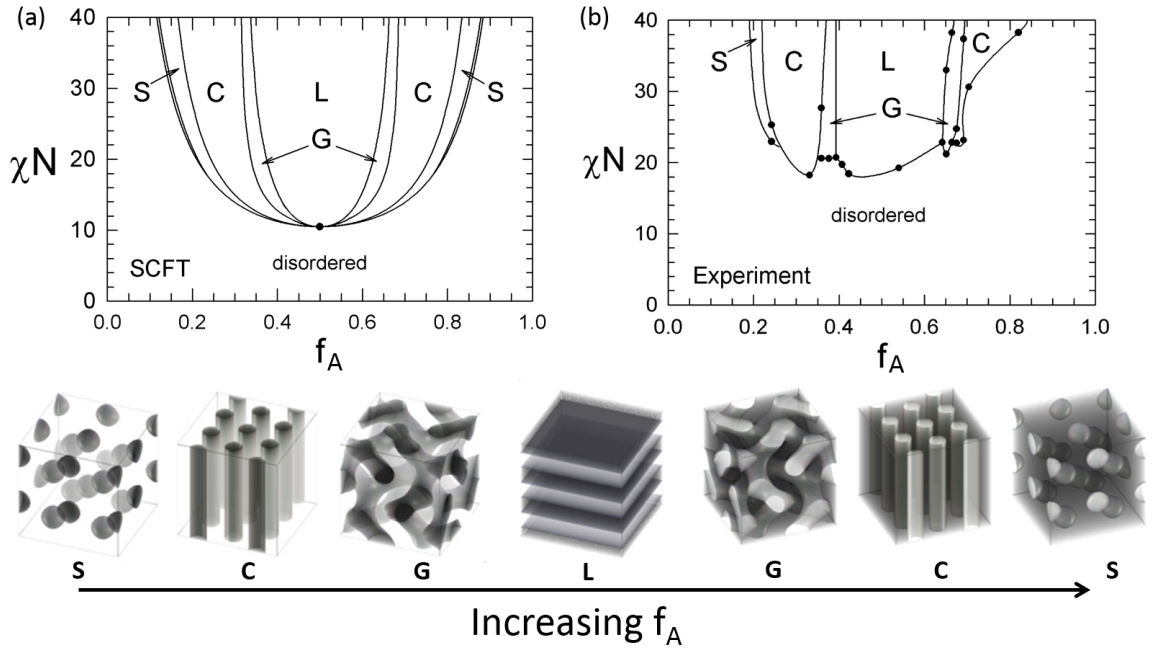

Figure 1.1.: (a) Theoretical phase diagram of AB diblock copolymers calculated by self-consistent mean-field theory [MB97] and (b) experimentally measured block copolymer phase diagram of polyisoprene-*block*-polystyrene [KFB*95]. The equilibrium morphologies in the different regions of the phase diagram are given below the image. The graphic was reprinted in modified form from http://chemeng.uwaterloo.ca/mwmatsen/research/mc.html and http://www.msri.org/publications/sgp/jim/models/copolymers/morphologies/main.html.

Figure 1.1 (a) displays the theoretical phase diagram of an AB diblock copolymer calculated by self-consistent field theory. Figure 1.1 (b) shows the experimental phase diagram of polyisoprene-*block*-polystyrene [KFB*95]. Depending on the product of the the Flory-Huggins interaction parameter and the degree of polymerization (χN), and the volume fractions of the individual blocks (f_A, f_B) a multitude of mesoscopic structures are producible [Lei80, BF90, LD95], rendering BCPs viable materials for lithographic patterning of nanostructures on a length scale beyond the resolution limits of conventional photolithography [KPH09, JHK*13]. The stability regions of the individual phases (sphere (S), cylinder (C), gyroid (G), lamellae (L), hexagonal perforated lamella (PL)) in dependency of χN and f_A are indicated in the diagram. A schematic of each microstructure is given below the phase diagrams.

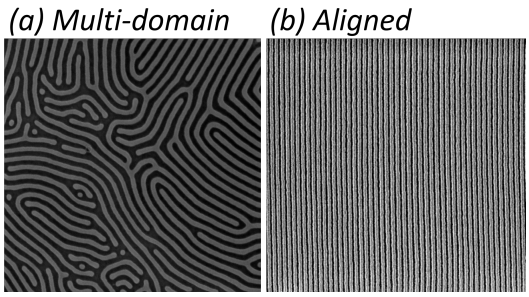

As shown in the image (a) to the left self-assembled block copolymer samples are commonly characterized by a multi-domain structure comprising grains whereby the correlation length of ordering merely amounts a few μm^2. The lack of long-range order is a key issue which needs to be addressed to facilitate the use of block copolymers in potential applications such as data storage, microelectronics, or semiconductors [SGR12]. Methods envisaged to obtain large area orientation of block copolymer patterns (image (b)) include the application of external stimuli such as shear forces [CKS*97, AWA*04], temperature gradients [BBD*07], solvent annealing [GR13, FEMK00, KHH*08], magnetic- [GMCO13, GPH05, TZOS07, MEO10] or electric fields [BEH*02b], as well as chemoepitaxy [RLM*99, KSS*03, CRP*03, RKD*08, DMS*06] and graphoepitaxy [BYJ*08, SYK10, CRT*03].

Benefits of electric field-induced orientation include that they can easily be integrated into electronic devices, are increasingly effective on diminishing length scales, and the rapid, stepwise tunability of field strength. Furthermore, substrate preparation procedures are less cumbersome and cheaper than in the case of chemo- and graphoepitaxy approaches. Additionally, phase transitions between various block copolymer microphases can be induced allowing structural tunability by simple stimuli application which is of fundamental interest. This thesis focuses on the analysis of long-range ordering and phase transitions induced by the application of electric fields. Experiments to Chapters 3-6 were conducted at the DWI - Leibniz Institut für Interaktive Materialien, RWTH Aachen University (Aachen, Germany) and at the ESRF (Grenoble, France) while the experiments to Chapter 7 and 8 were performed during a research internship in the group of Prof. Dr. Caroline A. Ross at the Materials Science and Engineering Department of

the Massachusetts Institute of Technology (MIT) (Cambridge, MA, USA).

Part I: Bulk Samples of Block copolymers

Bulk samples are considered to be close to thermodynamic equilibrium, as compared to thin films where additional effects induced by e.g. surface fields, annealing conditions or film thickness have to be taken into account. Their analysis gives deeper insights into the effects of electric field on the nanostructures since it enables the systematic variation of a single parameter at a time. Therefore, the first four chapters of this thesis deal with the bulk analysis of the effect of electric field on microphase separated diblock copolymer nanostructures.

In **Chapter** 3 we describe the setup developed in this thesis to use birefringence measurements as a supplementary method to synchrotron SAXS giving a general overview of the scope of this method including example measurements. Birefringence measurements are non-destructive and easily accessible facilitating a higher sample throughput and hence allowing time consuming measurements which was not feasible with the synchrotron SAXS measurements used before. Apart from transitions between ordered microphase separated phases and the disordered phase (order-disorder transition), we show that optical analysis also enables the assessment of transitions between different nanostructures (order-order transition) and electric field-induced block copolymer reorientation.

(i) The Analysis of Order-Disorder Transitions (ODT)

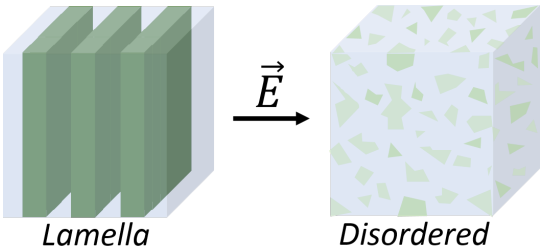

Experimentally, electric fields have been shown to induce mixing in concentrated solutions of polystyrene-*block*-polyisoprene in vicinity of the transition temperature between microphase separated and disordered phases (T_{ODT}) [SSSB09, SPR*13]. A schematic image of the transition is given to the left. Nonetheless, the unambiguous allocation of the cause of mixing was not possible to date considering that theoretical considerations contradict the experimental results [Tso09]. Therefore, part of this thesis focusses on explaining this observation which has been under debate for several decades. For the first time the effect of strong DC electric fields on the order-disorder transition temperature could be analyzed for various block copolymer systems as we report in **Chapter** 4. The developed setup described in **Chapter** 3 allowed to conduct these time consuming measurements and the systematic screening of the behavior in a large parameter window. The novelty of our findings is that we identify the parameters that evoke mixing of block copolymers when exposed to electric fields (the difference in dielectric permittivity $\Delta\epsilon$ between the block copolymer constituents and

the degree of polymerization (N)) and can hence theoretically explain the experimental results.

(ii) The Analysis of Order-Order Transitions (OOT)

Another phase transition focused on in this thesis is the electric-field-induced transition between a gyroid and a cylinder nanostructure as schematically shown in the image to the right. The gyroid morphology is a candidate for applications in three-dimensional photonic crystals, microporous systems, and nanoreactors [EUD*01, HTF97, ZFH*98]. Considering it's technical applications, the structural control over the gyroid morphology via electric fields is of great interest.

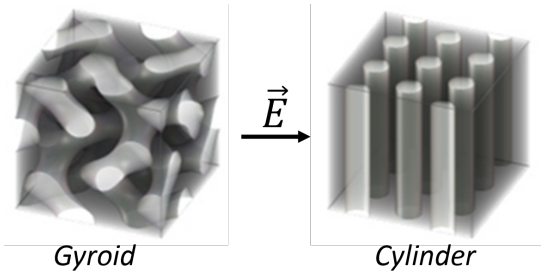

Through a detailed synchrotron SAXS study we could unveil the mechanisms of the electric-field-induced gyroid-to-cylinder transition and of the reformation of the gyroid phase after turning off the electric field which have not been reported to date. The detailed mechanistic study is given in **Chapter** 6. We show that the exploited mechanism is determined by temperature and electric field strength and resolve the conditions under which higher ordered gyroids could be obtained with the help of electric fields.

(iii) The Analysis of Electric Field-Induced Block copolymer Reorientation

Block copolymer nanoparticle composite materials have attracted much interest in the past decade. The combination of ordering on a nanometer length scale with various interesting properties associated with nanoparticles enables applications in e.g. catalysis [JBCM03], biomedical devices [KNP07], solar cells [HDA02] or photonic band gap materials [TGMB02, SHGC05]. However, few studies exist on how the behavior of block copolymers in the electric field is altered upon incorporation of nanoparticles.

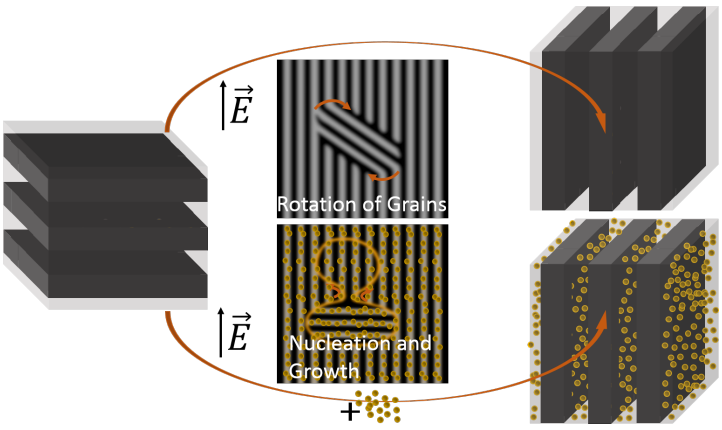

In **Chapter** 5 time- and temperature-resolved *in-situ* birefringence measurements were applied to analyze the effect of nanoparticles on the electric field-induced alignment of a microphase separated solution of polystyrene-*block*-polyisoprene in toluene. With our experiments we reveal that the incorporation of isoprene-confined CdSe quantum dots leads to an altered reorientation behavior. Particle loading lowers the order-

disorder transition temperature, and increases the defect density, favoring nucleation and growth as an alignment mechanism over rotation of grains. Furthermore, a novel method to analyze the temperature dependent change in the reorientation mechanism via birefringence was developed which exploits the difference in reorientational time constants between the two mechanisms.

Part II: Thin Films of Block copolymers

It is well known that in thin film samples additional complexity is added through surface and interface energies which significantly influence the structure formation. Commonly thermal annealing (TA) and solvent vapor annealing (SVA) are utilized to enhance the ordering in thin films by increasing the mobility of the polymer. Upon thermal annealing the thin film sample is exposed to temperatures above the glass transition temperature (T_g) but below the decomposition temperature of the polymers in an inert gas or vacuum environment. In the case of solvent vapor annealing the sample is placed in a controlled atmosphere containing selected solvent vapors. The effectivity of SVA is dependent on the solubility of the block copolymer constituents in the utilized solvents. Next to pure solvents also solvent mixtures can be used. Both methods accelerate the self-assembly kinetics of the block copolymer resulting in an augmentation of the size of ordered domains. Slight changes in annealing conditions and film thickness may already alter the thin film morphology of the block copolymer. Despite these disadvantages the thin film analysis of block copolymers is attractive since they account for higher applicability than the bulk samples and are more interesting for future applications in nanopatterning:

(i) Enhancing Long-range Order through a Combined Approach

Nowadays high χ copolymers are highlighted which afford the formation of tiny patterns below 10 nm. In this thesis polystyrene-*block*-poly(dimethylsiloxane) (PS-*b*-PDMS) was utilized which furthermore has the benefit of a high etch selectivity between its constituents - a feature especially important for pattern transfer applications. Prerequisite for its utilization in future applications is accomplishing long-range order.

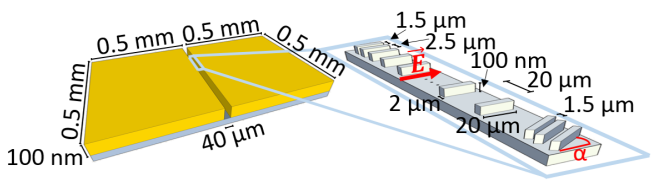

In **Chapter** 7 we systematically analyze how the combination of two directing effects (graphoepitaxy and electric field) influences the self-assembly of cylinder forming polystyrene-*block*-polydimethylsiloxane block copolymer in thin films during solvent vapor annealing. To our knowledge this is the first study reporting about the interplay of graphoepitaxy and electric field. Our combined approach allowed to enhance the correlation length of uniaxial ordered striped patterns by an order of magnitude compared to

the individual methods at reduced annealing times. We analyzed how the angle between the electric field direction and the topographic guides, as well as the dimensions of the trenches affected both the quality of the ordering and the direction of the orientation of cylindrical domains: parallel or perpendicular to the topographic features which was summarized in a phase diagram of microdomain orientation. This combined approach allows the fabrication of highly ordered block copolymer structures using macroscopically pre-patterned photolithographic substrates (see image on the left) [KBCI*15].

(ii) Complex Order-order Phase Transitions in Thin Films

The morphologies formed by diblock copolymers are well studied and limited. Therefore, in **Chapter** 8 the studies are extended to star-shaped 3-miktoarm triblock terpolymers which exhibit an extraordinary structural diversity. These polymers possess a metalorganic block which alters their behavior upon exposure to electric field compared to previously analyzed systems. Polymers comprising polyferrocenylsilane (PFS) blocks represent an interesting class of materials since they combine the structural diversity of multiblock polymers with the unique physical properties of the PFS block, such as electroactivity and electrochromism which arise from the presence of transition metals in the polymer backbone [ZWM14, KM01]. Through systematic variation of parameters the effect of electric field on the morphological transitions and ordering behavior of polyferrocenylethylmethylsilane block (PFEMS)-containing copolymers was analyzed and explained.

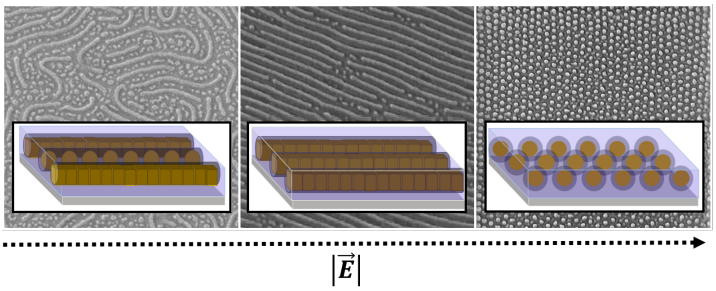

Analyzing structures in swollen films of metalorganic sphere- and cylinder-forming diblock copolymers, as well as of 3-miktoarm polyisoprene-arm-polystyrene-arm--PFEMS (3μ-ISF) terpolymers we decouple two types of responses to the electric field: an increase in the volume fraction of the PFEMS block by oxidation of the ferrocenyl groups inducing morphological transformation, and orientation of the dielectric interfaces of microdomains parallel to the electric field vector. In the case of 3μ-ISF, the former effect dominates the morphological behavior at high electric field strengths, leading to a perfectly hexagonally ordered dot pattern. Our results demonstrate multiple tunability of ordered microdomain morphologies, suggesting future applications in nanofabrication and surface patterning [KBN*15].

2. Methods

2.1. Birefringence [1]

2.1.1. Polarization States of Light

Light is an electromagnetic wave which is characterized by an electric field strength (**E**), an electric displacement density (**D**), a magnetic field strength (**H**), and a magnetic flux density (**B**) which are all interconnected by Maxwell's field equations and the associated constitutive material relations. The state of polarization is defined by **E**. Regarding a fixed point in space the vibration of the electric vector can be decomposed into three individual linear harmonic vibrations:

$$\mathbf{E} = E_x\hat{\mathbf{x}} + E_y\hat{\mathbf{y}} + E_z\hat{\mathbf{z}} \tag{2.1}$$

$$E_i = \tilde{E}_i \cos(\omega t + \delta_i) \tag{2.2}$$

Where $i = x, y, z$ and $\hat{\mathbf{x}}$, $\hat{\mathbf{y}}$, and $\hat{\mathbf{z}}$ are the unit wave vectors in x-, y-, and z-direction, respectively. The most general state of polarization of monochromatic light is elliptical polarization. Figure 2.1 displays the parameters defining the ellipse of polarization in its plane. The orientation of the plane of the ellipse of polarization is described by the unit vector $\hat{\mathbf{n}}$ which is orthogonal to the displayed x- y- coordinate system and points to the reader. The state of polarization can be defined by the following parameters:

(1) The azimuth θ which defines the angle between the major axis of the ellipse and the positive x-axis. θ is displayed in purple in Figure 2.1 and can have values between $-\frac{1}{2}\pi$ and $\frac{1}{2}\pi$.

(2) The ellipticity $e = \frac{b}{a}$ where b is the length of the semi-minor axis and a is the length of the semi-major axis.

(3) The handedness which determines if the ellipse traverses in a clockwise sense (right handed) or counter clockwise sense (left handed) when looking against $\hat{\mathbf{n}}$ with $-1 \leq e \leq 1$. The handedness can also be described by the ellipticity angle ϵ defined as $e = \tan\epsilon$ which is displayed in dark blue in Figure 2.1 and can obtain values between $-\frac{1}{4}\pi$ and $\frac{1}{4}\pi$.

[1] This section is in parts based on a textbook by Azzam and Bashara. [AB77]

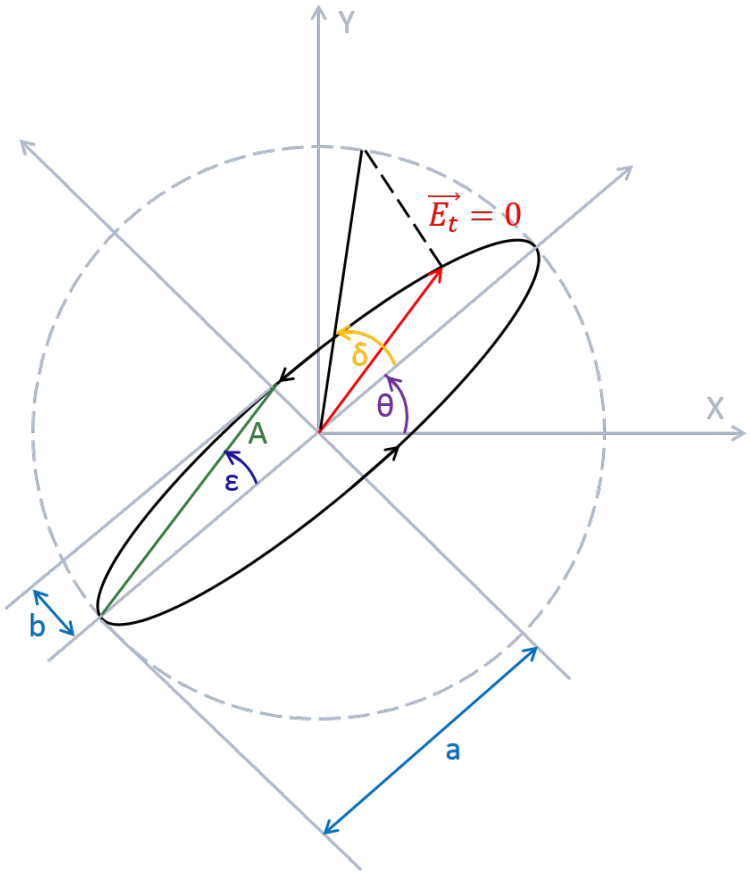

Figure 2.1.: The ellipse of polarization in its plane. This figure was adapted from Ref. [AB77].

(4) The amplitude A which has the value $A = (a^2 + b^2)^{\frac{1}{2}}$.

(5) The absolute phase δ which describes the angle between the position of the electric field vector at t=0 and the ellipse's major axis.

Special cases of polarization are linear (e=0) and circular (e=1: right handed circularly polarized; e=1: left handed circularly polarized) polarization. Figure 2.2 gives the direction of the electric field vector in space for examples of (a) linear, (b) circular and (c) elliptical polarization, where **E** is displayed by the blue arrows.

2.1.2. Light Passing Through an Uniaxial Linear Birefringent Medium

Traversing through a uniaxial birefringent medium the light wave will experience different refractive indices (n_e, n_o) depending on if its polarized parallel or perpendicular

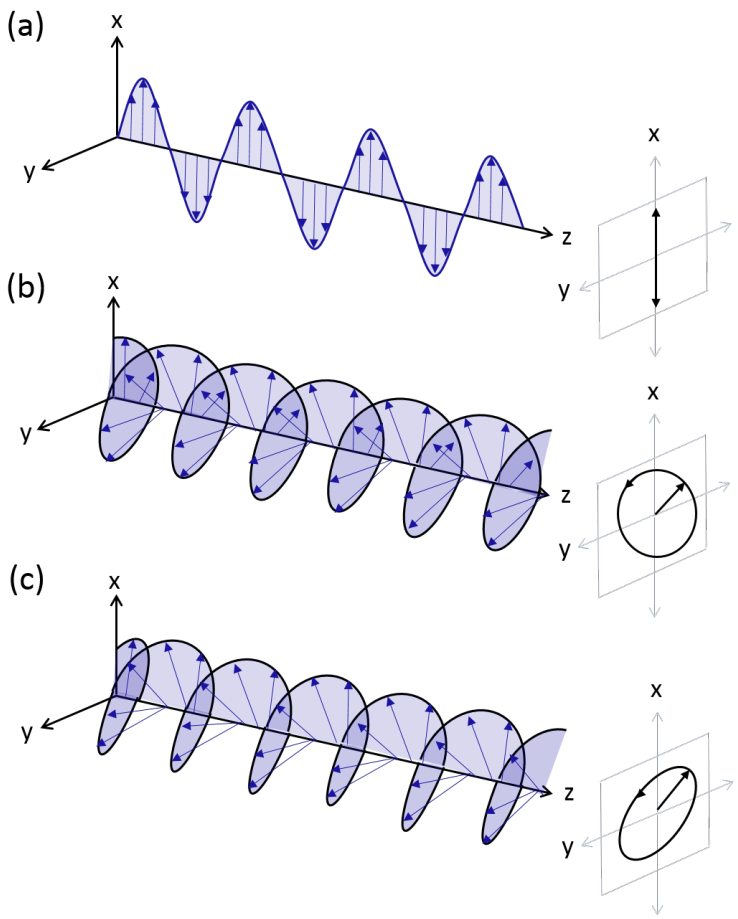

Figure 2.2.: Exemplary electric field vectors of (a) linear (b) circular and (c) elliptically polarized electromagnetic waves.

to the optic axis. Components of light polarized parallel to the optic axis will therefore travel at speed $\frac{c}{n_e}$ where n_e is the extraordinary refractive index while components polarized perpendicular to it will traverse through the medium with $\frac{c}{n_o}$ (n_o: ordinary refractive index).

When $n_e < n_o$ the medium is negative birefringent and the optic axis is the fast axis. In case of $n_e > n_o$ the material exhibits positive birefringence, meaning the optic axis is the slow axis. Components of light polarized along the slow axis will experience a phase retardation with respect to those polarized along the fast axis. Therefore, the polarization state of light is altered upon passing through a birefringent medium. A detailed description on birefringence of block copolymers will be given in Chapter 3.

2.1.3. Exicor 150AT

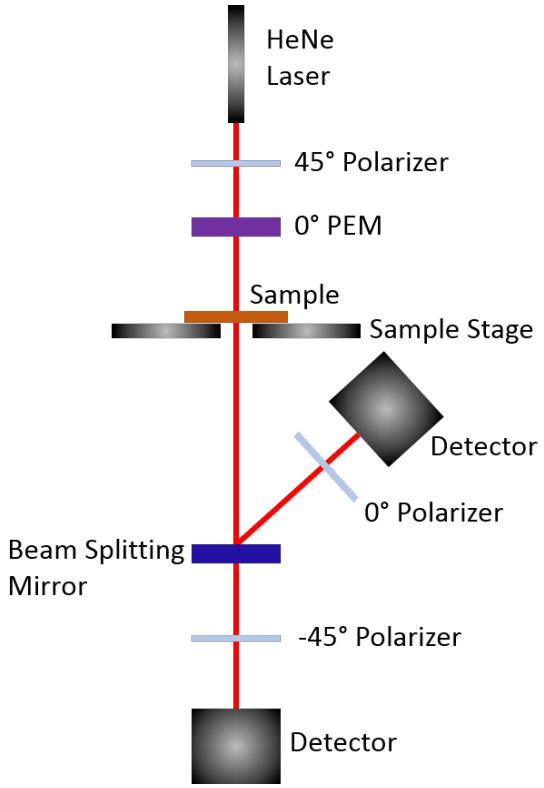

Figure 2.3.: Schematic image of the setup of an Exicor 150AT. This image was adapted from http://www.hindsinstruments.com/wp-content/uploads/Exicor-150AT.pdf.

Birefringence measurements are conducted with an Exicor 150AT from Hinds Instruments which measures magnitude and fast axis orientation of the sample's optical retardation. Figure 2.3 schematically shows the setup of the Exicor. Owing to its special design moving parts in the optical train can be avoided and the alteration of measurement angles is not necessary. The HeNe laser beam is first polarized by a 45° polarizer and subsequently passes through a photo elastic modulator (PEM). After traversing through the sample the beam is divided in two parts by a beam splitting mirror. Both beams afterwards pass through an analyzer, an optical filter, and a photodetector. A lock-in amplifier processes the electronic signals which are further converted using a software algorithm to determine the magnitude of retardation and the angle of fast axis orientation.

2.2. Small Angle X-ray Scattering (SAXS) [2]

2.2.1. Basic Scattering Theory

Figure 2.4 displays an incident beam with wavelength λ in direction of the unit wave vector $\mathbf{u_i}$ which is scattered on a sample. The incident radiation is scattered through angle α and leaves the sample in direction of the unit vector $\mathbf{u_s}$. When the beam is coherently scattered at O and j the phase difference Δ between the two scattered waves

[2] This section is partly based on textbooks by R.J. Roe and K. Mortensen. [Roe00, Mor01]

is merely dependent on the difference in optical path length (l) covered by the two rays. The scattered photons are no longer in phase, whereby the phase difference amounts:

$$\Delta = \frac{2\pi}{\lambda} l = \frac{2\pi}{\lambda}(\mathbf{u_i} - \mathbf{u_s})\mathbf{r_j} = \mathbf{q}\mathbf{r_j} \tag{2.3}$$

The scattering wave vector $\mathbf{q}$ is defined as the difference between incident ($\mathbf{q_i}$) and

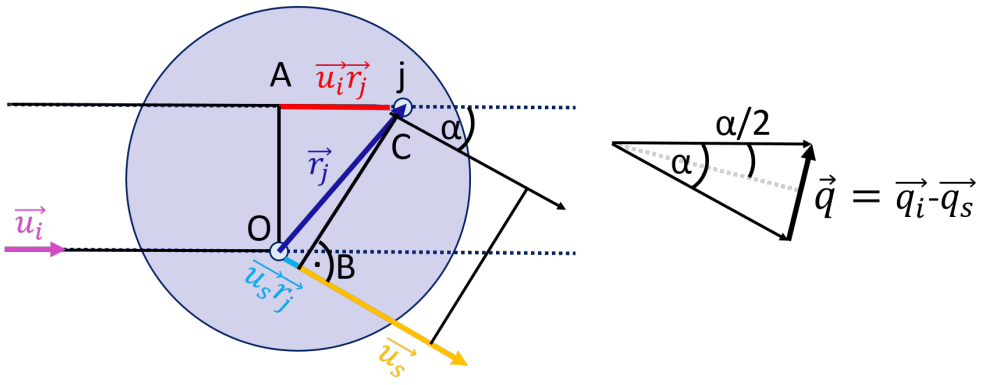

Figure 2.4.: Schematic illustration of scattering from two points in a sample. The incident beam is scattered under the angle α. $\mathbf{q}$ displays the scattering wave vector which is defined by the difference between the incident and the scattered wave vector. This figure was adapted from Ref. [Roe00].

scattered ($\mathbf{q_s}$) wave vectors.

$$\mathbf{q} \equiv \mathbf{q_i} - \mathbf{q_s} \tag{2.4}$$

The overall value of q amounts:

$$q \equiv |\mathbf{q}| = 2|\mathbf{q_i}| \sin\left(\frac{\alpha}{2}\right) = \frac{4\pi}{\lambda} \sin\left(\frac{\alpha}{2}\right) \tag{2.5}$$

Diffraction patterns can be described by Bragg's Law:

$$n\lambda = 2d\sin(\alpha) \tag{2.6}$$

Comparison of equation 2.5 and 2.6 reveals that the distance between two scatterers (d) can be determined from the diffraction pattern through the scattering vector $\mathbf{q}$:

$$d = \frac{2\pi n}{q} \tag{2.7}$$

In real samples the radiation is scattered from several different points described by vectors $\mathbf{r_j}$. The overall scattering amplitude can be expressed by:

$$A(\mathbf{q}) = \sum_i b_i \exp(i\mathbf{q}\mathbf{r_i}) \tag{2.8}$$

Where b_i is the scattering length which describes the interaction between radiation and matter. When the x-rays enter the sample its electrons are accelerated by the electric field of the radiation. The beam is scattered by each electron proportional to $b_e = e^2/(m_e c^2)$. e and m_e are charge and mass of an electron and c displays the speed of light. To account for their interactions an integration over all electrons is performed which yields an expression for the scattering length as a function of the charge distribution within the atom ($\rho(\mathbf{r})$):

$$b_z = \int b_e \rho(\mathbf{r}) d^3 r \tag{2.9}$$

The scattering intensity is given by $I(\mathbf{q}) = K|A(\mathbf{q})|^2$, where K is dependent on the geometry, the intensity of incident flux and the transmission through the sample.

2.2.2. Scattering from Block Copolymer Microstructures

In the phase separated regime each thermodynamically stable structure can be identified by a characteristic sequence of Bragg reflections. Table 2.1 summarizes the ratios between successive Bragg peaks for the most common block copolymer microstructures.

Table 2.1.: Ratios of successive Bragg peaks for different diblock copolymer morphologies.

Morphology							
Space group		1	2	3	4	5	6
Spheres	(hkl)	110	200	211	220	310	222
$Im\bar{3}m$	q_{hkl}/q_{100}	1	$\sqrt{2}$	$\sqrt{3}$	$\sqrt{4}$	$\sqrt{5}$	$\sqrt{6}$
Cylinders	(hkl)	100	110	200	210	300	320
P6mm	q_{hkl}/q_{100}	1	$\sqrt{3}$	$\sqrt{4}$	$\sqrt{7}$	$\sqrt{9}$	$\sqrt{12}$
Gyroid	(hkl)	211	220	321	400	420	332
$Ia\bar{3}d$	q_{hkl}/q_{100}	$\sqrt{3}$	$\sqrt{4}$	$\sqrt{7}$	$\sqrt{8}$	$\sqrt{10}$	$\sqrt{11}$
Lamellae	(hkl)	100	200	300	400	500	600
Pm	q_{hkl}/q_{100}	1	2	3	4	5	6

Usually only the first few Bragg peaks can be observed as broadened peaks when analyzing the Intensity vs q plots obtained from scattering patterns of block copolymer solutions due to the limited domain size and regularity.

2.3. Atomic Force Microscopy (AFM)

Atomic Force Microscopy (AFM) is a non-destructive measurement technique which was developed by Binning et al. in 1986 to probe nanometer sized objects on a scale of a few μm^2. [BQG86] A schematic image of the setup of an AFM is given in Figure 2.5 (a) A cantilever with a tip composed of silicon or silicon nitride scans a section of the specimen surface whereby its position in x- y- and z- is controlled by a piezo-element.

Figure 2.5 (b) displays the cantilever deflection as a function of piezo displacement upon approaching the surface (red curve) and retrieving from the specimen (green curve). Approaching the surface attractive van der Waals and electrostatic forces act on the tip. When the distance between tip and specimen is reduced even further, repulsive forces dominate. Retrieving from the sample surface hysteresis can be observed, meaning that the tip jumps off contact further away from the sample than it jumped to contact. Reason for this are adhesion forces between the tip and the surface. This interaction with the sample results in deflection of the cantilever according to the height profile of the specimen. In Figure 2.5 (b) the cantilever deflection is displayed as a function of piezo displacement.

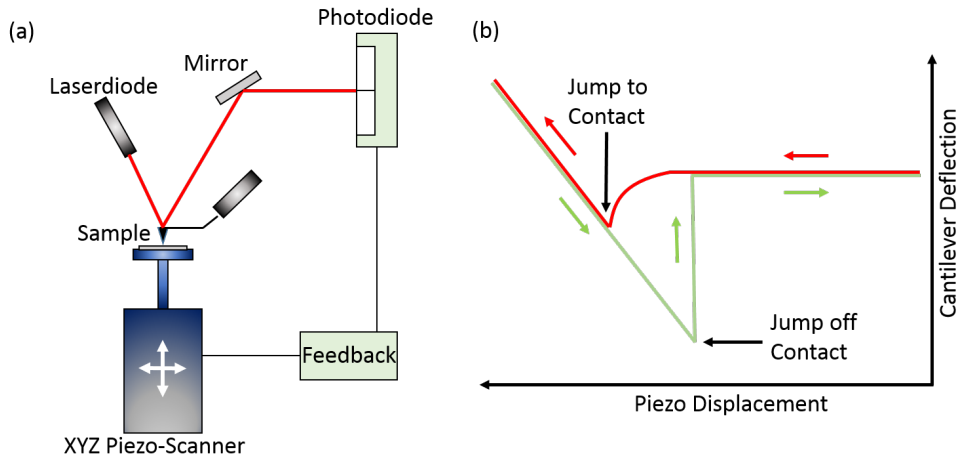

Figure 2.5.: (a) Schematic image of an AFM. (b) Cantilever deflection as a Function of piezo displacement upon approaching (red curve) and retrieving from (green curve) the specimen surface. This figure was adapted from the lecture notes of "Optische Spektroskopie und Streumethoden zur Untersuchung komplexer Fluide" from Prof. A. Böker.

A laser beam pointing to the cantilever is reflected onto a position sensitive photo detector comprising two photodiodes. The amount of laser light on each individual photo

diode varies depending on the deflection of the cantilever. A topographic image of the surface is constructed by converting the optical information into height information.

Three different measurement modes can be distinguished: contact-, tapping-, and non-contact mode. In contact mode the tip is in direct contact to the surface. Advantage of this mode is the relatively good resolution at high scan rates. An unfavorable implication is that tip and sample are more likely damaged [DPCGHB98, BQG86].

Measuring in non-contact mode, the cantilever is excited to oscillate slightly above its resonance frequency at a distance of a few nanometers from the sample surface. Van der Waals and other long range forces acting between the specimen and the tip, give rise to a reduction in cantilever resonance frequency which causes attenuation in the amplitude of oscillation. By means of a control loop, the amplitude is held constant leading to a topographic image of the sample. [GHBM00]

In the tapping-mode the cantilever is brought to oscillation at or slightly below its resonance frequency by a piezo-crystal. Only periodic contact between tip and specimen is established through which the method is less damaging than the contact mode. The resonance frequency of the system is shifted through the forces acting between tip and surface. To gain a topographic picture of the sample the oscillation amplitude is held constant as in the non-contact mode. [DPCL*00]

From the phase shift between excitation and oscillation information on the hardness respectively the softness of the surface can be gained. Attractive interactions between tip and specimen cause a negative phase shift while repulsive interactions implicate a positive phase shift. When interpreting the phase shift, the influence through material properties and measurement parameters has to be considered.

The lateral resolution is determined by the radius of the tip, the larger the radius the higher the relative broadening of the imaged structures. If the distance between the pictured particles is too small they cannot be imaged individually. Another disadvantage of the method is that only a small part of the sample can be analyzed making it impossible to prove a homogenous covering of the sample surface.

2.4. Electron and He-Ion Microscopy [3]

Using optical characterization methods the smallest distance δ that can be resolved is proportional to the wavelength λ of the incident radiation as stated by the Rayleigh criterion for visible light microscopy given in equation 2.10. The refractive index is denoted by n, and β is the semi-angle of collection of the magnifying lens. Therefore, it

[3] This section is in parts based on a textbook by Williams. [WC96]

is not possible to image structures in the size range of a few nanometers by conventional light microscopy.

$$\delta = \frac{0.61\lambda}{n \sin \beta} \tag{2.10}$$

Applying an acceleration voltage of 100 kV, the wavelength of electrons is in the order of a factor 104 smaller compared to the wavelength of UV radiation making imaging of nanometer sized objects feasible. Under consideration of relativistic effects the wavelength of electrons λ can be calculated according to equation 2.11 where h is the Planck constant, V the acceleration voltage of the electron microscope, m_0 the electron mass, c the speed of light and e the elementary electric charge.

$$\lambda = \frac{h}{\left(2m_0eV\left(1 + \frac{eV}{2m_0c^2}\right)\right)^2} \tag{2.11}$$

Field-emission guns are commonly used as electron source. Through the applied voltage the emitted electrons are accelerated to energies of 1-30 keV for scanning electron microscopy (SEM) and to values between 80 and 400 keV for transmission electron microscopy (TEM). The electron beam can be focused by usage of magnetic lenses. Next to elastic and inelastic scattering electrons as a type of ionizing radiation can produce a variety of secondary signals when interacting with matter such as the emission of secondary electrons (SE), Auger electrons, back scattered electrons (BSE) and the emission of visible light or X-rays through the relaxation of excited atoms which can be used to gain information on the sample.

In scanning electron microscopy (SEM) the sample is scanned by an electron beam focused on the sample through an electronic lens system. Scanning of the sample is accomplished by the use of deflection coils. Upon interaction between electrons and matter such as elastic and inelastic scattering, emission of secondary electrons, emission of Auger electrons and emission of radiation such as x-rays or cathodoluminicence, different information can be obtained.

Due to the relative low energy of the electrons, the penetration depth into the sample is rather small. The secondary electrons (SE) emitted from the near surface layers of the sample give information on the topography and are detected by an Everhart-Thornley-Detector which consists of a scintillator and a photomultiplier. In energy dispersive x-ray analysis for each element characteristic x-rays emitted by excited atoms during relaxation are analyzed to determine the chemical composition of the surface. Here the energy of the x-ray corresponds to the energy difference between the two atomic energy levels. Since the scattering intensity is dependent on the atomic number, back-scattered electrons (BSE) can be used to gain information on the morphology of the sample.

For the detection of BSE, microchannel plates are used since the Everhart-Thronley detectors are insensitive to high energetic electrons.

For sensitive materials such as polymers and biomolecules it is desirable to use low energy electron beams to avoid destruction of the sample. By the use of a field-emission (FE) cathode in the electron gun of a scanning electron microscope, narrower probing beams at high and low electron energies are accomplished. As a result sample charging and damage can be decreased by simultaneously improving the spatial resolution. Therefore, metallization of nonconductive materials is not required.

The principle of He-Ion microscopy is similar to that of scanning electron microscopy just that the sample is scanned by a He-Ion beam. Advantages compared to scanning electron microscopy include the small De Broglie wavelength of the He-Ions and the high source brightness. High resolution images can be obtained from a larger variety of materials compared to SEM.

2.5. Ellipsometry [4]

Ellipsometry is a non-destructive sensitive optical measurement technique from which information on the thickness and dielectric properties of thin films can be gained by investigation of the change of polarization of light reflected from a sample. Film thicknesses of a few nanometers can be determined with excellent accuracy. Information on e.g. morphology, chemical composition, and electrical conductivity can be gained from the complex refractive index and the dielectric function tensor. Figure 2.6 shows a polarization ellipse of an elliptically polarized wave which propagates along the z-axis of the right handed Cartesian coordinate system.

X and Y denote the amplitudes of the electric field in x- and y-direction. The electric field vector $\mathbf{E}(t)$ in the pictured z=0 plane is given by:

$$\mathbf{E}(t) = \begin{bmatrix} \mathbf{E}_x(t) \\ \mathbf{E}_y(t) \end{bmatrix} = Re\left\{ \begin{bmatrix} Xe^{i\Delta} \\ Y \end{bmatrix} \right\} e^{i\omega(t-t_0)} \tag{2.12}$$

The y-component reaches its maximum at $t = t_0$ and the x-component after another time interval Δ/ω, where ω is the angular frequency and Δ the phase shift. The state of elliptic polarization is characterized by the phase shift Δ and the relative amplitude X/Y which can be expressed using the angle Ψ as stated in equation 2.13.

$$\tan\Psi = \frac{X}{Y} \tag{2.13}$$

[4] This section is in parts based on a textbook by Tompkins. [TE05]

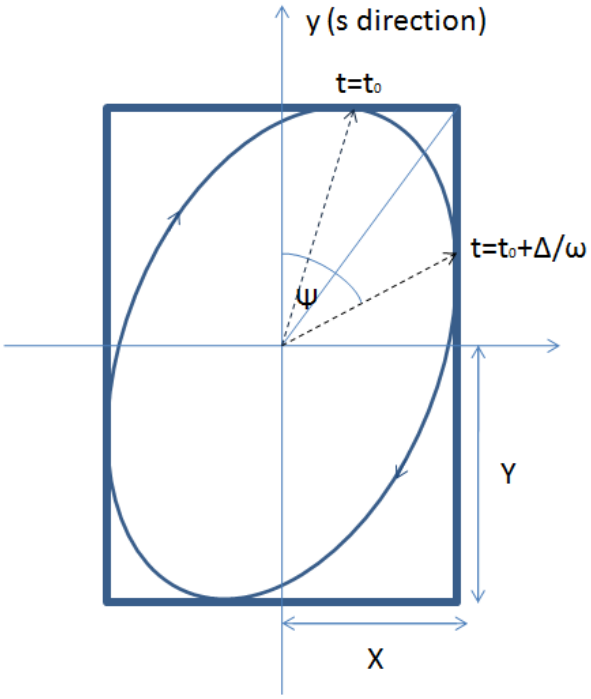

Figure 2.6.: Polarization ellipse of an elliptically polarized wave which propagates along the z-axis of the right handed Cartesian coordinate system. The y-component reaches its maximum at $t = t_0$ and the x-component after another time interval Δ/ω, whereas Δ is the phase shift and ω the angular frequency. X and Y are the amplitudes in x- and y-direction. This figure was adapted from Ref. [TE05].

The elliptic polarization can therefore be expressed by the Jones vector:

$$\begin{bmatrix} \sin(\Psi e^{i\Delta}) \\ \cos(\Psi) \end{bmatrix} \tag{2.14}$$

Basis of ellipsometry is the manipulation of the polarization state of light by polarizing elements and the measured sample. The conventional ellipsometric setup consists of a light source, a linear polarizer, optionally a compensator, the sample, another linear polarizer called analyzer and a detector as schematically shown in Figure 2.7.

According to the Fresnel-equations the linear polarized, incident light experiences a change in polarization state upon reflection from the sample. The incident and reflected beam lie in the plane of incidence which also contains the normal of the sample surface. The incident beam can be decomposed into components polarized parallel (p-polarization) or perpendicular (s-polarization) to the plane of incidence. Upon reflection the s- and p-polarized components behave differently. The reflected wave can be described by multiplying the complex amplitudes of the s- and p-polarizations by

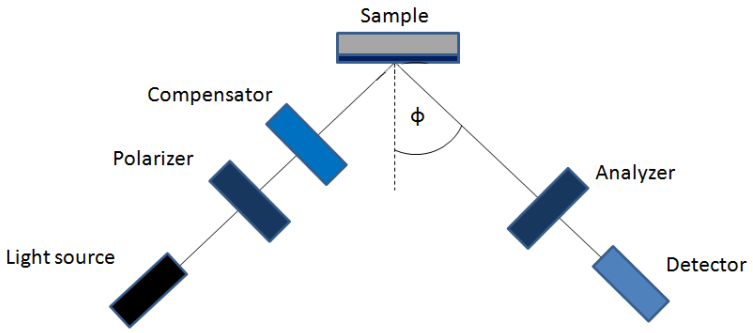

Figure 2.7.: Schematic setup of an ellipsometer. This figure was adapted from Ref. [TE05].

the complex reflectivity r_p (complex reflectivity of the p-polarizations) and r_s (complex reflectivity of the s-polarizations). In ellipsometry the complex reflectance ratio ρ_r is measured which is given by equation 2.15. Δ is the relative phase of the vibrations along the x- and y-directions.

$$\rho_r = \frac{r_p}{r_s} = \tan(\Psi)e^{i\Delta} \tag{2.15}$$

Δ and Ψ can only be converted directly into the optical constants when measuring optical infinitely thick films. If this criterion is not fulfilled a layer model must be applied. This model must consider the optical constants and thicknesses of the individual layers as well as their correct sequence. Disadvantage of the method is that detailed knowledge about the layer composition is essential to obtain accurate data. In an iterative procedure the optical constants are varied and Δ and Ψ can be calculated using the Fresnel equations until the values fit the experimental data. Advantages of ellipsometry are that no reference measurement has to be conducted since intensity ratios are measured instead of intensities leading to a low sensitivity concerning intensity fluctuations.

Part I.

Bulk Samples of Block copolymers

3. Birefringence Analysis of Block copolymers

3.1. Introduction and Theoretical Background

3.1.1. Electrothermodynamics of Dielectric Materials

Infinitesimal changes in the internal energy (dU) of a system comprising N_i molecules in a volume V can be described by thermodynamics according to 3.1 [LLP04].

$$dU = TdS - pdV + \sum_i \mu_i dN_i \tag{3.1}$$

Here S is the entropy of the system, T the temperature, p the pressure, and μ_i the chemical potential of the i-th component. Under use of the particle density $\rho \equiv \frac{N_i}{V}$ and the entropy per unit volume $s \equiv \frac{S}{V}$ 3.1 can be rewritten to

$$du = Tds + \sum_i \mu_i d\rho_i. \tag{3.2}$$

By introducing the free energy density f the system can be described by considering the change in temperature rather than the change in entropy. The Legendre-transformation, $f = u - Ts$ of Equation 3.2 yields

$$df_0 = -sdT + \sum_i \mu_i d\rho_i \tag{3.3}$$

describing infinitesimal changes in the free energy density, df.

When the system is exposed to an external stimulus an additional term must be added to the equation and the change in free energy density can be described according to Equation 3.4.

$$df(\mathbf{r}) = -sdT + \sum_i \mu_i d\rho_i - \mathbf{D}(r)d\mathbf{E}. \tag{3.4}$$

The last term of the equation describes the electrostatic contribution when the external stimulus is an electric field. Here $\mathbf{E}$ is the electric field vector, and $\mathbf{D}$ is the displacement

field related with $\mathbf{E}$ through $\mathbf{D} = \epsilon\mathbf{E}$ where ϵ is the dielectric constant of the medium. We now picture a system comprising two materials with different dielectric constants ϵ_1 and ϵ_2 separated by a sharp interface which is exposed to an electric field. $\mathbf{D}$ and $\mathbf{E}$ each have a component perpendicular and parallel to the interface between the two media. While the perpendicular component of $\mathbf{D}$ is continous across the interface the perpendicular component of $\mathbf{E}$ is discontinous and given by $\epsilon_1\mathbf{E_1} = \epsilon_2\mathbf{E_2}$ where $\mathbf{E_1}$ and $\mathbf{E_2}$ are the electric fields in perpendicular direction. Opposed to this the parallel component of $\mathbf{E}$ is continous across the interface, while that of $\mathbf{D}$ is not [Tso09].

To obtain the electrostatic energy density (F_{es}) the electrostatic contribution to the free energy per unit volume is integrated over the volume of the system:

$$F_{es} = -\frac{1}{2}\int_V \frac{\mathbf{D}^2}{\epsilon} d^3r \tag{3.5}$$

A Legendre transform and the relation $\mathbf{D} = \epsilon\mathbf{E}$ yields the electrostatic energy for linear dielectrics (F_{es}):

$$F_{es} = F - F_0 = -\frac{1}{2}\int_V \epsilon\mathbf{E}^2 d^3r. \tag{3.6}$$

Here F_0 is the free energy without application of electric field. The important result of Equation 3.6 is that an electric field lowers the free energy of a system with intrinsic composition fluctuations. The derived equation is universal and not dependent on the medium's constituents.

3.1.2. Block Copolymers in Electric Fields

3.1.2.1. In the Weak Segregation Limit

To analyze the effect of electric field on liquid mixtures of two dielectrics and block copolymers a spacially dependent order parameter $\phi(\mathbf{r})$ is defined as a dimensionless quantity describing the relative composition of one liquid or copolymer component at $\mathbf{r}$ ($0 < \phi < 1$).

$$\phi(\mathbf{r}) = \phi_0 + \varphi(\mathbf{r}); \langle\varphi(r)\rangle = 0 \tag{3.7}$$

Here ϕ_0 is the average composition and φ the variation from the average. The variation in composition results in a variation in dielectric constant ϵ. Under assumption that the system is isotropic ϵ is a scalar and not a tensor. In case of small φ, $\epsilon(\phi)$ can be expressed as a Taylor series expansion to second order:

$$\epsilon(\phi) = \bar{\epsilon} + \Delta\epsilon\varphi + \frac{1}{2}\epsilon''\varphi^2 \tag{3.8}$$

Now an electric field $\mathbf{E}_0$ is defined which is present in the system when ϵ is constant throughout the sample. Since ϵ and $\mathbf{E}$ are connected through Laplace's equation variations in ϵ lead to variations in electric field. [Tso09]

$$\mathbf{E} = \mathbf{E}_0 + \mathbf{E}_1\varphi + \frac{1}{2}\mathbf{E}_2\varphi^2 \tag{3.9}$$

The quadratic term of the expansion vanishes in the limit of $\varphi << 1$. An analytical expression for the linear term $\mathbf{E}_1\varphi$ was given by Amundson [AHQS93]

$$\mathbf{E}_1\varphi = \sum_q \tilde{\mathbf{E}}(\mathbf{q}) \exp(i\mathbf{qr}) \tag{3.10}$$

$$\tilde{\mathbf{E}}(\mathbf{q}) = -\frac{\beta}{\bar{\epsilon}}\tilde{\varphi}(\mathbf{q})(\hat{\mathbf{q}}\mathbf{E}_0)\hat{\mathbf{q}} \tag{3.11}$$

$\beta = \frac{\delta\bar{\epsilon}}{\delta\phi}$ describes the sensitivity of the dielectric constant to composition fluctuations.

Landau and Lifshitz evaluated how the Gibbs free energy density, $F(\epsilon)$ changes as a function of ϵ [LLP04]:

$$\delta F(\epsilon) = -\frac{1}{2}\mathbf{E}^2\delta\epsilon \tag{3.12}$$

Under consideration of Equation 3.6 the electrostatic energy density in a medium of average dielectric constant $\bar{\epsilon}$ is given by:

$$F = -\frac{1}{2}\bar{\epsilon}|\mathbf{E}(\varphi)|^2 \tag{3.13}$$

Neglecting the second order term in expression 3.9 the electrostatic free energy contribution of small composition fluctuations is obtained:

$$F = \frac{\beta^2}{2\bar{\epsilon}}\sum_q (\hat{\mathbf{q}}\mathbf{E_0})^2\varphi(\hat{\mathbf{q}})\varphi(-\hat{\mathbf{q}}) \tag{3.14}$$

Equation 3.14 is valid for small variations in $\phi(\mathbf{r})$ when the dielectric contrast between the systems constituents is small compared to $\bar{\epsilon}$. It can be applied to ordered phases in the weak segreation limit i.e. in proximity to the critical point and in the disordered phase. According to equation 3.14 composition fluctuations with wave vectors normal to the applied field minimize the electrostatic energy and are hence stabilized. Composition fluctuations with wave vectors parallel to $\mathbf{E}$ generate interfaces perpendicular to $\mathbf{E}$ and are therefore destabilized. This has severe influence on the orientation of the block copolymer nanostructure: interfaces preferentially align parallel to the electric field vector in case of morphologies for which 3.14 is non-zero i.e. those of uniaxial symmetry.

3.1.2.2. In the Strong Segregation Limit

In the strong segregation limit interfaces are sharp and the composition and hence the dielectric constant does not vary smoothly over the interface but exhibits a square-wave composition profile (see Figure 3.2 (c)). Hence, equation 3.14 does not apply. While phase A is characterized by dielectric constant ϵ_1 the dielectric constant of phase B amounts ϵ_2. Tsori and Andelman [TA03] derived the electrostatic energy (F_{es}) of lamella with orientation parallel and perpendicular to the direction of electric field. For their calculations they assumed a parallel-plate capacitor analogy with distance L between its plates and potential difference V (see Figure 3.1).

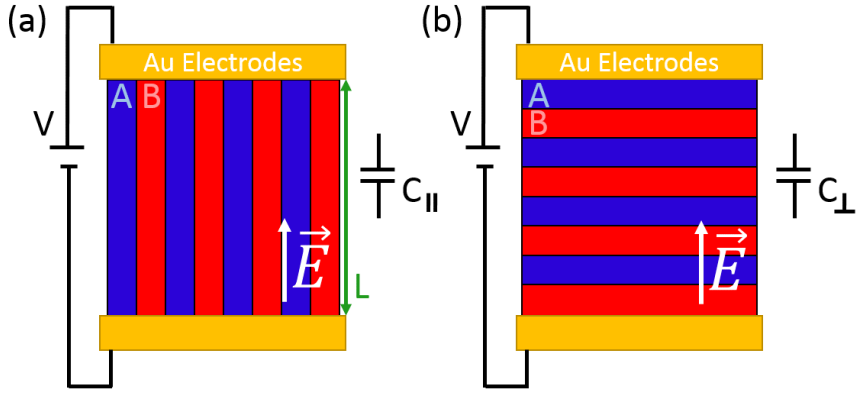

Figure 3.1.: Simplified illustration of a lamella stack in a parallel-plate capacitor analogy with lamellae interfaces oriented parallel ($C_\parallel$) (a) and perpendicular ($C_\perp$) (b) to **E**. This figure was adapted from Ref. [Tso09].

The electrostatic energy per unit area for lamellae with interfaces oriented parallel ($F_{es\parallel}$) and perpendicular ($F_{es\perp}$) to **E** amounts:

$$F_{es\parallel} = -\frac{1}{2}\frac{\epsilon_1\epsilon_2}{\bar{\epsilon}}\frac{V^2}{L} \tag{3.15}$$

and

$$F_{es\perp} = -\frac{1}{2}\bar{\epsilon}\frac{V^2}{L} \tag{3.16}$$

The average dielectric constant is given by $\bar{\epsilon} = \frac{1}{2}(\epsilon_1 + \epsilon_2)$. Equations 3.15 and 3.16 imply that dielectric interfaces oriented parallel to the electric field vector are electrostatically favored over those oriented perpendicular to **E**. The electrostatic energy difference is proportional to the square of the dielectric contrast between phases A and

B ($(\Delta\epsilon)^2 = (\epsilon_1 - \epsilon_2)^2$). Consequentially, the dielectric interfaces perferentially align parallel to the electric field vector similar as in the weak segregation limit.

3.1.2.3. Experiments and Theory

Amundson et al. were the first to demonstrate electric-field-induced ordering in a lamellae forming diblock copolymer melt of polystyrene-*block*-poly(methyl methacrylate) (PS-*b*-PMMA) in 1991 [AHD*91]. The block copolymer was shown to rearrange with its interfaces parallel to the electric field vector (**E**) when exposed to strong DC electric fields. Driving force for the reorientation is the electrostatic energy penalty associated with dielectric interfaces not oriented parallel to **E** [SPR*13]. As described in the previous paragraph the energy difference between parallel and perpendicular orientations with respect to **E** was found to be proportional to the square of the dielectric contrast $(\Delta\epsilon)^2$ between the two copolymer constituents and to the second power of the electric field strength E^2 [Tso09]. Experimentally block copolymer nanostructures have been shown to align with their interfaces parallel to the electric field vector as well in bulk [AHQS93] as also in thin film [MLU*96].

Further work by Amundson et al. [AHQS93, AHQ*94], Böker et al. [BEH*02a, BEH*03, BSK*06], Schmidt et al. [SBZ*05, SSS*07] and Ruppel et al. [RPL*13] unveiled the kinetics and mechanisms of the reorientation process. Using concentrated polystyrene-*block*-polyisoprene (PS-*b*-PI) solutions in toluene as a model system, three reorientation mechanisms were distinguished. The degree of phase separation as well as the pre-orientation of the block copolymer sample were shown to determine the exploited mechanism.

In the strong segregation limit (SSL) the rotation of entire grains is observed while "Nucleation and Growth" - i.e. the growth of lamellae grains aligned parallel to the electric field vector at expense of those oriented perpendicular to **E** - is the predominant mechanism at lower degrees of phase separation [BEH*02a]. The reorientation of block copolymers in even closer vicinity to the order-disorder transition was found to proceed via "Selective Disordering" [RPL*13]. Selective disordering is associated with the selective disintegration of ill aligned lamellae upon exposure to sufficiently large electric fields while no disordering is found for grains aligned parallel to the electric field vector. Theory and simulations support the experimental results [Gur94, KSZF03, PW99, TTL03]. Next to lamellae block copolymer morphologies also cylindrical block copolymers [TADRK02, TADRJ00] as well as triblock copolymers [BKE*02] have been oriented in the electric field.

In the past decade block copolymer/nanoparticle composite materials have gained considerable interest since they afford a variety of potential applications. While the

nanoparticles exhibit interesting catalytic, [JBCM03] optical, [MUY*02, BLB03, BT04] mechanical, [BLB03] or magnetic properties, [THD02] block copolymers, can effectively control particle location and patterns [TGMB01, TGMB02]. Simulations by Yan et al. imply an alteration in reorientation mechanism and kinetics upon exposure to electric fields when nanoparticles are added to the system [YSB10]. A more precise description of the reorientation mechanisms will be given in Chapter 5 which deals with the effect of nanoparticles on the reorientation mechanisms of block copolymers under application of electric fields.

While morphologies of uniaxial symmetry (lamellae, cylinders) readily align upon application of electric field - provided that the threshold voltage for the particular system is exceeded [TADRJ00, BEH*03] - interfaces with an unfavorable angle to **E** cannot be eliminated in cubic phases (spheres, gyroids) by altering their orientation. In these cases minimization of the electrostatic free energy can merely be achieved by distortion of the unit cell leading to elongation in direction of **E** upon exposure to electric fields. Consequently, order-order transitions are induced when the copolymer compositions is in vicinty of the phase boundary and the field is of sufficient magnitude. The following electric field-induced order-order phase transitions have been analyzed in simulations and experiments: gyroid to cylinder [SPS*10, LHKZ07, PZ08], sphere to cylinder [XZS*04, LZS06, Mat06, TTAL03, WCR08, WD08], HPL to lamella [PSR*15], and HPL to cylinder [LHKZ08, LHKZ09]. Despite the fact that Schmidt et al. [SPS*10] reported the synchrotron SAXS study of an electric field-induced gyroid to cylinder transition, its mechanisms could not be resolved to date. Therefore, in Chapter 6 a detailed synchrotron SAXS analysis of the electric field strength and temperature dependent mechanisms characterizing the transition is given.

Electric fields were also shown to shift the order-disorder transition temperature (T_{ODT}) of lamellae forming block copolymers to lower values favoring the disordered phase [SSSB09, SPR*13]. This stands in direct contrast to theoretical considerations which anticipate the shift of T_{ODT} into the opposite direction [Tso09, GSTAT07, OF95, STA09]. Chapter 4 deals with this problem in detail and gives a general overview over hitherto performed calculations and experiments. Therefore, we refer to the introduction of Chapter 4 for a detailed description of the theoretical background behind the effect of electric fields on the T_{ODT}.

3.1.3. Birefringence

Previously, synchrotron small angle x-ray scattering (SAXS) was utilized to analyze block copolymer solutions under application of an electric field. Block copolymer microstructures can exhibit as well form- birefringence as also intrinsic- birefringence

[BEH*02b, BEH*03, SBZ*05, RPL*13, PRS*11]. In this chapter birefringence measurements are probed as an alternative measurement technique since they are easily accessible, inexpensive, non-destructive and therefore allow high data throughput. *In-situ* birefringence measurements display an effective means to analyze the kinetics of alignment processes [CIK*97], order-disorder transitions [AHPQ92, BPS92] as well as order-order transitions between birefringent and non-birefringent block copolymer phases with excellent time resolution and therefore display a valuable supplementary method to synchrotron SAXS, especially for time-consuming measurements. First a general literature overview on birefringence measurements of block copolymer microstructures is given, then the sample cell is described which was likewise used for birefringence measurements as also for synchrotron SAXS measurements and allowed a precise control over temperature and electric field. In the last part of this chapter exemplary measurements are presented to demonstrate the scope of this method.

3.1.3.1. Intrinsic Birefringence

Intrinsic birefringence results from the orientation of block end-to-end vectors, and the stretching of block copolymer chains away from the block-block interfaces as schematically shown in 3.2 (a). Lodge and Fredrickson predicted that the intrinsic birefringence is directly proportional to the stretching of the chains defined by $\frac{L^2}{\langle h^2 \rangle_0}$, where L is the layer thickness and $\langle h^2 \rangle_0$ is the mean-square unperturbed end-to-end distance [LF92]. In strongly segregated lamella and cylindrical block copolymer systems ($\chi N \gg 10$) this represents a significant contribution to the overall birefringence strength of the sample and can even be comparable to or greater than the form birefringence [LF92]. In the Strong Segregation Limit (SSL) the interfaces separating the microdomains are very narrow since the system wants to minimize the unfavorable A-B interfacial area. This results in perturbed, extended chain configurations and therefore in an entropic penalty. Figure 3.2 (c) displays the one dimensional composition profile characterizing the SSL, where ϕ_A is the volume fraction of the A block.

In block copolymer samples close to the order-disorder transition temperature (Weak Segregation Limit) the intrinsic birefringence only plays a minor role [AHPQ92]. In the weak segregation limit the individual polymer chains are largely unperturbed and the one dimensional composition profile 3.2 (b) is near to sinusoidal.

In the disordered phase A-B interactions are weak and the individual chain statistics are Gaussian like [BF90]. Therefore, the intrinsic birefringence diminishes in the disordered phase.

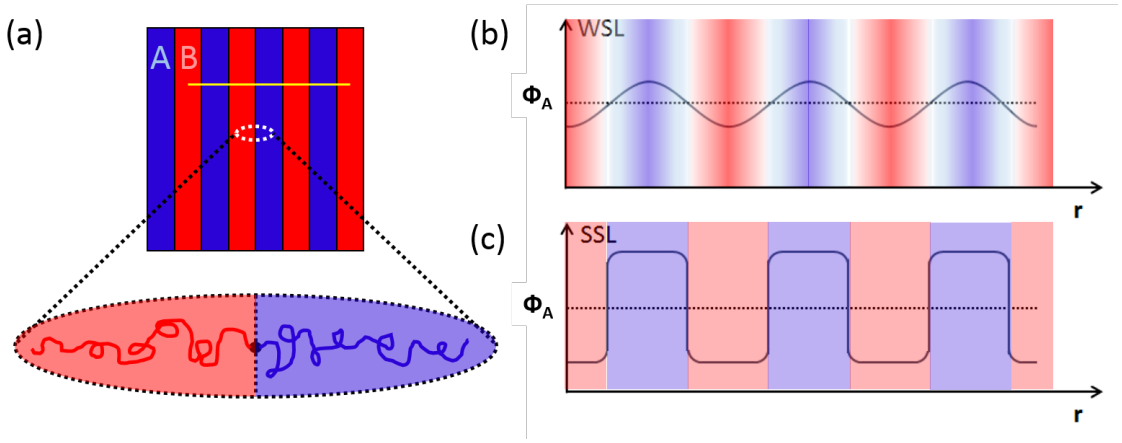

Figure 3.2.: (a) Schematic representation of a lamella block copolymer phase in the strong segregation limit (SSL). The individual block copolymer chains are stretched away from the interfaces to minimize the unfavorable A-B contact area. (b, c) One dimensional composition profiles characterizing the WSL (b) and SSL. ϕ_A displays the volume fraction of A while r displays the position in the sample. The dotted black line in the plots corresponds to a ϕ_A volume fraction of 0.5. The yellow line in (a) displays the position r in the sample. Parts of this figure were adapted from Ref. [BF90].

3.1.3.2. Form Birefringence

Form birefringence arises from an ordered anisotropic arrangement which is large compared to the size of the individual molecules but small with respect to the wavelength of light. Since a vast majority of the birefringence measurements in this thesis were performed on lamellae systems form birefringence is explained on the example of a lamellae stack. A lamella microdomain pattern is characterized by a uniaxial optical anisotropy resulting in form birefringence. Figure 3.3 displays a simplified illustration of a lamella stack, its optic axis and the direction of the fast and the slow axis. The axis of symmetry, also known as the optic axis, which is indicated by the green arrow in Figure 3.3, is perpendicular to the lamella interfaces. Components of light propagating through the sample are exposed to different refractive indices n_o and n_e depending on whether their direction of polarization is perpendicular (ordinary wave (o), direction indicated by blue arrows) or parallel (extraordinary wave (e), direction indicated by red arrows) to the optic axis. In the case of negative uniaxial birefringence, as found in a lamella assembly, the fast axis coincides with the optic axis while the slow axis is perpendicular to it. Light polarized along the slow axis will be refracted with a refractive index n_o while light polarized along the fast axis is exposed to a refractive index n_e. [BW59] Therefore, the

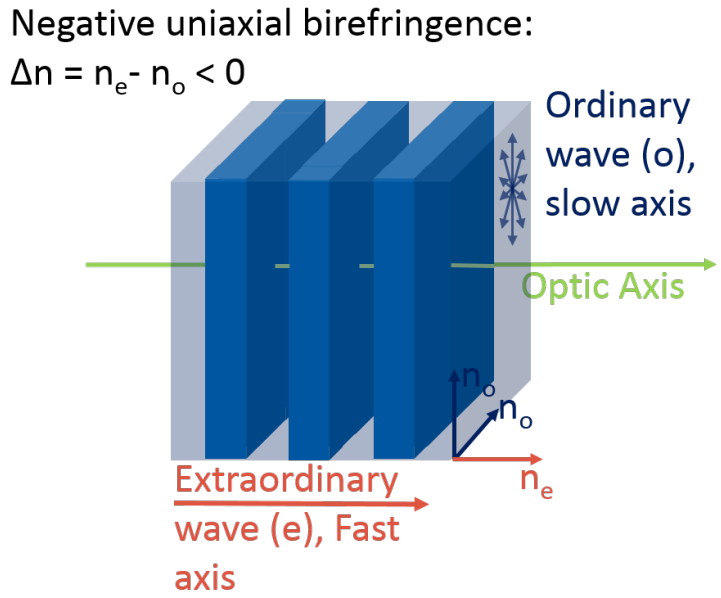

Figure 3.3.: Simplified illustration of a lamella stack, its optic axis and the direction of the slow and the fast axis with respect to the lamella interfaces.

ordinary wave will experience a phase retardation Γ with respect to the extraordinary wave [BW59]. The magnitude of the resulting phase retardation Γ amounts to Eq. 5.1.

$$\Gamma = 2\pi \frac{l}{\lambda} \Delta n^0 \langle \overline{\Psi}^2 \rangle \sin^2 \theta \tag{3.17}$$

Here l is the optical path length, λ describes the wavelength of light while passing through the medium, $\langle \overline{\Psi} \rangle$ denotes the periodic lamella pattern, and θ is the angle between the propagation direction of light and the unit wave vector of the lamella pattern $\hat{e}_k$. $\Delta n = n_e - n_o$ is the birefringence of the sample. The overall birefringence strength of a block copolymer is dependent on its degree of phase separation. In the strong segregation limit (SSL) the interfaces are sharp and a maximum form birefringence strength Δn^0 is attained [AHPQ92].

3.1.3.3. Birefringence in the Disordered Phase

The disordered phase is characterized by a lack of long-range order. Upon approaching the transition to the ordered microphase concentration fluctuations increase. Since these concentration fluctuations have no preferred orientation, and are barely larger than molecular dimensions the material will appear optically isotropic and therefore, will not exhibit form birefringence [AHPQ92].

3.1.3.4. Birefringence of Optically Anisotropic Ordered Phases

When no directing force is applied, the block copolymer sample exhibits a multidomain structure of optically anisotropic, randomly oriented grains without any preferred direction of alignment. Each grain has a constant optic axis which is perpendicular to the lamellae interfaces or parallel to the cylinder axis for lamellae and cylindrical block copolymer microstructures, respectively [AGM*04]. When light propagates through the sample, each individual grain induces a small phase retardation depending on its size, degree of phase segregation, and orientation, whereby typical grain sizes lie in a range of 1-10 μm.

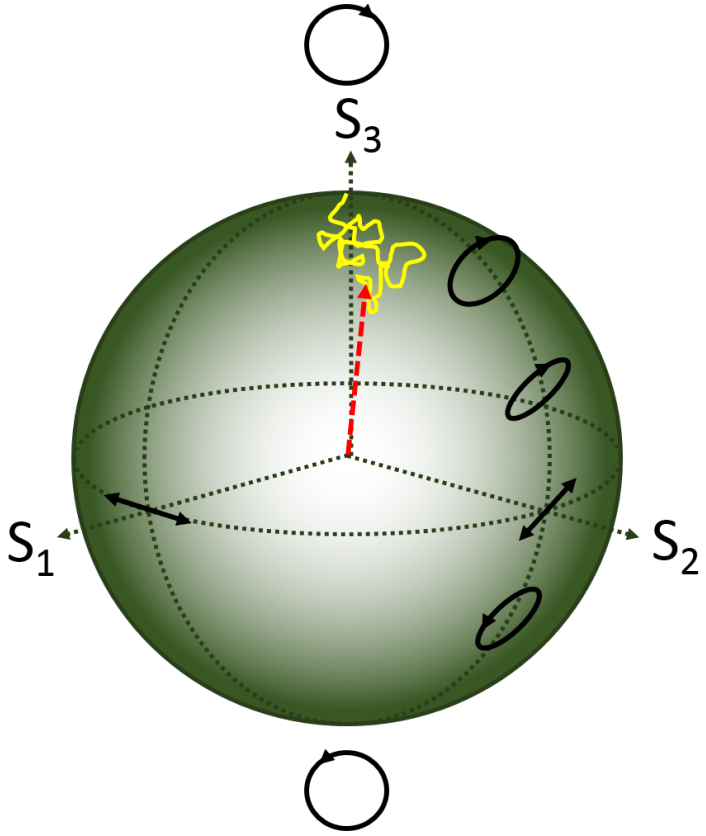

Figure 3.4.: Poincaré sphere. S_1 to S_3 are the Stokes Parameters. Each point on the surface of the sphere represents a different polarization state of light.

Amundson et al. [AHPQ92] described the propagation of light through a macroscopically disoriented sample as a random walk on the poincaré sphere - a spherical surface of unit diameter on which each point corresponds to a different polarization state of light [AHPQ92]. A schematic image of the poincaré sphere is given in Figure 3.4: The north- and south- pole display right- and left circular polarization, respectively, the

equator corresponds to linear polarization along an axis with a direction varying with longitude. The other points on the surface represent different states of elliptical polarization. S_1, S_2, S_3 in Figure 3.4 display the Stokes parameters which are commonly utilized to describe the polarization state of electromagnetic waves through the Stokes vector $\mathbf{S} = \{S_0, S_1, S_2, S_3\}$, where S_0 represents the total intensity of the wave, S_1 defines the difference between the intensities of the x- and the y- components, S_2 indicates the preference of the wave to either the $+\frac{1}{4}\pi$ or the $-\frac{1}{4}\pi$ linearly polarized component and S_3 represents if the wave has a preference to either the right- or the left-handed circularly polarized component [AB77].

Upon passing through the sample each encounter of light with a grain can be described as a small change of position on the poincaré sphere, whereby direction and magnitude of the step are determined by the orientation, the birefringence strength and the size of the grain. This results in a series of uncorrelated small phase retardations. The associated trajectory on the poincaré sphere can be described as a random walk and is exemplified in yellow in Figure 3.4. The overall birefringent phase retardation is determined by the position of the end point.

The laser beam utilized in this study has a diameter of 1 mm while typical grain dimensions lie between 1 μm and 10 μm. Therefore, one ray of light traverses through various microstructural arrangements, displaying different random walks on the poincaré sphere. The overall polarization state of the laser beam exiting the sample will be a mixed state composed of the individual end points of the random walks.

3.1.3.5. Birefringence Analysis of Order-Disorder and Order-Order Transitions

In 1992 Amundson [AHPQ92] and Balsara [BPS92] reported that the order-disorder transition of optically anisotropic block copolymer phases is accompanied by a change in birefringent phase retardation. As reported in the previous paragraphs both the intrinsic- and the form birefringence diminish upon approaching the disordered phase. Therefore, the birefringent phase retardation can be used as a direct measure to analyze the order-disorder transition of lamellae and cylindrical block copolymer phases, making it possible to determine the order-disorder transition temperature (T_{ODT}) as well as the kinetics of the transition. Opposed to lamellae and cylindrical microstructures optically isotropic block copolymer structures such as bcc and gyroid do not exhibit form birefringence. Therefore, order-order phase transitions between optically isotropic and anisotropic structures can likewise be detected by birefringence measurements [LJK*02]. This enables the optimization of the conditions under which the order-order transition takes place with optical techniques and saves time when subsequently performing synchrotron SAXS measurements to get closer insights into the underlying mechanisms.

3.1.3.6. Birefringence Analysis of Alignment Kinetics

In the past birefringence measurements have been utilized to analyze the alignment of block copolymers under shear flow [GKCK96, GKKS95, WNC*00]. Chen et al. proposed a combination of *in-situ* rheo-optical measurements, *ex-situ* electron microscopy and *in-situ* SAXS to probe alterations in microstructure and orientation upon flow-induced alignment [CK98]. Birefringence measurements offer excellent time resolution while providing information on the degree of alignment of optically anisotropic block copolymer microstructures and are therefore well suitable for the real-time analysis of the alignment kinetics.

The degree of alignment of a block copolymer sample is described by the orientational order parameter P_2.

$$P_2 = \frac{3\langle\cos^2\theta\rangle - 1}{2} \tag{3.18}$$

A macroscopically disordered sample is characterized by $P_2 = 0$ while a maximum alignment of lamella interfaces parallel to the electric field vector corresponds to an order parameter of -1/2. For perfect alignment perpendicular to the electric field vector $P_2 = 1$ is found. The effective overall birefringence strength of the block copolymer sample is directly proportional to the order parameter and amounts:

$$\Delta n = \Delta n^0 \langle\overline{\Psi}^2\rangle P_2 \sin^2\theta. \tag{3.19}$$

Therefore, the phase retardation can be used as a direct measure to analyze the reorientation kinetics.

3.2. Experimental

3.2.1. The Sample Cell

A sample cell was constructed which could likewise be utilized for birefringence and SAXS measurements. Figure 3.5 shows photos of the sample cell (a-b) as well as its engineering drawing (c) and a schematic cross sectional view. The sample cell was milled from a single polyetheretherketone (PEEK) block, a high performance polymer with excellent temperature- ($T_g = 143°C$; $T_m = 343°C$) and solvent resistivity against most common solvents. Furthermore, the high dielectric strength of the material of 20 $kVmm^{-1}$ permits the application of high voltage.

The parallel plate capacitor in the middle of the setup comprises two polished gold electrodes ④ (Figure 3.5; 15 mm × 5 mm × 1 mm) which afford electric fields of high homogeneity. A thin platinum wire connects the back side of the electrodes with the

connectors to the high voltage power source ⑤. Quartz glass slides above and below the capacitor ⑨ are tightly screwed to the cell preventing solvent evaporation. Solvent resistant O-rings made from perfluoroelastomer (FFKM) properly seal the sample cell. When SAXS measurements are performed with this setup the glass slides can easily be replaced by kapton sheets covered with a thin layer of teflon ⑧ (DuPont™Kapton® Films, 300FN929 and 500FN131). Normal kapton sheets did not show sufficient resistivity against the utilized solvents. The teflon covered kapton sheets were immersed in solutions of THF and toluene to determine the material compatibility. Even after weeks no deformation of the film in solution was observed. Teflon pieces with the same dimensions as the glass slides (thickness: 1 mm; diameter: 3 cm) were pressed to the kapton sheets and screwed to the sample cell. This on the one hand fixed the kapton and on the other hand prevented voltage breakthrough to the outside of the cell. Measurements were performed through a 1 mm wide centered hole directly above the middle of the capacitor. Next to SAXS and birefringence measurements this sample cell was constructed in such a manner that it can likewise be used for Small Angle Neutron Scattering (SANS) and Polarization Optical Microscopy (POM) measurements.

3.2.1.1. Temperature Regulation

A circular Peltier element ⑦ (*EURECA* Messtechnik GmbH, TEC1C-24.0-9.8-21/78-CS) with a maximum operating temperature of T_{max} = 120°C underneath the lower glass slide permits precise regulation of heating- and cooling cycles. The Peltier element has a thermoelectric strength of $\alpha = 0.0157$ VK^{-1}, an internal resistance of $\rho = 0.624\Omega$ and a coefficient of heat conductivity of $\gamma = 0.153$ WK^{-1} and is addressed remotely via a LabVIEW software module. A metal plate ④ which stands in direct contact to the back side of the Peltier element assures the necessary heat transfer between the Peltier element and the surrounding. The temperature is measured in solution via a PT100 thermosensor ③ covered by thin glass. In Figure 3.6 the measured temperature is plotted against the time in seconds. Prior to the measurement the sample cell was filled with a concentrated block copolymer solution in toluene. The feedback of the PT100 is used to control the temperature. When a heating- and cooling rate of ± 1.5 °$Cmin^{-1}$ was provided by the LabVIEW program (see Appendix 3.12 for the block diagram of the software) the respective heating- and cooling rates determined by the PT100 thermosensor were 1.47 °$Cmin^{-1}$ and -1.44 °$Cmin^{-1}$. The terminal values were in accordance with the set temperatures. Figure 3.6 displays a uniform temperature augmentation and diminution which is especially important for the precise determination of for instance the order-disorder transition temperature.

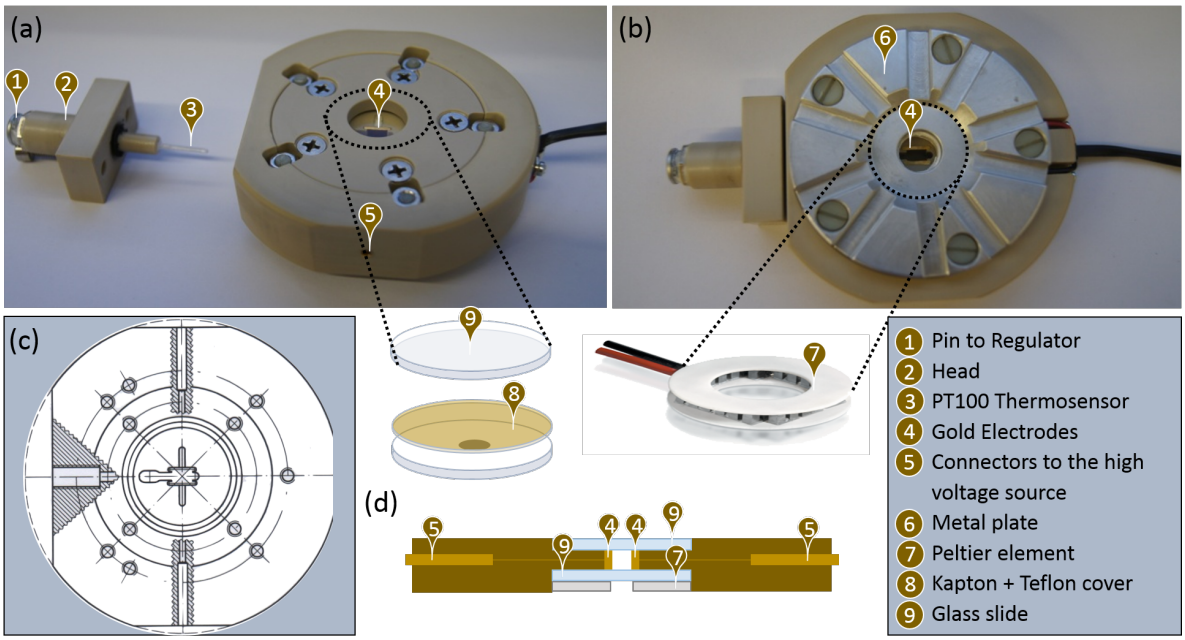

Figure 3.5.: (a,b) Photos of the sample cell used for the bulk analysis of block copolymers under the application of electric field. The block copolymer solution is sandwiched between two polished gold electrodes ④. Two glass slides ⑨ tightly seal the chamber above and below the parallel plate capacitor preventing solvent evaporation as demonstrated in the schematic cross section image (d). Heating- and coolingrates can precisely be regulated via a circular Peltier element ⑦. A metal plate ⑥ below the Peltier element ensures rapid heat transfer to the surrounding. The Head ② which seals the sample cell comprises a tiny PT100 thermosensor covered by thin glass ⑦ for precise *in-situ* temperature determination. The high voltage power source is connected to the gold electrodes via ⑤. (c) Engineering drawing of the sample cell. The sample cell was built by Guido Kirf from the Mechanical Lab at Institute of Physical Chemistry, RWTH Aachen University.

3.2.2. Birefringence Measurements

Concentrated solutions (32-43 wt%) of the block copolymer in THF and toluene were prepared 24 h prior to the measurements to assure complete dissolution, and removement of bubbles from the solution. The exact compositions and concentrations of the polymer solutions will be given in the experimental section of the corresponding chapter. A syringe was carefully filled with the block copolymer solution avoiding the formation of bubbles and subsequently given into the sample cell which was then sealed tightly. Birefringence measurements were performed with an Exicor 150AT birefringence mea-

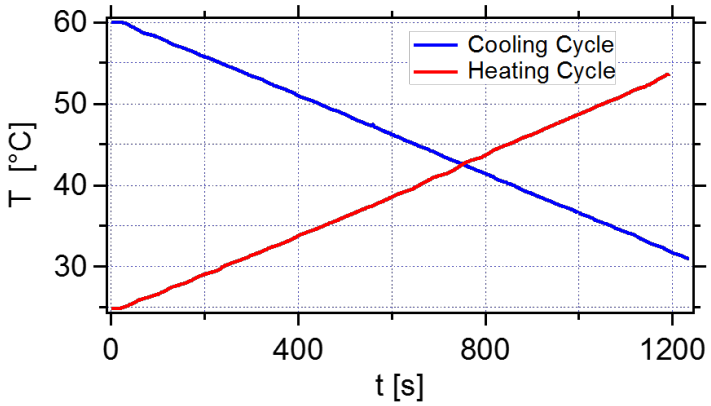

Figure 3.6.: Temperature measured by the PT100 theromsensor as a function of time in s upon heating and cooling via the Peltier element.

surement system from Hinds Instruments which allowed high-speed measurement of the optical retardation and fast axis orientation with high accuracy and resolution. The laser beam with a spot size of 1 mm and a wavelength of $\lambda = 632.8$ mm traversed the sample in the center of the capacitor directly between the two gold electrodes. The optical path length amounted 5 mm.

3.3. Results and discussion

3.3.1. Order-Disorder Transition

3.3.1.1. Determination of T_{ODT}

In Figure 3.7 the evolution of birefringent phase retardation (Γ) is displayed as a function of temperature upon heating through the order-disorder transition (ODT). A schematic of the ordered lamella and the disordered phase are given inside the plot. In this example a concentrated solution (32 wt%) of polystyrene-*block*-polyisoprene $S_{46}I_{54}^{108}$ in THF was utilized. The subscripts define the weight fractions of the blocks and the superscripts denote the average molecular weight in kg mol^{-1}. The heating rate amounted 1 °Cmin^{-1}. Prior to the measurements the sample was oriented at an electric field strength of 5 kV mm^{-1}. Upon heating a slight continuous decrease in the phase retardation is observed up to a temperature of about 37.4 °C. This initial decrease can either be attributed to a softening of lamellae interfaces upon heating or to a reorganization of grains away from the preferred direction induced by the electric field applied prior to the measurement over time. This initial decrease is followed by a steep continuous decline in optical retardation between 37.4 °C and 39.4 °C when the order-disorder transition is approached. Above

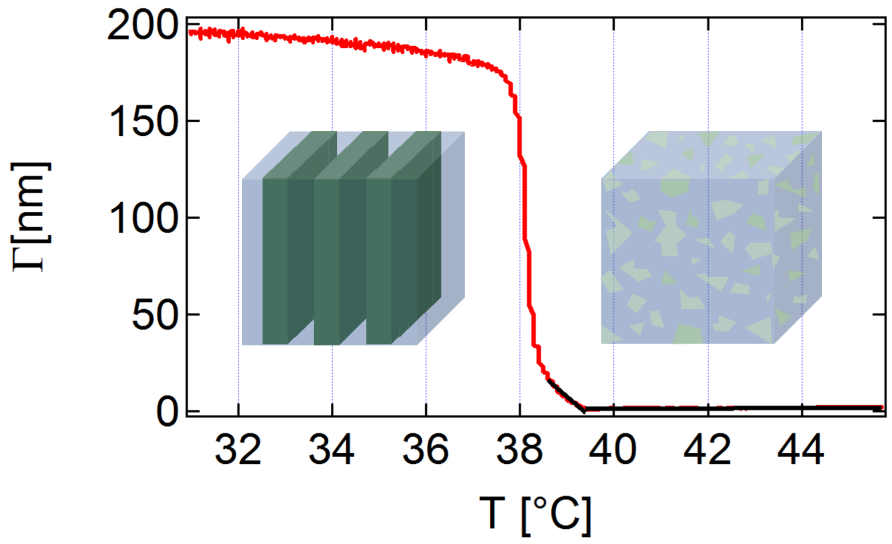

Figure 3.7.: The red curve displays the measured optical retardation (Γ) as a function of temperature upon heating a 32 wt% solution of $S_{46}I_{54}^{108}$ in THF through the order-disorder transition temperature. The T_{ODT} is the intersection point of the two black linear fits. The phase separated and disordered phase are schematically displayed inside the plot. This figure was adapted from Ref. [KKKB15].

this temperature a constant minimum retardation value is measured. As stated above the disordered phase is characterized by directionless concentration fluctuations, and chains are Gaussian like. Therefore, no intrinsic- or form birefringence is observed. To determine the precise order-disorder transition temperature (T_{ODT}) two linear functions are fittet to the data as presented by the black fitting functions in Figure 3.7. The T_{ODT} is identified as the intersection point of the two linear fits. In the following chapter the T_{ODT} measurements presented here will be used to analyze the factors resulting in electric field-induced mixing of block copolymers.

3.3.1.2. ODT-Jump Kinetics

Schoberth et al. [SSSB09] observed a downward shift of the T_{ODT} in concentrated solutions of polystyrene-*block*-polyisoprene in toluene under application of electric fields. This implies that switching on an electric field in a certain temperature interval below the T_{ODT} induces a sudden order-disorder transition. As will later on be demonstrated in Chapter 4, this temperature interval depends on the block copolymer constituents and the overall chain length of the polymer. The kinetics of the phase transition can be monitored by birefringence measurements since the measured phase retardation strongly

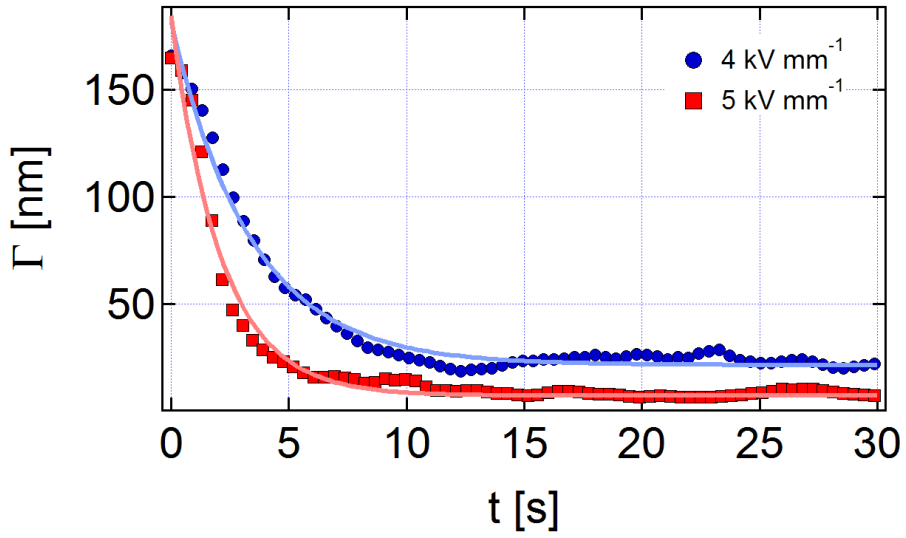

Figure 3.8.: Phase retardation as a function of time for a 42.8 wt% solution of $S_{50}I_{50}^{50}$ in THF at a temperature of 36.5 °C. At t=0 an electric field of 4 kV mm^{-1} (blue circles) and 5 kV mm^{-1} (red squares) is applied.

depends on the degree of block copolymer phase separation. An example measurement for a 42.8 wt% solution of $S_{50}I_{50}^{50}$ in THF is given in Figure 3.8.

The order-disorder transition temperature of the solution was measured before and after recording the melting kinetics and amounted 37.8 °C. The measurement was performed at a temperature of 36.5 °C thus 1.3 K below the T_{ODT}. Upon application of the electric field a steep but continuous decline in phase retardation is observed which can be attributed to the melting of the block-block interfaces. The curves are fitted by a single exponential function to obtain the time constants τ which amount 3.4 s when the electric field strength is 4 kV mm^{-1} and 2.1 s for 5 kV mm^{-1}. Looking at the final retardation values merely the 5 kV mm^{-1} jump induces complete mixing of the microstructure. In case of the 4 kV mm^{-1} jump a residual phase retardation of around 22 nm is observed which implies that the structure has not fully reached the disordered phase. This corresponds to the measurements in the ODT shift. When applying 5 kV mm^{-1} to the sample a downward shift in the T_{ODT} of 1.7 K was observed while for 4 kV mm^{-1} the shift amounted 1.2 K. The temperature interval was too large to induce complete mixing at an electric field strength of $\leq$ 4 kV mm^{-1}.

In Figure 3.9 the time constant τ in s which was obtained as described above is displayed as a function of the distance from the T_{ODT} at which the measurement was performed for a 32 wt% sample of $S_{46}I_{54}^{108}$ in THF (T_{ODT}=40 °C). The melting kinetics were measured at an electric field strength of 5 kV mm^{-1}. For this specific block copoly-

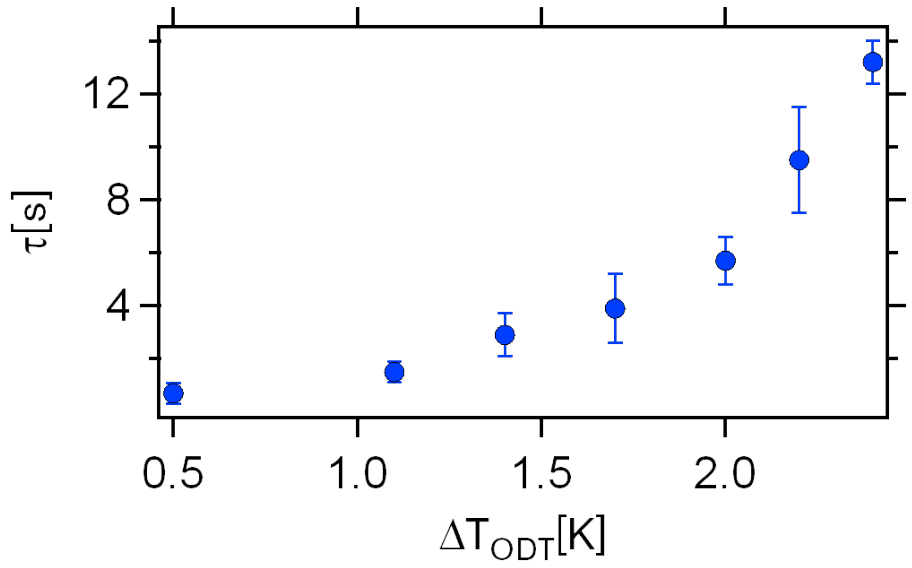

Figure 3.9.: Time constant (τ) describing the kinetics of the electric field-induced order-disorder transition as a function of temperature distance (ΔT) from the T_{ODT} for a 32 wt% sample of $S_{46}I_{54}^{108}$ in THF (T_{ODT}=40 °C). The order-disorder transition was induced by sudden application of an electric field of 5 kV mm^{-1}.

mer sample the T_{ODT} was shifted by -3 °C upon application of an electric field of 5 kV mm^{-1}. Therefore, complete mixing was observed in the analyzed temperature interval of 2.5 °C. The distance from the T_{ODT} has profound influence on the kinetics of melting.

3.3.2. Threshold Voltage

The threshold voltage is the minimum voltage which needs to be applied to the block copolymer sample to induce an electric field-induced reorientation process. It strongly depends on the dielectric contrast between the block copolymer constituents, chainlength and experimental conditions. In this paragraph the experimental procedure to determine the threshold voltage via birefringence measurements is described.

A 32 wt% sample of $S_{46}I_{54}^{108}$ in THF (T_{ODT}=40 °C) was heated to 55 °C, thus 15 K above the T_{ODT} to eliminate any pre-orientation based on the sample history. After 10 min the sample was cooled down to 30 °C exhibiting an isotropic multi-domain structure. As previously described the overall phase retardation upon passing through a non-oriented block copolymer sample can be described as a random walk on the poincaré sphere and is therefore comparably small. When the electric field is large enough to reorient the block copolymer sample an increase in phase retardation is observed since

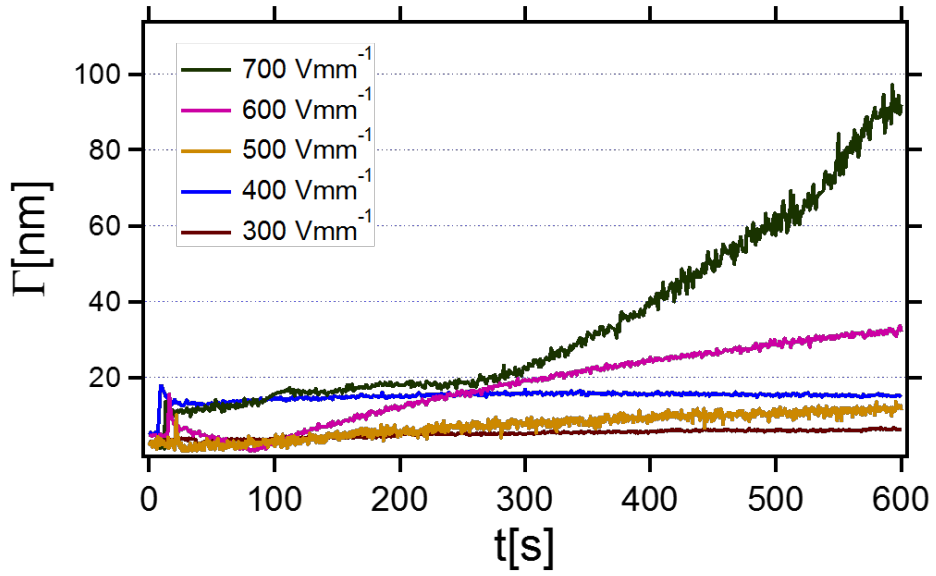

Figure 3.10.: Measurement of the Threshold voltage for a 32 wt% sample of $S_{46}I_{54}^{108}$ in THF (T_{ODT}=40 °C). Prior to the measurement the sample was heated above the T_{ODT} to obtain an isotropic multi-domain structure. After subsequent cooling to 30 °C the respective electric field strength was applied at t=0 s. The plot displays the measured phase retardation as a function of time.

the small phase retardations induced by each single grain are no longer uncorrelated as described in detail in the section "Birefringence Analysis of Alignment Kinetics".

In Figure 3.10 the measured phase retardation is plotted against the time in s. At t=0 the respective field strength was applied to the sample. Up to an electric field of 500 V mm^{-1} no significant increase in phase retardation is observed. The threshold voltage for this particular sample lies at 600 V mm^{-1}.

3.3.3. Order-Order Transitions

Order-order transitions between birefringent and non-birefringent microphaseseparated nanostructures can easily be detected by measuring the change in birefringent phase retardation. In case of order-order transitions additional methods such as synchrotron SAXS have to be applied to determine end and transition states. Non the less the birefringence measurements are useful to screen samples and check which concentrations and polymers are worthwhile to measure in time limited synchrotron SAXS. This is important since order-order transitions can only be induced in close proximity to the boundary between two different microstructures and therefore much time can be saved by excluding samples through pre-observation.

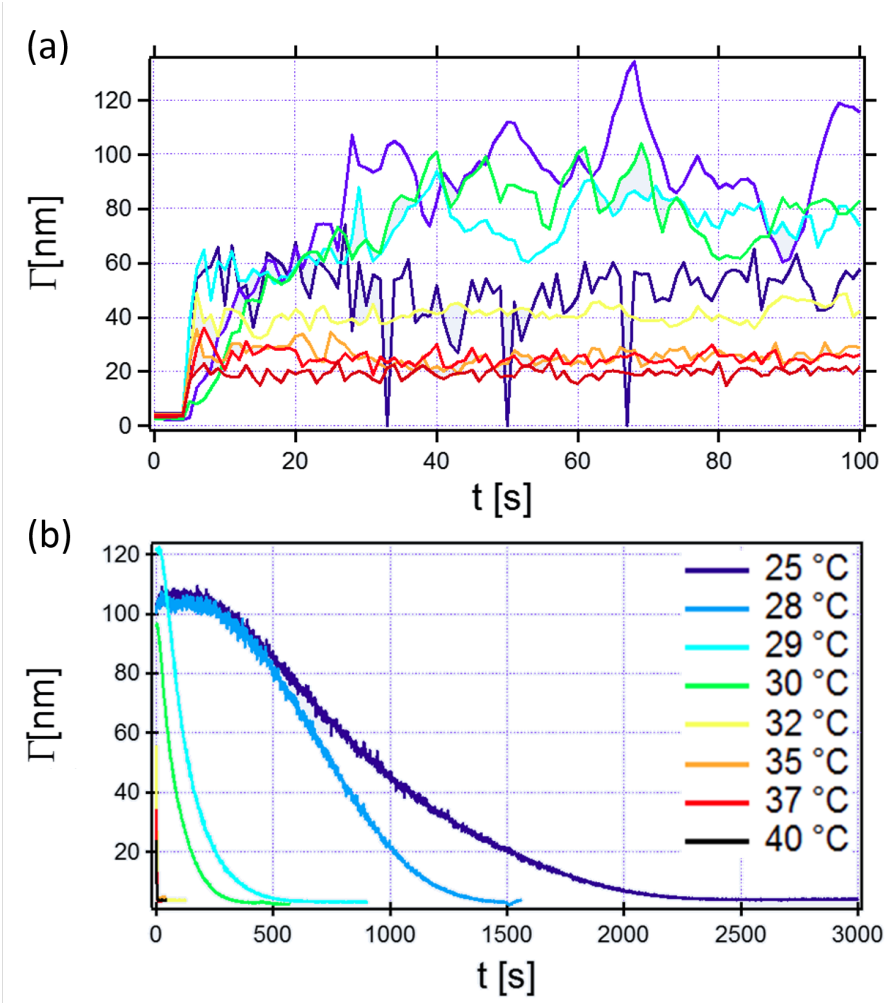

Figure 3.11.: Birefringent phase retardation as a function of time for a 44.3 wt% sample of $S_{22}V_{78}^{98}$ in THF. (a) An electric field of 5 kV mm^{-1} is applied after 5 s. (b) Decrease in birefringent phase retardation after turning off the electric field.

In Figure 3.11 the phase retardation of a 44.3 wt% sample of polystyrene-*block*-poly(2-vinylpyridine) with a polystyrene weight fraction of 22 wt% and a molecular weight of 98 kg/mol ($S_{22}V_{78}^{98}$) in THF is displayed as a function of time at different temperatures between 25 °C and 40 °C. Previously performed SAXS measurements confirmed a gyroid microstructure when no electric field is applied to the sample. In Figure 3.11 (a) the electric field is applied after 5 s. The resulting increase in phase retardation can be attributed to an order-order transition into a birefringent block copolymer microstructure and its subsequent orientation in direction of the electric field vector. Figure 3.11 (b) displays the decline in birefringent phase retardation after turning off the electric field.

This demonstrates that the order-order transition is reversible. In Chapter 6 the results of the synchrotron SAXS measurements on this sample will be evaluated which give insights into the mechanistic pathways of the electric field-induced gyroid to cylinder transition and of the reformation of the gyroid phase.

3.4. Summary

In this chapter we establish an experimental approach to analyze block copolymers in electric fields via birefringence measurements. Birefringence measurements can be utilized to determine the T_{ODT} as well as melting kinetics, reorientation kinetics, the threshold voltage and to detect order-order transitions from birefringent to non-birefringent block copolymer phases and vice versa. In the following three chapters of this thesis three different projects are demonstrated were birefringence was either applied on its own or in combination with synchrotron SAXS to analyze novel aspects of block copolymers in electric fields.

3.5. Appendix

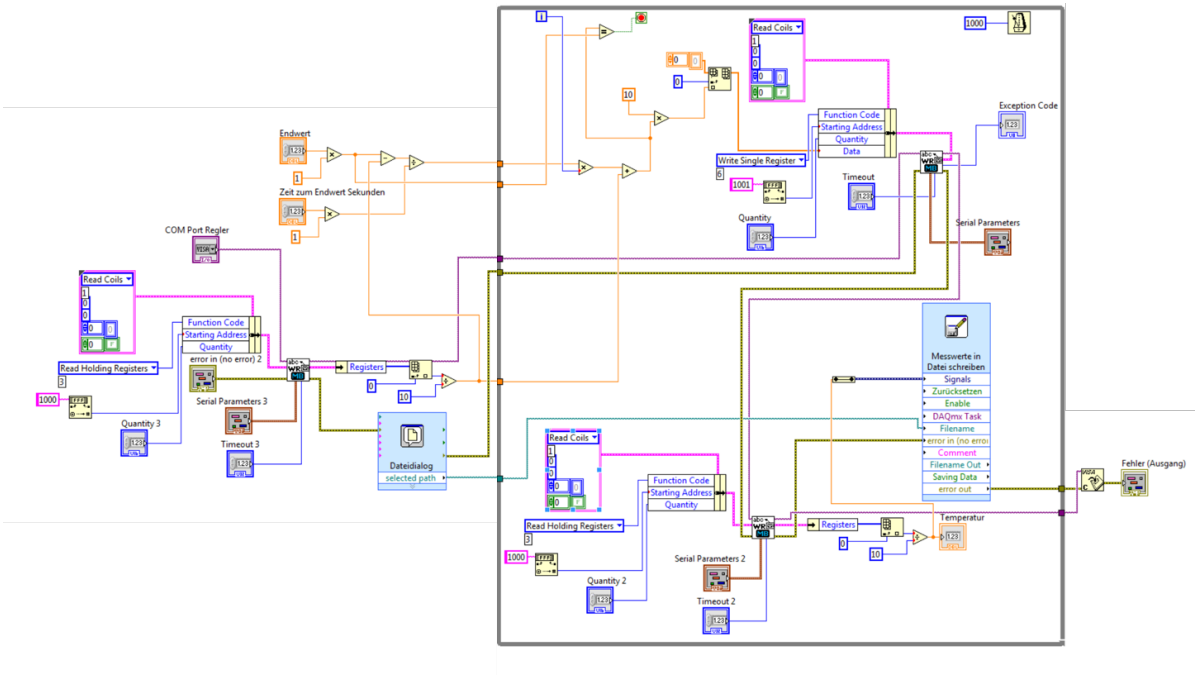

Figure 3.12.: Blockdiagramm of the Labview program regulating the temperature of the sample cell. The program was written by Bernd Huppertz and Christoph Heeren of the Electronics workshop of the Institute for Physical Chemistry at RWTH Aachen University.

4. The Effect of Electric Fields on the Order-Disorder Transition Temperature[1]

4.1. Introduction and Theoretical Background

As previously described electric fields can be utilized to induce order-order [SPS*10] and order-disorder [SSSB09] phase transitions implementing reversible switching between different BCP morphologies. Therefore, the control over BCP morphology is enabled. Thus, a precise knowledge of the impact of electric fields on BCP nanostructures is of fundamental interest. In this chapter the long discussed issue why electric fields are experimentally found to induce mixing as well in block-copolymers as also in polymer mixtures will be addressed. This questions has been under debate since the first experiments on the effect of electric fields on the critical temperature of simple binary mixtures.

Recently, Schoberth et al. [SSSB09] revealed that the T_{ODT} of a 32.5 wt% solution of poly(styrene)-*block*-poly(isoprene) in toluene is lowered by about 2 °C upon application of an electric field of 8.5 kV/mm. Numerous experimental studies on the phase diagram of simple binary mixtures likewise indicate electric field-induced mixing upon exposure to an electric field although the effect is much less pronounced. For low molecular weight substances a downward shift in the critical temperature T_c by merely a few millikelvins scaling with the square of the applied electric field strength was observed [WF93, Orz98]. Reich and Gordon who worked with a mixture of poly(vinyl methyl ether)-polystyrene found that the cloud point temperature is decreased by several °C upon exposure of the mixture to an electric field [RG79].

[1] This Chapter and its figures have been published in modified form. [KKKB15], Reprinted (adapted) with permission from C. C. Kathrein, W. K. Kipnusu, F. Kremer, and A. Böker, Birefringence Analysis of the Effect of Electric Fields on the Order-Disorder Transition Temperature of Lamellae Forming Block Copolymers, *Macromolecules* **2015**, *48*, 3354-3359. Copyright 2015 American Chemical Society.

In contrast to the experimental results, classical thermodynamics predict the evocation of phase separation by homogeneous electric fields [Onu95, SBMG80, DK65, WF93, Orz98]. The influence on the transition temperature is expected to merely lie in the millikelvin range, rendering the effect unsuitable for any application. Gunkel et al. additionally considered the non-mean field effect of homogeneous electric fields on composition fluctuations in symmetric diblock copolymer melts which likewise yielded a shift in the opposite direction than observed experimentally. An example calculation on poly(styrene)-*block*-poly(methyl methacrylate) predicted an upward shift in the critical temperature by 2.5 °C upon application of an electric field of 40 V/μm [GSTAT07]. Due to the contradiction in experimental and theoretical results the cause of the electric field-induced mixing is heretofore ambiguous.

Tsori concluded that the difference in dielectric contrast $\Delta\epsilon$ between the two blocks not taken into account in the calculations stated above is the dominating parameter when mixing microphase separated BCPs by exposure to an electric field in close vicinity to the T_{ODT}. Furthermore, the large molecular weight was anticipated to be the cause of the enhanced effect the electric field exerts on the transition temperature of polymeric samples [Tso09]. The T_{ODT} was presumed to be lowered according to $\Delta T_c \propto N v_0 \frac{\Delta\epsilon^2}{\overline{\epsilon}} E_0^2$ where N denotes the degree of polymerization, $\Delta\epsilon$ is the difference in dielectric permittivity between the two BCP constituents, E_0 defines the applied electric field strength, $\overline{\epsilon}$ is the mean dielectric permittivity of the solution, and v_0 is the monomer volume [Tso09]. The experimental evidence for these theoretical considerations is still pending.

This chapter reports a detailed birefringence analysis of the effect of dielectric contrast $\Delta\epsilon$ and chain length on the electric field-induced shift in T_{ODT} and compares the obtained results to theoretical considerations and previously performed experiments. With the results presented in this study, previous findings can be explained and the understanding of the effect of electric fields on the phase diagram of block copolymers is greatly enhanced. The reported large shifts, induced in the transition temperature, facilitate the reversible switching of optical- and structural properties of a material in a large temperature range by simple application of an electric field. With the findings presented in this chapter the temperature range of switchability can be tuned exactly. This could find application in future devices but also has to be taken into account when the effect is not favorable. Especially, during the preparation of thin film samples by solvent vapor annealing or thermal annealing the distance from the order disorder transition temperature has a crucial influence on the obtained structure.

4.2. Experimental

4.2.1. Materials and Sample Preparation

The lamella forming diblock copolymers poly(styrene)-*block*-poly(isoprene) (SI), poly-(styrene)-*block*-poly(2-vinylpyridine) (SV), poly(styrene)-*block*-poly(*tert*-butyl methacrylate) (ST) and poly(styrene)-*block*-poly(hydroxy ethyl methacrylate)-*block*-poly(methyl methacrylate) (SHM) were synthesized by sequential living anionic polymerization [HUM99]. The short poly(hydroxy ethyl methacrylate) block of SHM mixes with the poly(methyl methacrylate) block allowing the BCP to be treated as a diblock [BKE*02]. The polymers utilized in this study are listed in Table 4.1. The subscripts mark the weight fractions of the blocks and the superscripts denote the averaged molecular weight in kg/mol.

Table 4.1.: Investigated block copolymer solutions in THF. T_{ODT} = 40 °C at E = 0 kV/mm.

Polymer	$\frac{M_w}{M_n}$	conc. wt% (polymer)
$S_{46}I_{54}^{108}$	1.05	32.0
$S_{52}I_{48}^{80}$	1.02	36.0
$S_{50}I_{50}^{50}$	1.04	42.9
$S_{47}V_{53}^{80}$	1.00	37.0
$S_{54}V_{46}^{99}$	1.05	34.2
$S_{67}V_{33}^{115}$	1.03	32.0
$S_{46}H_4M_{50}^{134}$	1.06	32.8
$S_{47}H_{10}M_{43}^{82}$	1.06	40.5
$S_{55}T_{45}^{117}$	1.04	34.5

Concentrated solutions (32-43 wt%) of the block-copolymers in the non-selective good solvent tetrahydrofuran (THF) were prepared [HCLB98, EK04]. For comparability all samples were adjusted to a T_{ODT} of 40 °C at E = 0 kV/mm. The polymer concentration in solution is given in Table 4.1.

4.2.2. Birefringence Measurements

Measurements were performed *in-situ* in the home-built capacitor described in Chapter 3 with an Exicor 150 AT birefringence measurement system from Hinds Instruments which allowed high speed measurement of the optical retardation and fast axis orientation with

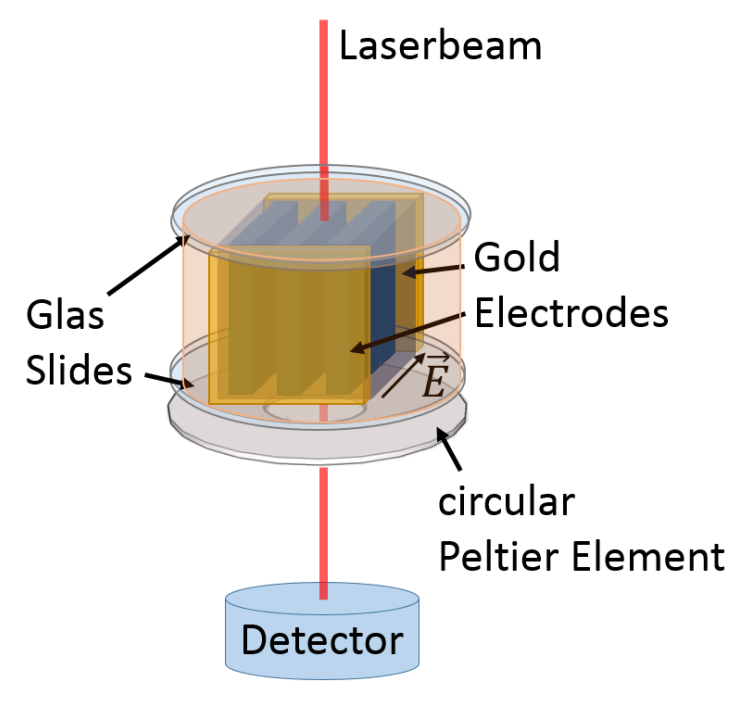

Figure 4.1.: Schematic illustration of the sample setup used for the birefringence measurements.

high accuracy and resolution. A schematic illustration of the sample setup is given in Figure 4.1. The block copolymer solution was sandwiched between two gold electrodes with an electrode spacing of 2 mm. The electrodes were cased in polyether ether ketone (PEEK) and had a length of 1.5 cm. The capacitor was tightly sealed to prevent solvent evaporation. Two glass slides covered the gold electrodes making it possible to directly measure the birefringence signal in solution when the voltage was applied. The laser beam (λ = 632.8 nm) with a measurement spot size of 1 mm traversed the sample directly between the two gold electrodes perpendicular to the electric field vector. To preclude an effect by fringe fields close to the electrode edges all measurements were performed in the middle of the capacitor. A volume of 1 mm × 1 mm × 5 mm was detected by the laser beam. Heating and cooling rates (0.45 °C/min and 0.25 °C/min) were controlled precisely by a circular Peltier element directly beneath the capacitor. Changes in temperature were measured in solution via a PT100 thermo sensor with a temperature resolution of ±0.1°C covered with thin glass. The sample was heated from 8 °C below to 8 °C above the respective T_{ODT} of each sample. Upon heating the phase retardation Γ was monitored as a function of block copolymer solution temperature. The T_{ODT} of the BCP samples was measured upon application of electric fields with

strengths between 0 kV/mm and 5 kV/mm. The voltage across the capacitor and the current were monitored during the experiment and, no current flow was observed. To exclude systematic errors, the different electric field strengths were applied in random sequence. For determination of the error each measurement was repeated five times.

4.2.3. Broadband Dielectric Spectroscopy Measurements

The relative dielectric permittivities of the homopolymers were measured by broadband dielectric spectroscopy (BDS) [KS02] at a temperature of 41 °C, which lies in the range of the T_{ODT} measurement. 100 μm thick films of the homopolymers from melt state were sandwiched between platinum electrodes separated by glass spacers.

4.3. Results and Discussion

4.3.1. ODT Determination

BCP melts of molecular weights comparable to the ones analyzed exhibit T_{ODT}s near or above their decomposition temperature. The dissolution of the copolymers in neutral solvents significantly lowers the T_{ODT} compared to the pure bulk samples circumventing this difficulty. Fredrickson and Leibler derived a theory to describe the microphase separation behavior of BCPs in non-selective good solvents and revealed that the theories, valid for the molten state, were also a good approximation for BCPs in solution [FL89]. The T_{ODT} of the BCP sample and the polymer concentration are linearly dependent [SPR*13, HT72, LPJ*95, HL98]. For comparison, the concentration of the BCP samples was adjusted to obtain a T_{ODT} of 40 °C at E = 0 kV/mm. Small angle x-ray scattering (SAXS) measurements confirmed that all samples exhibit a lamella microstructure in solution below T_{ODT}.

Due to its high accuracy and high sensitivity, birefringence was chosen to determine the T_{ODT}. In 1992, Amundson [AHPQ92] and Balsara [BPS92] demonstrated that the T_{ODT} of diblock copolymers can be detected easily by measuring the decrease in birefringent phase retardation upon heating through the T_{ODT} of lamella forming poly(styrene)-*block*-poly(methyl methacrylate) (SM) as described in detail in the previous chapter. Despite this fact, the majority of studies were performed by synchrotron SAXS or neutron scattering (SANS). Birefringence measurements have the advantage of being inexpensive, non-destructive, and with high-throughput capacity allowing the analysis of a higher quantity of samples. Figure 4.2 shows the evolution of measured phase retardation upon heating a highly concentrated solution of $S_{46}I_{54}^{108}$ (32.0 wt%) in THF through the T_{ODT} without an electric field (light gray circles) and under application of

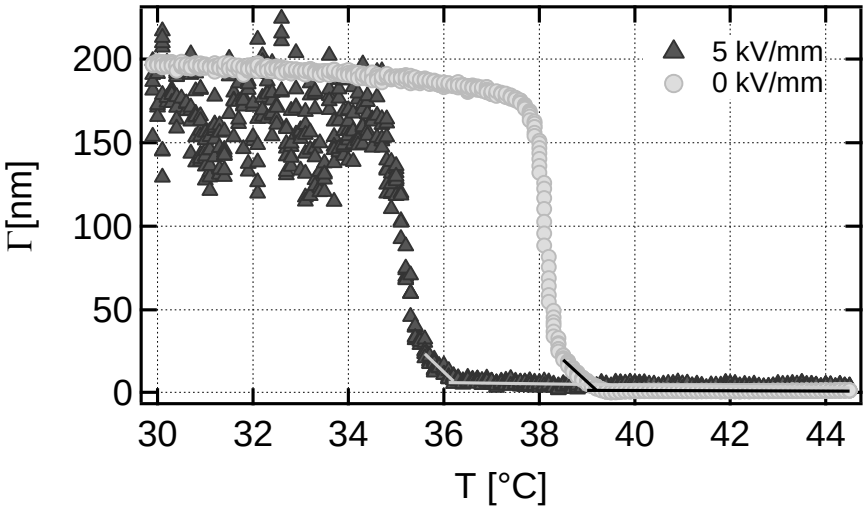

Figure 4.2.: Evolution of the birefringent phase retardation (Γ) of a sample of $S_{46}I_{54}^{108}$ (32.0 wt%) in THF as a function of temperature upon heating through the T_{ODT} at 5 kV/mm (dark gray triangles) and at 0 kV/mm (light gray circles). This figure was adapted from Ref. [KKKB15].

an electric field of 5 kV/mm (dark gray triangles). The birefringent phase retardation is plotted against the temperature. A downward shift in the transition temperature with increasing field strength was observed for all samples. Due to its optical anisotropy the lamella microstructure shows a high degree of form birefringence. A higher degree of ordering yields an increased birefringence signal [AHQS93, AHPQ92]. Upon heating a slight decrease in the phase retardation signal was recorded when no electric field was applied to the sample. This can either be attributed to a reorganization of lamella domains over time [BPS92] or to lamella softening upon approaching the order-disorder transition (ODT) [RBA*95]. When an electric field was applied fluctuations in the phase retardation signal were observed as long as the sample was in the phase separated state. These fluctuations were less pronounced the lower the electric field strength was. The monitored fluctuations most probably arise from local composition variations induced by the electric field. They are the cause for a higher amount of dielectric interfaces oriented perpendicular to the direction of the electric field vector and hence contribute to the electrostatic energy penalty [OAWT14]. Approaching the T_{ODT}, a steep but continuous decrease in phase retardation was observed at all field strengths. In the disordered phase the sample is optically isotropic and therefore the phase retardation dropped down to minimal values upon entering it. To determine the T_{ODT} two linear functions were fitted to each curve as shown in Figure 4.2. The T_{ODT} corresponds to the intersection of the two linear fits. The high resolution in measured phase retardation (±0.01 nm) and

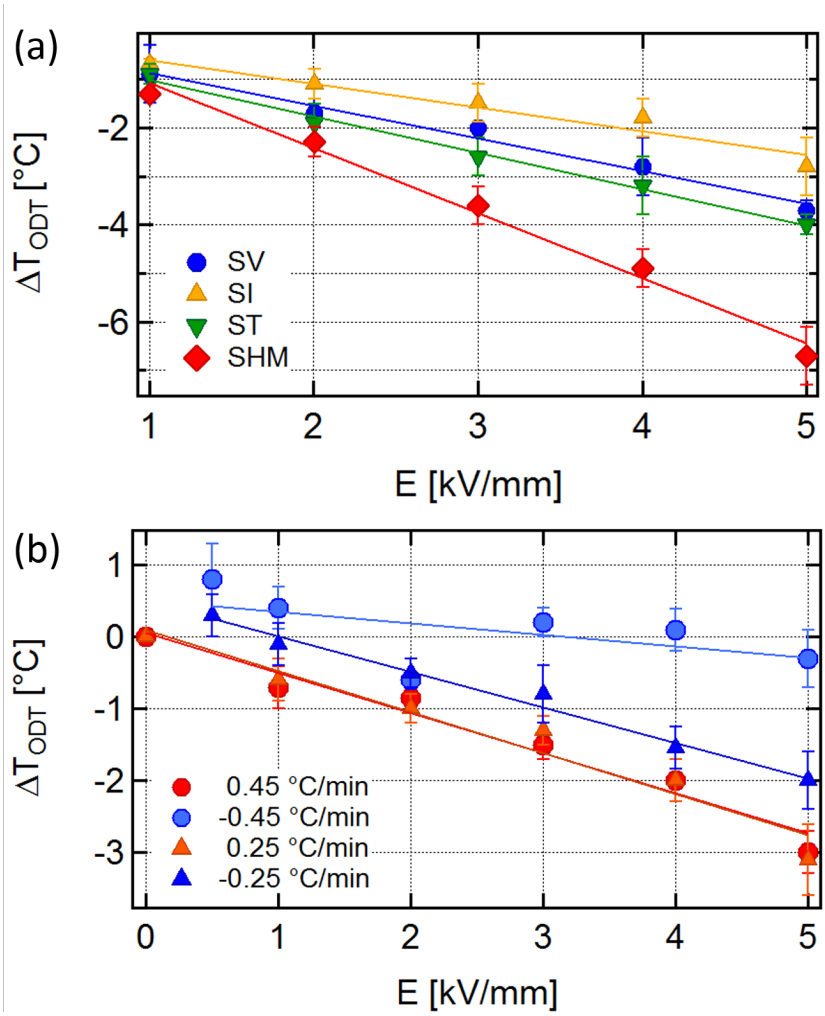

Figure 4.3.: (a) ΔT_{ODT} as a function of E for $S_{46}H_4M_{50}^{134}$, $S_{47}V_{53}^{80}$, $S_{46}I_{54}^{108}$ and $S_{55}T_{45}^{117}$.(b) ΔT_{ODT} upon heating and cooling as a function of E for $S_{46}I_{54}^{108}$ measured at two different heating and cooling rates. This figure was adapted from Ref. [KKKB15].

temperature ($\pm 0.1\,°C$) facilitated the precise determination of the T_{ODT} of the block copolymer sample.

4.3.2. Effect of Electric Field Strength

In a first set of experiments, the effect of the electric field strength on the shift in the transition temperature ($\Delta T_{ODT} = T_{ODT}(E) - T_{ODT}(0\ kV/mm)$) was evaluated. From electrostatic considerations [LLP04, Tso09] and observations for low molecular weight mixtures [WF93, Orz98] an increase in ΔT_{ODT} proportional to E^2 is expected. The

corresponding diagram is presented in Figure 4.3. In contrast to this our data implied a scaling as $\Delta T_{ODT} \propto E$. A possible reason for this discrepancy could be the very high electric field strengths applied during the measurement. Given that the analyzed field strength range only lies between 1 kV/mm and 5 kV/mm it might not be sufficiently large to determine the correct exponent. Onuki predicted the electric field dependency scaling as $E^{1.6}$ in the limit of strong electric fields as applied in our experiments while for weaker fields a dependency proportional to E^2 is expected [RZ04]. A further reason for the observed discrepancy could be a slight conductivity in the THF. In this case a scaling with $E\rho$ would be expected where ρ is the charge density.

4.3.3. Influence of Heating- and Cooling Rates

To exclude that the shift in transition temperature is merely a kinetic effect a 32 wt% sample of $S_{46}I_{54}^{108}$ in THF was measured at different heating and cooling rates. In Figure 4.3 (b) ΔT_{ODT} is plotted against the electric field strength applied upon heating and cooling. The red data points are the values in phase transition temperature shift obtained upon heating. The blue data points were acquired during the corresponding cooling cycle. The shift in transition temperature was monitored in dependency of the heating rate. When the temperature was altered at a rate of 0.45 °C/min a discrepancy between the electric field-induced shifts of the transition temperature obtained from heating and cooling was observed. This hysteresis diminished at a heating rate of 0.25 °C/min. Here the same shift in T_{ODT} was monitored upon heating and upon cooling. As reported by Amundson a critical domain size is required for the electric field to effectively interact with the BCP [AHD*91]. At high cooling rates this critical domain size is not reached until the temperature is already below the actual value at which the phase transition would take place. Therefore, the shift can merely be monitored upon cooling at very low rates. The shift in T_{ODT} upon heating was found to be independent of the heating rate.

4.3.4. Effect of Chain Length

To evaluate the effect of chain length, three different samples of SI and SV of differing molecular weights were analyzed. In Figure 4.4 the shift in the T_{ODT} upon application of an electric field strength of 5 kV/mm is plotted against the molecular weight of the block copolymer samples. While nearly the same shift was observed for $S_{46}I_{54}^{108}$ and $S_{46}I_{54}^{80}$, the sample with the lowest molecular weight ($S_{50}I_{50}^{50}$) showed a decreased shift in T_{ODT}. For SV the situation differs. Here ΔT_{ODT} increased with chain length in the observed molecular weight range. From the data it was concluded that $\Delta T_{ODT} \propto N$ as it was

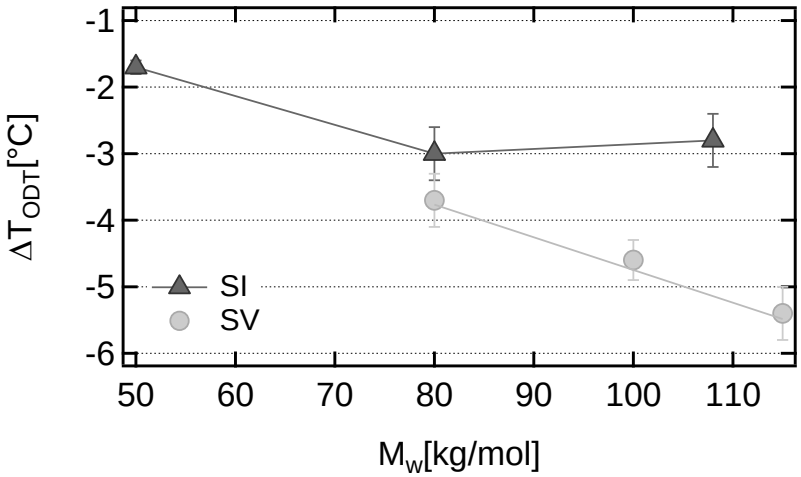

Figure 4.4.: The electric field-induced shift in the T_{ODT} upon application of an electric field of 5 kV/mm as a function of molecular weight for SI and SV. This figure was adapted from Ref. [KKKB15].

predicted by Tsori. The dependency on chain length only seems to be valid until a certain BCP specific molecular weight is reached at which the maximum ΔT_{ODT} is attained. The observed chain length dependency accounts for the much higher shifts in the transition temperatures found for polymeric systems [RG79, SSSB09] than for low molecular weight mixtures upon exposure to electric fields. For the latter, a downward shift in the critical temperature (T_c) by merely a few millikelvins was observed [WF93, Orz98].

4.3.5. Effect of Dielectric Contrast

This section focuses on the effect of the dielectric contrast $\Delta\epsilon$ on the electric field-induced shift in the T_{ODT}.

To determine the dielectric contrast between the blocks the dielectric permittivities of the homopolymers which correspond to the individual block copolymer constituents were measured by BDS.[2] The isothermal plots of the real part ϵ' of the complex dielectric permittivity of the homopolymers are shown in Fig. 4 (a). The real part of the complex dielectric permittivities at 0.1 Hz for all analyzed homopolymers is given in Table 4.2.

[2]BDS measurements were performed and evaluated by Wycliffe K. Kipnusu from the group of Prof. Dr. Friedrich Kremer at the Institut für Experimentelle Physik, University of Leipzig, Germany.

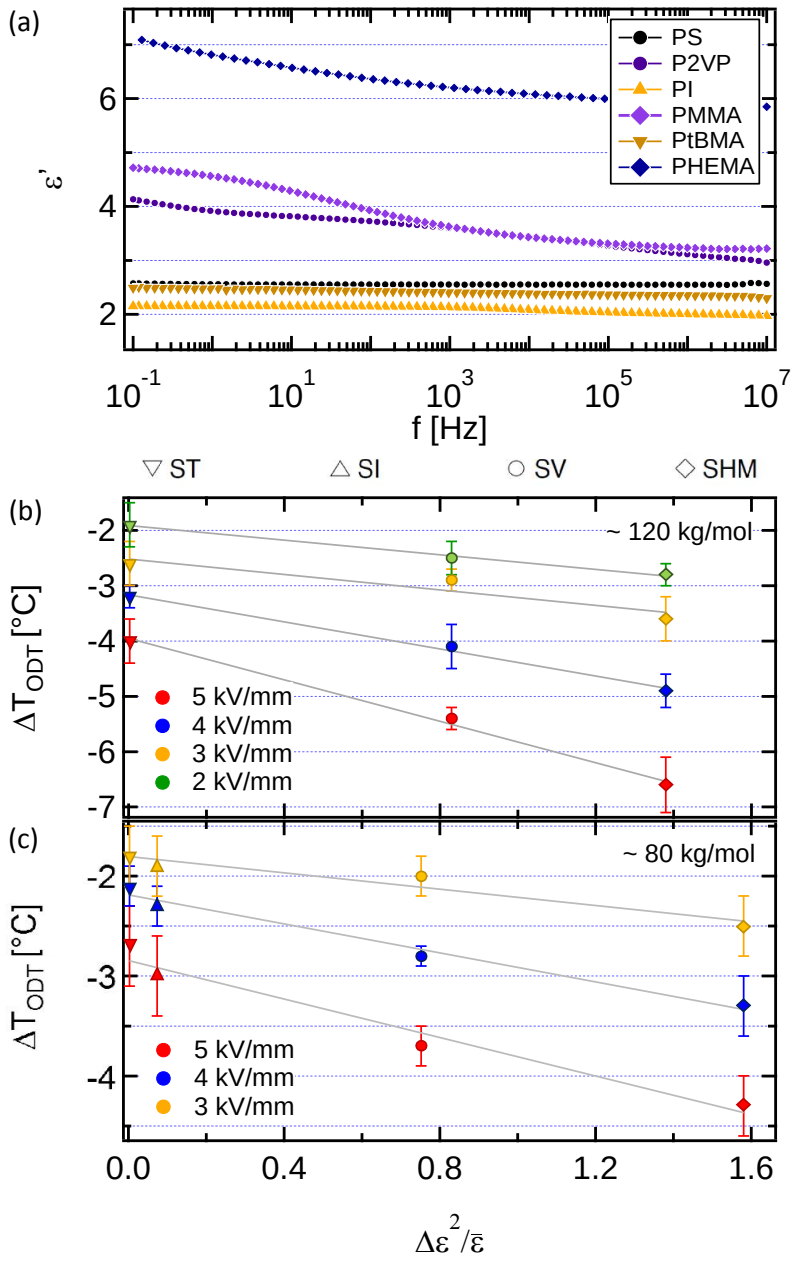

Figure 4.5.: (a) The real part of the complex dielectric permittivities of the homopolymers Poly(styrene)(PS), Poly(2-vinylpyridine)(P2VP), Poly(isoprene)(PI), Poly(methylmethacrylate)(PMMA), Poly(*tert*-butyl methacrylate)(PtBMA) and Poly(hydroxy ethyl methacrylate)(PHEMA) is plotted against the measurement frequency in Hz measured by dielectric spectroscopy at a temperature of 41 °C. (b-c) The electric field-induced shift in the T_{ODT} as a function of $\Delta\epsilon^2/\bar{\epsilon}$ for BCPs of a molecular weight of about (b) 120 kg/mol and (c) 80 kg/mol. The symbols denote different BCPs as indicated above (b), 52the colors mark different field strengths. This figure was adapted from Ref. [KKKB15].

Table 4.2.: Real part of the complex dielectric permittivites of the homopolymers measured by Broadband Dielectric Spectroscopy (BDS) at 0.1 Hz.

Homopolymer	ϵ' (0.1 Hz, 41 °C)
PHEMA	7.09
PMMA	4.72
P2VP	4.13
PS	2.57
PtBMA	2.49
PI	2.15

The dielectric permitivitites of the poly(hydroxy ethyl methacrylate)-*block*-poly(methyl methacrylate) blocks H_4M_{50} and $H_{10}M_{43}$ were calculated from the measured data according to Looyengas mixing rule [Loo65]. The resulting dielectric contrast which was calculated according to $\Delta\epsilon = \epsilon'_A - \epsilon'_B$ for the BCPs at 0.1 Hz is given in Table 4.3. Since the measurements were performed in DC electric fields, the lowest frequency was chosen for analysis of the data.

Table 4.3.: Dielectric contrast $\Delta\epsilon = \epsilon'_A - \epsilon'_B$ between the block copolymer constituents.

Block copolymer	$\Delta\epsilon$ (0.1 Hz, 41 °C)
PS-PI	0.42
PS-P2VP	1.6
PS-PtBMA	0.08
PS-PHEMA-PMMA[134]	2.3
PS-PHEMA-PMMA[82]	2.5

ΔT_{ODT} was plotted against the square of the dielectric contrast between the block copolymer constituents divided by the mean dielectric permittivity of the sample $\Delta\epsilon^2/\bar{\epsilon}$ for electric field strengths between 2 kV/mm and 5 kV/mm for polymers of molecular weights around 80 kg/mol (Figure 4.5(c)) and 120 kg/mol (Figure 4.5(b)). The effect of the electric field on the transition temperature is more pronounced with higher dielectric contrast between the block copolymer constituents. The results clearly demonstrate that the dielectric contrast is a dominating factor which promotes mixing in BCPs when exposed to electric fields in close vicinity to the T_{ODT}.

Schoberth et al. showed that the shift in the transition temperature scales with the initial lamella orientation with respect to the electric field vector φ as $\Delta T_{ODT} \propto cos^2\varphi$ [SPR*13]. These experimental findings are in accordance with a theory published previously by Amundson and coworkers [AHQS93]. Under the precondition that the dielectric

permittivities of two liquids differ, their dielectric interfaces become instable in the presence of an electric field. When these interfaces are normal to the field vector, they possess a maximum excess in free energy density ΔG compared to those parallel to the electric field vector. Dielectric interfaces not parallel to the electric field are therefore rendered instable according to $\Delta G \propto \Delta\epsilon^2 E^2 cos^2\varphi$, where φ is the angle between the applied electric field $\mathbf{E}$ and the normal to the lamella interfaces $\hat{\mathbf{n}}$. The dependency of the electric field-induced ODT shift on $\Delta\epsilon$ presented here supports these results and the importance of this effect for the phase diagram of BCPs under the influence of electric fields. The variations in composition observed during the phase retardation measurement (Figure 4.2) increase the amount of dielectric interfaces which are not parallel to the electric field vector. Due to this electrostatic energy penalty which scales with the dielectric contrast between the block copolymer constituents electric field-induced mixing is observed. Furthermore the obtained results indicate that there is a further contribution, independent of the dielectric contrast between the blocks, which likewise induces mixing. This can be concluded from the relatively large ΔT_{ODT} obtained for PS-PtBMA for which the dielectric contrast merely amounts to 0.08. For contributions to the mixing under the influence of strong electric fields we refer to a paper recently published by Orzechowski et al. [OAWT14] in which the downward shift of T_c was estimated from mean field theory taking into account the linear and quadratic components of an expansion of the relation between the dielectric constant and the composition of the mixture.

4.4. Conclusion

For the first time the effect of homogeneous DC electric fields on the T_{ODT} of concentrated solutions of various BCPs was analyzed. Electric field-induced mixing can be induced in a relativly large temperature interval in the vicinity of the ODT. The main parameters determining the degree to which the T_{ODT} is shifted by the electric field are the difference in dielectric permittivity $\Delta\epsilon$ between the individual blocks and the chain length. In the measured field strength range the shift is proportional to E for all BCPs analyzed. The results are in accordance with previously published theoretical considerations by Amundson and Tsori. Both predicted a destabilization of interfaces between two dielectric media of differing dielectric permittivity proportional to $\Delta\epsilon^2$ when exposed to an electric field. Tsori concluded that the chain length is a relevant factor determining the degree to which the T_{ODT} is shifted upon application of the electric field.

5. Block copolymer/ CdSe Quantum Dot Composites

5.1. Introduction and Theoretical Background

Block copolymer/nanoparticle composite materials have gained considerable interest in the past decade due to their wide variety of potential applications. While the nanoparticles exhibit interesting catalytic, [JBCM03] optical, [MUY*02, BLB03, BT04] mechanical, [BLB03] or magnetic properties, [THD02] block copolymers, can effectively control particle location and patterns [TGMB01, TGMB02]. Utilizations include photonic band gap materials, [TGMB02, SHGC05] solar cells, [HDA02] and catalytic [JBCM03] and biomedical devices [KNP07].

The properties of the composite materials are not only determined by particle size and shape, but also by the spatial distribution within the polymer matrix. Therefore, precise control over the particle assembly and orientation is required. Block copolymers, which are capable of forming a rich variety of structures in a size range of 10-100 nm, are the ideal scaffold for the assembly. Through selective insertion into one block copolymer domain, highly ordered arrays of nanoparticles are producible. The crucial parameter determining the affinity to the individual block copolymer constituents is the chemical surface modification of the particle [CKKP05]. The localization within the domain is mainly influenced by its core diameter and the grafting densities and molecular weights of the ligands [BMT05].

Although much effort has been given to understand the effects of electric fields on the block copolymer microstructure, [PRS*11, BEH*03, SSR*08, LPR*12] only few studies exist on how nanoparticles influence the electric field-induced alignment. Cell dynamic system simulations by Yan and coworkers revealed that the nanoparticles alter the morphology and reorientation dynamics of block copolymers under the influence of electric fields [YSB10]. Furthermore, Yan et al. anticipated that the inclusion of nanoparticles leads to an alteration in alignment mechanism with a preference of NG over RG [YSB09]. Liedel et al. showed that selectively-confined gold nanoparticles lower the critical field strength necessary to align polystyrene-*block*-poly(2-vinylpyridine) thin films [LSP*13].

Foundation of the realignment process under application of an electric field is the difference in dielectric permittivity $\Delta\epsilon = \epsilon_A - \epsilon_B$ between the copolymer blocks. Dielectric interfaces perpendicular to the electric field vector are electrostatically unfavorable compared to those parallel to the external field. The energy difference between the two orientations is proportional to the second power of the dielectric contrast $(\Delta\epsilon)^2$ between the two blocks [Tso09]. To obtain the energetically favorable orientation with interfaces parallel to the electric field vector, block copolymers can undergo three different microscopic mechanisms of alignment: nucleation and growth (NG), reorientation of grains (RG), [BEH*02b, PSZ09] and selective disordering (SD). Selective disordering is merely found in close vicinity to the order-disorder transition temperature T_{ODT} and therefore will not be discussed in this chapter. For a detailed explanation it is refered to an article by Ruppel et al. [RPL*13] A precise description of the two other reorientation mechanisms will be given in the course of this chapter.

This chapter presents the first reported experimental studies of the influence of nanoparticles on the realignment kinetics and mechanisms of a concentrated diblock copolymer solution in *non-selective* solvents exposed to electric fields. It is analyzed whether the nanoparticles are capable of switching the reorientation mechanism of electric field-induced alignment as anticipated by Yan and coworkers. Polystyrene-*block*-poly(isoprene) (SI) (33.2 wt%) in toluene was chosen as a model system due to the fact that its alignment kinetics and reorientation mechanisms under exposure to an electric field have been intensively analyzed via synchrotron small angle x-ray scattering (SAXS) [BEH*02b, SBZ*05]. Therefore, the comparison to previously performed experiments is straightforward. Oleylamine functionalized CdSe quantum dots were incorporated into the lamella-forming block copolymer. The oleylligands have previously been shown to favor the poly(isoprene) domain over poly(styrene), leading to a selective confinement of the particles within the poly(isoprene) matrix [KLL*08]. The quantum dots were chosen since they show no absorption at the wavelength of the laser beam ($\lambda = 632.8$ nm).

5.2. Experimental

5.2.1. Sample Preparation

Lamella forming poly(styrene)-*block*-poly(isoprene) of a molecular weight of 180 kg mol^{-1} and a polydispersity index of 1.05 was synthesized by sequential living anionic polymerization. The weight fraction of the poly(styrene) block was determined to be 0.46 by ^1H-NMR spectroscopy. 33.2 wt% solutions of the block copolymer in the *non-selective* good solvent toluene were prepared. Oleylamine-stabilzed CdSe quantum dots with a peak emission at 525 nm and a particle diameter of 2.8 nm in hexane solution were pur-

chased from STREM Chemicals Inc. Through addition of twice the amount of ethanol absolute to the particle solution the quantum dots were precipitated. Subsequently, the mixture was centrifuged at 11000 rpm for 10 min. The hexane/ethanol mixture was decanted and the particles were dried under high vacuum for 2 hours. Afterwards, the quantum dots were redissolved in toluene which was then given to the block copolymer to attain concentrated solutions with a polymer concentration of 33.2 wt% and nanoparticle loadings of 0 wt%, 1 wt%, 2 wt%, and 3 wt% with respect to the amount of polymer.

5.2.2. Birefringence Measurement

Time- and temperature-resolved *in-situ* birefringence measurements were performed with an Exicor 150 AT birefringence measurement system from Hinds Instruments which measured the optical retardation with high accuracy (0.01 nm) and time resolution allowing the acquisition of up to three data points a second. The electric field was applied in a home-built capacitor described in the previous chapters. The block copolymer solution was sandwiched between two gold electrodes of a length of 1.5 cm with an electrode spacing of 2 mm and a path length of light of 5 mm. The laser beam with a diameter of 1 mm and a wavelength of 632.8 nm propagated through the solution directly between the gold electrodes perpendicular to the electric field vector. Measurements were performed in the middle of the capacitor to avoid any influence by fringe fields close to the electrode edges. Above and below the capacitor, two glass slides prevented solvent evaporation which were tightly screwed to the sample cell. The temperature of the sample was precisely controlled using a circular Peltier element which was placed directly underneath the capacitor. Additionally, the temperature was monitored in solution via a PT-100 thermosensor covered with thin glass. To prevent solvent degradation of the sample cell, this was built from polyether ether ketone (PEEK).

5.2.3. Determination of the Reorientational Time Constants

The sample was heated to 10 °C above the T_{ODT} and subsequently cooled to 10 °C below the T_{ODT} at a heating and cooling rate of 1 °C min^{-1}. While the lamella phase is characterized by a strong degree of form birefringence, the disordered phase is optically isotropic. Therefore, the T_{ODT} can be determined by monitoring the decrease in phase retardation as a function of temperature. Afterwards, the block copolymer solution was quickly adjusted to the desired temperature. After cooling, the sample exhibits a microphase separated, isotropic multidomain structure with no preferred direction of orientation. Upon application of an electric field of 1 kV mm^{-1}, the increase in phase

retardation is measured as a function of time. The data was fitted by a single exponential function to retrieve the overall reorientational time constant τ.

5.3. Results and Discussion

5.3.1. Analyzing Block Copolymer Reorientation Kinetics via Birefringence.

In the following we will discuss how birefringence measurements can be utilized to analyze the reorientation kinetics of block copolymers as demonstrated by Amundson and coworkers [AHPQ92, AHQS93].

Figure 3.3 of Chapter 3 displays a simplified illustration of a lamella stack, it's optic axis and the direction of the fast and the slow axis. A lamella microdomain pattern is characterized by an uniaxial optical anisotropy resulting in form birefringence. The axis of symmetry, also known as the optic axis, which is indicated by the green arrow in Figure 3.3 , is perpendicular to the lamella interfaces. Components of light propagating through the sample are exposed to different refractive indices n_o and n_e depending on whether their direction of polarization is perpendicular (ordinary wave (o), direction indicated by blue arrows) or parallel (extraordinary wave (e), direction indicated by red arrows) to the optic axis. In the case of negative uniaxial birefringence, as found in a lamella assembly, the fast axis coincides with the optic axis while the slow axis is perpendicular to it. Light polarized along the slow axis will be refracted with a refractive index n_o while light polarized along the fast axis is exposed to a refractive index n_e. Therefore, the ordinary wave will experience a phase retardation Γ with respect to the extraordinary wave [BW59]. The magnitude of the resulting phase retardation Γ amounts to Eq. 5.1.

$$\Gamma = 2\pi \frac{l}{\lambda} \Delta n^0 \langle \overline{\Psi}^2 \rangle \sin^2 \theta \tag{5.1}$$

Here l is the optical path length, λ describes the wavelength of light while passing through the medium, $\langle \overline{\Psi} \rangle$ denotes the periodic lamella pattern, and θ is the angle between the propagation direction of light and the unit wave vector of the lamella pattern $\hat{e}_k$. $\Delta n = n_e - n_o$ is the birefringence of the sample. The overall birefringence strength of a block copolymer is dependent on its degree of phase separation. In the strong segregation limit (SSL) the interfaces are sharp and a maximum form birefringence strength Δn^0 is attained. [AHPQ92] For a more detailed description of the birefringence of block copolymers we refer to chapter 3.

In Figure 5.1 (a, b) the evolution of the phase retardation signal (Γ) upon exposing a sample with 0 wt% and 1 wt% of quantum dots to an electric field of 1 kVmm^{-1} is

plotted against time in seconds at three different temperatures. At the beginning of the measurement a phase retardation of around 0 nm is observed.

This is due to the fact that prior to application of the electric field, the block copolymer sample was heated to 10 °C above the order-disorder transition temperature (T_{ODT}) at which the lamella microstructure disintegrates and approaches the disordered phase. Subsequently, the samples were cooled to 10 °C below T_{ODT} at a cooling rate of 1 °C min^{-1}. After cooling, the sample exhibits an isotropic multidomain structure without any preferred direction of alignment as presented in Figure 5.1 (c). When light propagates through the sample, each region of coherence induces a small phase retardation depending on its size, degree of phase segregation, and orientation. Since these individual phase retardations are uncorrelated, the resulting overall Γ is near to zero. For a precise description we refer to section 3.1.3.4. (Birefringence of Optically Anisotropic Ordered Phases) of Chapter 3 of this thesis.

After an electric field of 1 kV mm^{-1} was applied, the electric field-induced reorientation process set in and an increase in Γ over time was observed. The degree of alignment of a block copolymer sample is described by the orientational order parameter P_2.

$$P_2 = \frac{3\langle \cos^2 \theta \rangle - 1}{2} \tag{5.2}$$

A macroscopically disordered sample is characterized by $P_2 = 0$ (Figure 5.1 (c)) while a maximum alignment of lamella interfaces parallel to the electric field vector corresponds to an order parameter of -1/2 (Figure 5.1 (d)). For perfect alignment perpendicular to the electric field vector $P_2 = 1$ is found (Figure 5.1 (e)). The effective overall birefringence strength of the block copolymer sample is directly proportional to the order parameter and amounts Eq. 5.3.

$$\Delta n = \Delta n^0 \langle \overline{\Psi}^2 \rangle P_2 \sin^2 \theta \tag{5.3}$$

Therefore, the phase retardation can be used as a direct measure to analyze the reorientation kinetics. To retrieve the overall reorientational time constant τ the data was fitted by a single exponential function $\Gamma = \Gamma_\infty + Ae^{(-t/\tau)}$.

As can be observed in Figure 5.1 (a, b) the maximum Γ values differ from each other after application of the electric field. The higher the temperature, the lower the overall attainable birefringence strength is after alignment. This can be attributed to the fact that the interfacial boundary between the block copolymer constituents becomes less defined in the weak segregation limit (WSL) upon approaching the order-disorder transition temperature.

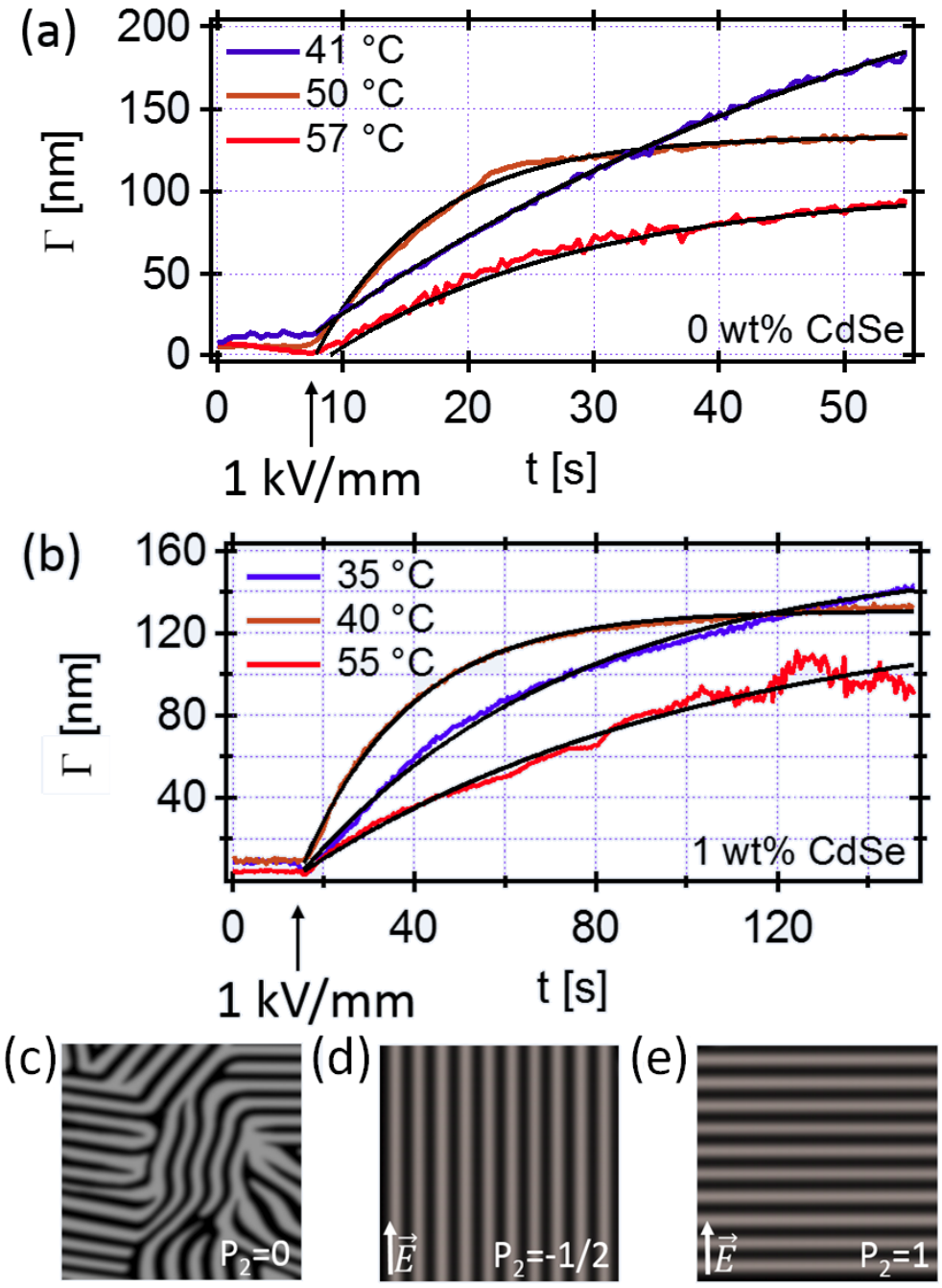

Figure 5.1.: Evolution of phase retardation of a sample of Poly(styrene)-*block*-poly(isoprene) (33.2 wt%) in toluene without (a) and with nanoparticles (b) upon application of an electric field of 1 kV mm^{-1} at different temperatures. The phase retardation Γ increases proportional to the order parameter of the sample. The data was fitted by a single exponential function (black line). (c, d) Schematic illustration of the lamella microstructure before (c) and after (d) electric field-induced alignment. (e) Schematic illustration of a lamella microstructure oriented perpendicular to the electric field vector. P_2 is the corresponding order parameter.

5.3.2. The Reorientation Mechanisms under Application of an Electric Field.

As stated above electric field-induced reorientation of block copolymer samples can proceed via three different mechanisms depending on the distance from the order-disorder transition temperature and the degree of prealignment in the sample. Previously the analysis of the time-evolution of the azimuthal intensity distribution of small angle x-ray scattering (SAXS) images upon inception of the electric field has been utilized to distinguish between the reorientation mechanisms [BEH*02b]. In the following we will compare the two mechanisms relevant to our study: reorientation of grains (RG) and nucleation and growth (NG) and explain which factors influence the reorientation behavior.

Well below the ODT, at lower temperatures, RG is the prevailing mechanism as reported by Böker et al. [BEH*02b] In this case, the orientation of entire grains rotates as demonstrated in Figure 5.2 (a). In the strong segregation limit (SSL), the average dimension of one region of coherence is larger and the formation of grain boundaries is thermodynamically unfavorable [AHD*91]. Therefore, the reorientation does not proceed via NG in this regime.

Nucleation and Growth (Figure 5.2 (b)) proceeds via the formation of nuclei of lamella with an enthalpically preferred orientation parallel to the electric field vector and their subsequent growth. The starting point for the nucleation are defects, such as, for example, dislocations. NG is the prevailing mechanism at elevated temperatures, in the vicinity of the order-disorder transition, where the segregation between the blocks is weaker [BEH*02b]. In this weak segregation limit (WSL), the energetic penalty induced by the creation of boundary interfaces is lower whereby small nuclei which have a large boundary area in comparison to their volume are more readily formed. Furthermore, this region is characterized by a higher defect density and mobility which also favors NG.

Compared to RG the reorientation through NG proceeds relatively slow whereby the time constants of reorientation at a given temperature can differ by an order of magnitude [SBZ*05].

Another important factor which greatly influences the reorientation of lamella domains under application of an electric field is the initial degree of order in the block copolymer sample. In misaligned samples, RG is the prevailing mechanism, while highly ordered block copolymers with lamella interfaces perpendicular to the electric field vector preferentially reorient via NG. [SBZ*05] The boundary between the two mechanisms is not sharp; at medium conditions both can coexist. Therefore, conditions prior to realignment are crucial. By heating the sample to 10 °C above the T_{ODT} and subsequent

cooling into the phase separated state, a macroscopically isotropic multidomain structure is generated with no preferred orientation. This ensures that the initial conditions of alignment are comparable at all temperatures and nanoparticle loadings.

Since the realignment behavior of the block copolymer system used in this study has been throughly analyzed via synchrotron SAXS the results described above are used to interpret the data of the birefringence measurements.

5.3.3. Analyzing the Switch in Reorientation Mechanism via Birefringence.

The reorientation kinetics of the block copolymer with different nanoparticle loadings (0 wt%, 1 wt%, 2 wt% , and 3 wt%) were analyzed via birefringence measurements at a field strength of 1 $kVmm^{-1}$ in a temperature range between 30 °C and 60 °C.

The large difference in the time constants of the two reorientation processes is exploited to determine the temperature at which NG is established as an alternative reorientation mechanism to RG [SBZ*05]. In the following, a description on how the switch in reorientation mechanism can be detected by birefringence measurements is given.

In Figure 5.2 (c) the determined reorientational time constants τ are plotted against the temperature for a sample with 0 wt% and 1 wt% CdSe nanoparticles. The reorientation kinetics are strongly dependent on the temperature of the sample. At first we will focus our discussion on the development of the reorientational time constants with increasing temperature of the sample with 0 wt% nanoparticles (black squares Figure 5.2 (c)). Between 28°C and 50°C τ decreases with rising temperature. In this low temperature regime all block copolymer domains reorient via RG. Upon raising the temperature, chain mobility is enhanced while the viscosity of the sample is lowered, leading to a faster reorientation. As long as all grains realign via RG, a decrease in τ proportional to the increase in temperature is found as expected. The fact that the reorientational constant increases again upon further temperature elevation between 50°C and 60°C can only be explained by the onset of a slower realignment mechanism, namely NG, in this region both mechanisms coexist. With increasing temperature, the slower NG mechanism is increasingly preferred over RG. Since the percentage of grains realigned via NG increases with temperature, τ rises upon temperature elevation. This increase in reorientational time constant with rising temperature is observed until the order disorder transition is reached. Therefore, it can be concluded that even at elevated temperatures the reorientation does not proceed via a pure NG process. If this were the case a renewed decrease in the reorientational time constants is expected. Reason for this is the misalignment in the sample prior to the electric field application which favors RG as an alignment mechanism over NG.

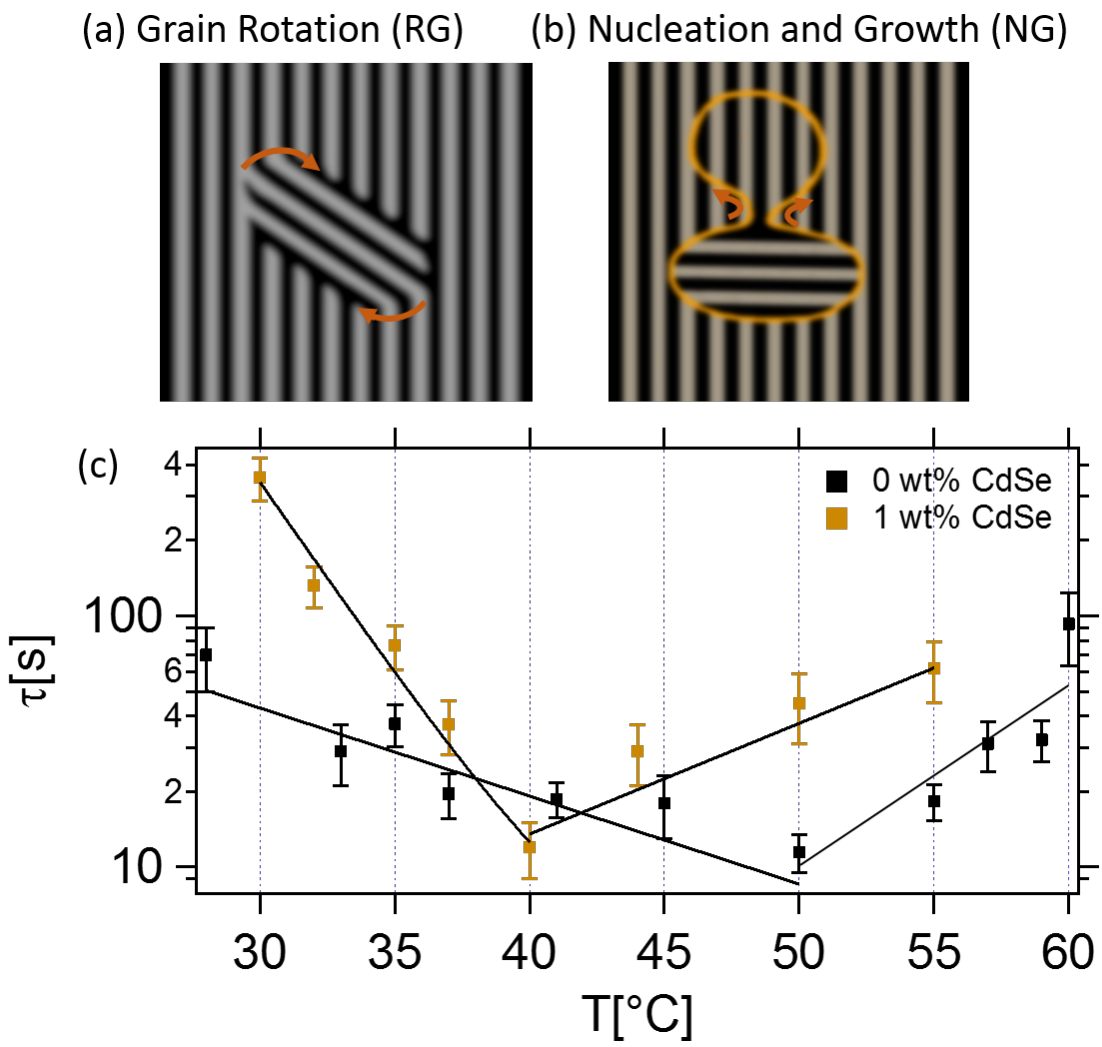

Figure 5.2.: (a, b) Schematic illustration of the two alignment mechanisms Grain Rotation (a), and Nucleation and Growth (b). (c) Time constants of the electric field-induced reorientation at 1 kV mm^{-1} for a sample of Poly(styrene)-*block*-poly(isoprene) (33.2 wt%) in toluene without nanoparticles (black squares) and with 1 wt% of CdSe quantum dots (orange squares) as a function of temperature.

These findings are in agreement with previously published synchrotron SAXS measurements on the temperature dependence of the electric field-induced reorientation of SI in concentrated solutions of toluene [BEH*02b]. Birefringence measurements have the advantage of being easily accessible and straightforward while at the same time offering a sufficient time resolution to capture the reorientation kinetics of block copolymers exposed to electric fields.

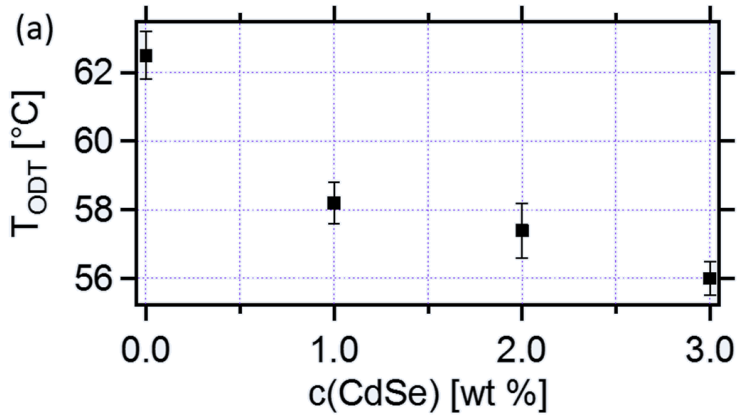

Figure 5.3.: (a) Order-disorder transition temperature of a solution of SI (33.2 wt%) in toluene as a function of nanoparticle concentration. The poly(isoprene) confined CdSe quantum dots lower the order-disorder transition temperature of the sample.

5.3.4. The Effect of Nanoparticles on the Reorientation Mechanism and Kinetics.

Upon comparison of the measurements with (yellow squares Figure 5.2 (c)) and without particles (black squares Figure 5.2 (c)), it becomes apparent that a low nanoparticle amount (1 wt%) is already sufficient to lower the temperature at which NG sets in as an additional mechanism by 10 °C down to a temperature of 40 °C. The results presented here are the first experimental evidence that the reorientation behavior is altered through the confinement of quantum dots.

The incorporation of nanoparticles into block copolymers lowers the order-disorder transition temperature (T_{ODT}) [JGG*02]. To exclude that, the observed effect can merely be attributed to this shift in T_{ODT}, T_{ODT} of the samples was plotted against the quantum dot concentration (Figure 5.3 (a)). At a nanoparticle loading of 1 wt% the T_{ODT} is merely lowered by 4.5 °C compared to the sample without particles. Therefore, this effect alone is not sufficient to explain the 10 °C decrease in the temperature at which NG sets in as a further mechanism of realignment. Clearly the interplay between increased defect density, and the lower T_{ODT} lead to a preference of NG over RG when nanoparticles are incorporated into the copolymer. The quantum dots serve as nuclei for their preferential phase and support the formation and coarsening of grains. The activation energy for the nucleation and growth process is decreased and NG becomes the thermodynamically preferred mechanism of realignment [ZS03].

5.4. Conclusion

In conclusion, *in-situ* birefringence measurements were applied to analyze the influence of quantum dots on the reorientation behavior of block copolymers upon inception of an electric field of 1 kV mm^{-1}. A method to determine the temperature at which NG sets in as an additional reorientation mechanism to RG apart from the established synchrotron SAXS measurements is presented. The birefringence measurements have the advantage of being inexpensive and easily accessible while at the same time offering a high time resolution to monitor the reorientation processes. The data presented here gives the first experimental evidence that the selective incorporation of nanoparticles into one block copolymer domain leads to a preference of NG over RG.

6. Mechanisms of the Electric field-induced Gyroid-to-Cylinder Phase Transition

6.1. Introduction

While electric fields can reorient uniaxial block copolymer phases [AHD*91, OHK*06, OHK*09, BSK*06, BEH*03, WLBSR06, WXLB*06, MLU*96, AHQS93, AHQ*94], cubic phases possess a certain amount of interfaces with an unfavorable angle to **E**, independent of their orientation. Their electrostatic energy cannot be reduced by structural reorientation. Hence, the exposure of cubic phases to electric fields results in an elongation of the unit cell in direction of **E**. If the electric field is of sufficient magnitude and the composition of the polymer is in vicinity of the phase boundary order-order transitions into uniaxial phases are observed [SPS*10, LHKZ07, PZ08, XZS*04, LZS06, Mat06, TTAL03, WCR08, WD08, PSR*15, LHKZ08, LHKZ09, LPH*13]. Schmidt et al. [SPS*10] reported the reversible electric field-induced gyroid-to-cylinder transition in a solution of polystyrene-*block*-polyisoprene but the mechanisms of the transition could not be resolved. In this chapter the mechanisms of the electric field-induced gyroid-to-cylinder transition and of the reformation of the gyroid phase after switching off the electric field in a solution of polystyrene-*block*-poly(2-vinylpyridine) in THF will be evaluated by time resolved *in-situ* synchrotron SAXS measurements. The results will be compared to previous experimental studies and calculations. A further objective of this study is to identify the conditions under which higher ordered gyroids can be obtained by evolving from an electric field-oriented cylinder phase.

6.2. Experimental

6.2.1. Sample Preparation and Experimental Procedure

Concentrated solutions (44.3 wt% (G1) and 46.3 wt% (G2)) of polystyrene-*block*-poly(2-vinylpyridine) (P2VP) with a molecular weight of 98 kg/mol and a volume fraction of P2VP of 77 v% in THF were prepared. For SAXS measurements the solutions were filled into the sample cell described in Chapter 3. Solutions of concentration G1 were exposed to homogeneous electric fields of 3 kV/mm, 4 kV/mm, and 5 kV/mm each at temperatures of 25 °C, 28 °C, 32 °C, and 36 °C.

6.2.2. Synchrotron SAXS Measurements

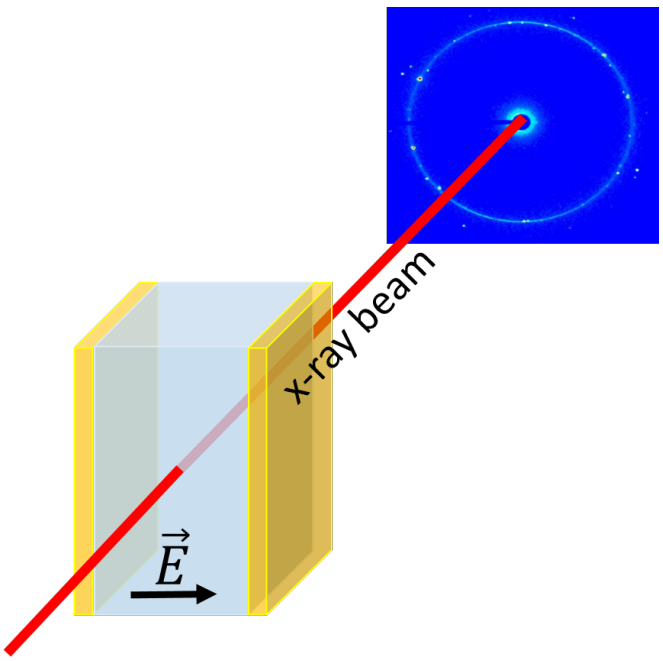

Figure 6.1.: Schematic image of the setup used for the SAXS measurements. The x-ray beam traverses the block copolymer sample directly between the electrodes, perpendicular to the electric field vector.

Measurements were performed in the sample cell described in Chapter 3. The x-ray beam traverses the block copolymer sample directly between the electrodes, perpendicular to the electric field vector as demonstrated in Figure 6.1. Time-resolved *in-situ* SAXS measurements were performed at the European Synchrotron Radiation Facility (ESRF) in Grenoble (France), at beamline ID02. The monochromatic beam at 12.5 keV had a spot size of 100 × 200 μm^2. A Kodak Frelon detector was used, whereby the sample to detector distance amounted 5 m. Before normalizing to incident beam intensity raw data were corrected for detector dark current and efficiency, sample absorption, and geometry. 2D SAXS data were processed by performing a radial integration to determine the q dependent scattering intensity. Locations of the Bragg peaks were determined via a Lorentz fit to the intensity vs q plots.

6.3. Results and Discussion

6.3.1. The Gyroid Phase

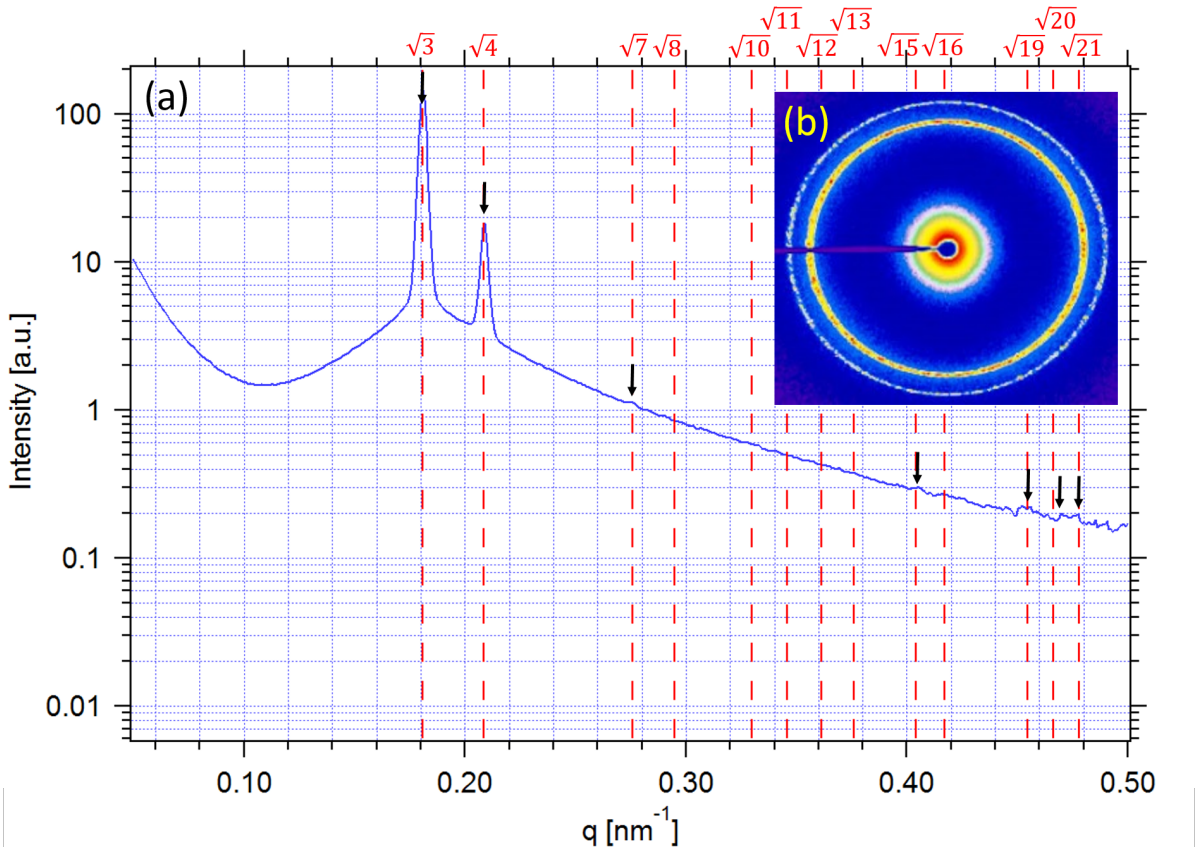

Figure 6.2.: (a) 2D SAXS scattering pattern and (b) Intensity vs q plot obtained by radial integration of the 2D scattering image. The dashed red lines mark the successive Bragg Peaks of a gyroid microstructure.

Prior to analyzing the effect of electric field, the microdomain structure formed in absence of an electric field is discussed. In Figure 6.2 the Intensity obtained by radial integration of the 2D SAXS pattern (Figure 6.2 (b)) is plotted against q. Peak ratios as well as the 10-to-1 intensity ratio of the first and second peak correspond to a bicontinuous $Ia\bar{3}d$ morphology. The red dashed lines indicate the calculated peak positions of a gyroid structure. The reflections can be indexed according to table 6.1. The two isotropic Debye-Scherrer-rings observable in the 2D scattering image imply a lack of long-range order.

Table 6.1.: Comparison of Experimentally observed scattering peak ratios for a 44.3 wt% solution of polystyrene-*block*-poly(4-vinylpyridine) in THF at 25 °C to theoretically calculated peak ratios of a gyroid microstructure.

$n^{1/2}$	q [nm^{-1}]	q/q*	q/q*	(hkl)
	exp.	exp.	theo.	
3	0.181	1.00	1.00	(211)
4	0.209	1.16	1.15	(220)
7	0.276	1.53	1.53	(321)
8			1.63	(400)
10			1.83	(420)
11			1.73	(332)
12			2.00	(422)
13			2.08	(431)
15			2.24	(521)
16	0.406	2.24	2.31	(440)
19	0.454	2.51	2.52	(611)
20	0.470	2.60	2.58	(620)
21	0.478	2.64	2.65	(541)
23			2.77	(631)
24			2.83	(444)
25			2.89	(543)

6.3.2. Electric Field-Induced Gyroid-to-Cylinder Phase Transition

The electrostatic penalty associated with dielectric interfaces not aligned parallel to the electric field vector cannot be reduced by realignment of the structure in cubic phases. Instead structural distortions and subsequently phase transitions occur upon inception of sufficiently large electric fields. Although the electric field-induced gyroid-to-cylinder transition in block copolymer solutions has been reported by Schmidt et al. in 2010 the mechanisms of the transition could not be unveiled to date [SPS*10].

Various possible mechanistic pathways have been reported. Matsen described a low energy pathway between the local minima of the cylinder and gyroid mesophases [Mat98]. According to Matsen the primary step of the temperature-induced gyroid-to-cylinder transition is the formation of a 5-fold junction from a 3-fold junction which breaks and forms a cylindrical unit within the gyroid mesophase. This cylindrical unit connects two distant 4-fold junctions which likewise transform into 5-fold junctions and subsequently

rupture, increasing the length of the cylinder. The gyroid to-cylinder transition proceeds upon repetition of this process. Pinna et al. investigated the electric field-induced gyroid-to-cylinder transition via cell dynamic system simulations [PZ08]. They proposed that the electric field first leads to a stretching of the gyroid structure. Subsequently, the gyroid connections in direction of the electric field vector rupture, leaving behind helical wound cylinders which straighten over time. A further possibly involves a metastable intermediate structure. The hexagonally perforated lamellae (HPL) phase is a common transient structure in the gyroid-to-lamellae transition and has also been observed in the cylinder-to-gyroid transition upon experiments involving shear alignment [ISK*05]. Nonetheless, the HPL microphase has not been observed during the reverse transition from gyroid-to-cylinder.

This section focuses on unveiling the mechanistic pathways behind the electric field-induced gyroid-to-cylinder transition. In Figure 6.9 of the appendix the radial integration of the 2D SAXS patterns shows the structural evolution upon inception of an electric field of 3 kV/mm, 4 kV/mm and 5 kV/mm at temperatures of 25 °C, 28 °C, 32 °C, 36 °C.

For clarification of the mechanistic pathway first Figure 6.3 is discussed in detail and later on compared to the results at different electric field strengths and temperatures. In Figure 6.3 the intensity vs. q plots at various times during the transition are displayed for a PS-*b*-P2VP solution of concentration G1 exposed to an electric field of 3 kV/mm (Figure 6.3 (a)) and 5 kV/mm (Figure 6.3 (b)) at 25 °C. The electric field is applied directly after the 0 s measurement. The calculated peak positions of the G/Ia$\bar{3}$d phase are displayed by the red dashed lines in the image.

Upon inception of electric field peak broadening is observed. The T_{ODT} of this sample amounts 42.5 °C. The electric field shifts the block copolymer phase diagram, favoring the disordered state over phase separation. Considering the results of chapter 4 of this thesis, a T_{ODT} shift of around 4.5 K would be expected for a lamellae forming PS-b-P2VP block copolymer of comparable molecular weight when exposed to an electric field of 5 kV/mm. For cubic microstructures the T_{ODT} shift is anticipated to be even more pronounced due to the increased amount of dielectric interfaces which cannot be aligned parallel to the electric field [KKKB15, SPR*13]. Therefore, the peak broadening can be attributed to softening of dielectric interfaces by reduction of the T_{ODT} induced by the electric field.

After 0.2 s (Figure 6.3 (a)), and 0.33 s (Figure 6.3 (b)), two additional peaks appear in the intensity vs q plots (see black arrows). The formation of a metastable HPL intermediate can be excluded at this point due to the fact that the observed peak positions do not match the calculated ones as indicated by the three green doted lines. Peak and intensity ratios of the newly formed reflections again correspond to the G/Ia$\bar{3}$d phase

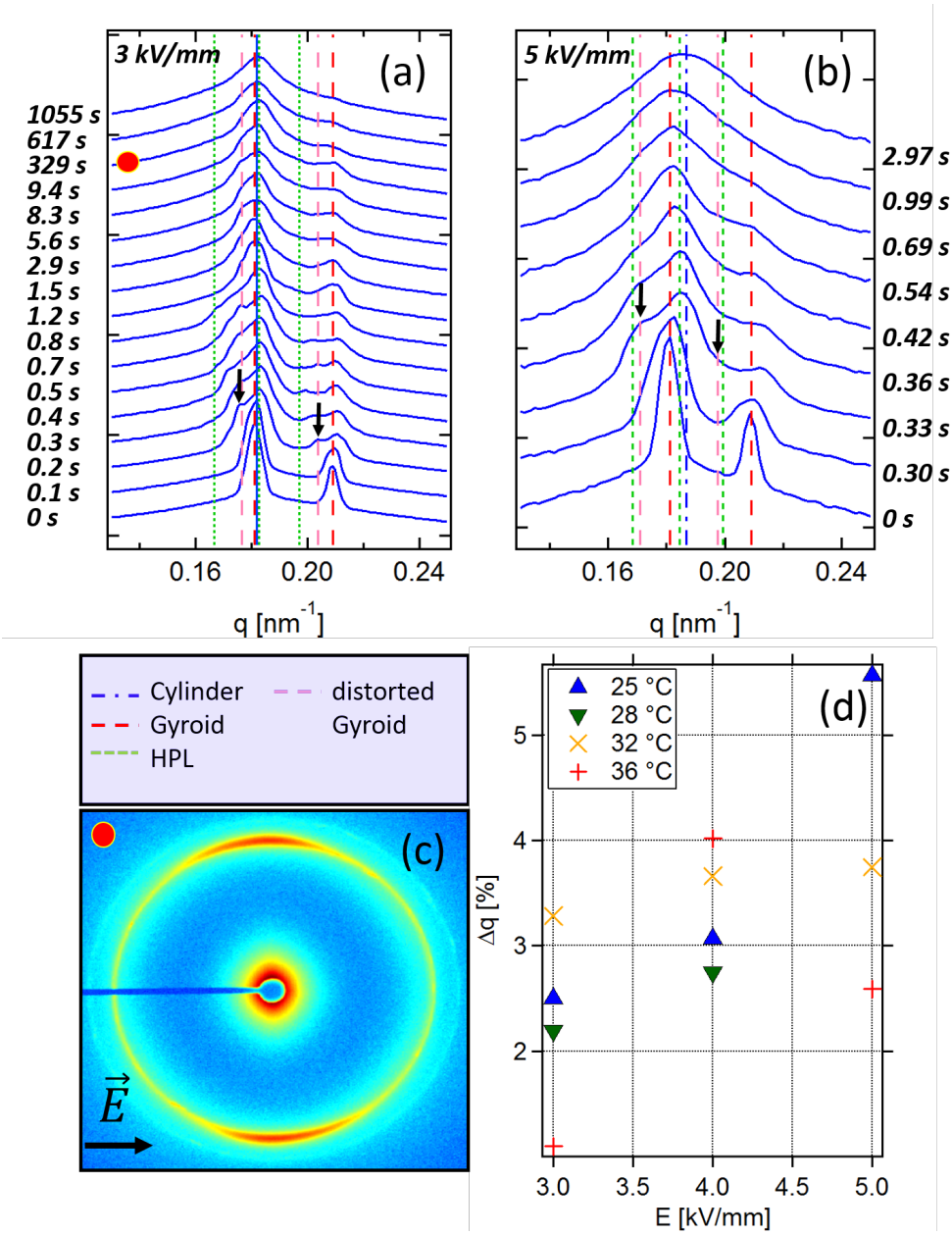

Figure 6.3.: Intensity vs q plots at different times during the electric field-induced gyroid-to-cylinder transition at 25 °C for an electric field of (a) 3 kV/mm and (b) 5 kV/mm. (c) Corresponding 2 D scattering image to the intensity vs q plot at 329 s of (a) as marked by the red dot. The scattering image shows the structural distortion. (d) Degree of distortion as a function of electric field strength.

(pink dashed lines). This implies that the peaks do not result from an intermediate struc-

ture but rather arise from anisotropy caused by the stretching of the gyroid resulting in different lattice parameters parallel and perpendicular to the electric field vector and therefore two different q_{max}. These findings are in accordance with the results of the cell dynamic system simulations by Pinna et al. described above [PZ08]. The assumption of structural anisotropy parallel and perpendicular to **E** is supported when analyzing the 2D scattering image in Figure 6.3 (c). The image corresponds to the intensity vs q plot at 329 s (Figure 6.3 (a)) as indicated by the red dot. The direction of the electric field is depicted in the bottom left of the image. Scattering from structures parallel to the electric field vector results in a single high intensity peak which can be attributed to the cylinder phase while for structures perpendicular to **E** the two reflections of the gyroid morphology are still present. This also corresponds to the findings of Pinna et al. who stated that cylinders begin forming in direction of the electric field vector [PZ08].

In Figure 6.3 (d) the degree of anisotropy (Δq) of the gyroid morphology is plotted against the electric field strength at temperatures of 25 °C, 28 °C, 32 °C, 36 °C. Δq was calculated according to equation 6.1 whereby q_{max}(Gyroid) is the q-value of the first peak of the original gyroid, and q_{max}(distorted Gyroid) describes the q position of the first peak of the additionally upcoming gyroid reflections.

$$\Delta q = \frac{q_{max}(\text{Gyroid}) - q_{max}(\text{distorted Gyroid})}{q_{max}(\text{Gyroid})} \times 100 \tag{6.1}$$

In general the degree of anisotropy rises with increasing electric field strength. The only exception is at 36 °C where a decrease in Δq is observed from 4 kV/mm to 5 kV/mm. This can be explained upon evaluation of the 2D SAXS patterns in Figure 6.10 which display the scattering from the final cylinder structure. At 36 °C an electric field of 5 kV/mm induces an order-disorder transition instead of an order-order transition. 0.09 s after inception of the electric field structural anisotropy is observed which is shortly afterwards followed by complete disordering of the structure. Furthermore, the dielectric interfaces between the block copolymer constituents are not as sharp in the weak segregation limit (WSL), the A and B monomer concentrations vary smoothly over the entire period of the microstructure which also affects the degree of distortion provoked by the electric field. This can likewise be seen upon analysis of the 2 D SAXS images shown in Figure 6.10. In general the degree of orientation is expected to correlate with the electric field strength. Opposed to this, in some cases e.g. at 25 °C the best degree of ordering seems to be present at 3 kV/mm. This observation can be attributed to the increased softening of interfaces and hence peak broadening at higher field strengths.

Although the phase transition mechanism seems to be similar in all analyzed cases the newly appearing gyroid peaks are not as strongly pronounced at 32 °C and 36 °C

when electric fields of 4 kV/mm and 5 kV/mm are applied as can be seen in Figure 6.9. Reason for this is the severe peak broadening initiated by the reduction of the T_{ODT} upon inception of electric field which complicates the differentiation of the peaks. Summarizing the electric field has influence on the degree of phase separation and the magnitude of drawing of the cylinder phase.

6.3.3. Mechanisms of the Cylinder-to-Gyroid Transition

As will be shown in the following sections, a reformation of the gyroid phase is observed after the electric field is turned off, hence the electric field-induced gyroid-to-cylinder transition is reversible. Questionable is whether the electric field enhanced ordering of the cylinder phase has influence on the orientation of the reformed gyroid. One of the objectives of this work was to identify the conditions leading to an increase in long-range order of the gyroid morphology upon application of electric field. In our study three different mechanisms were found resulting in different degrees of gyroid ordering which will be described in detail upon evaluation of three typical examples:

Pathway A - Hexagonal Perforated Lamellae Intermediate.

Pathway B - Nucleation and Growth from the Cylinder Phase.

Pathway C - Intermediate formation of Connections.

After a detailed description of these three example transitions the effect of temperature and electric field will be evaluated with respect to the exploited mechanism and the degree of ordering of the final G/Ia$\overline{3}$d phase.

6.3.3.1. A - Hexagonal Perforated Lamellae Intermediate

In this section pathway A will be discussed. In Figure 6.4 (a) the intensity vs q plots at various times during the reformation of the gyroid phase after turning of an electric field of 3 kV/mm at 25 °C in a solution of G2 are displayed. Starting point is a cylinder phase with a preferred orientation of the cylinder axis parallel to **E** which can be concluded from the corresponding 2 D SAXS image (Figure 6.4 (d)). A higher scattering intensity is observed perpendicular to **E** implying that the majority of cylinders are aligned in direction of the electric field vector. The electric field (3 kV/mm) is turned off directly after the 0 s measurement which is accompanied by a slight shift in the q_{max} value of the cylinders. After an induction period two additional peaks start appearing at around 42 s which subsequently grow. The corresponding scattering image at 1061 s where the additional peaks are most pronounced is given in Figure 6.4 (c). A metastable intermediate structure is formed which vanishes after 5253 s giving rise to the gyroid morphology.

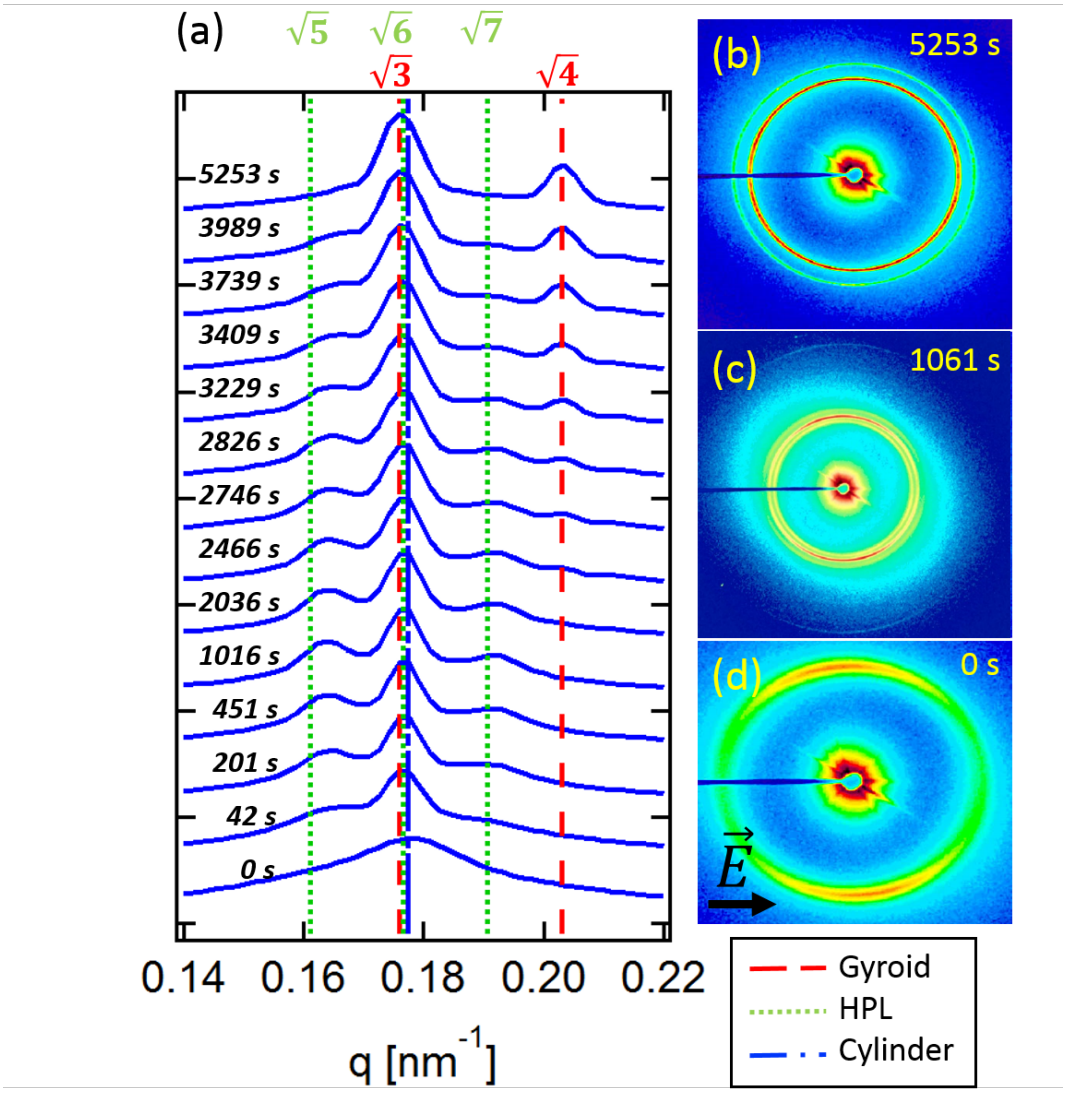

Figure 6.4.: (a) Intensity vs q plots at various times during the cylinder-to-gyroid transition after turning off the electric field. (c-d) Corresponding 2 D SAXS images at (b) 5253 s, (c) 1061 s, and (d) 0 s. An HPL is observed as metastable intermediate structure.

We now focus our discussion on the identification of the metastable intermediate. In Figure 6.5 (a) the scattering intensity in atomic units - obtained via radial integration of the 2D SAXS image displayed in Figure 6.5 (b) - is plotted against the scattering vector q. The peaks can unambiguously be attributed to the hexagonal perforated lamellae (HPL) morphology. The green dashed lines display the theoretical peak positions calculated for the HPL microstructure. The HPL structure can occur in various sequences with respect to the positioning of perforated layers to one another. Amongst others ABAB...

Table 6.2.: Comparison of Experimentally observed scattering peaks for a 46.3 wt% solution of polystyrene-*block*-poly(4-vinylpyridine) in THF at 25 °C. The metastable intermediate structure was observed during the cylinder-to-gyroid transition after turning of an electric field of a strength of 3 kV/mm.

$n^{1/2}$	q [nm^{-1}]	q/q*	ABCABC... stacking	$(hkl)^{ABC}$	ABAB... stacking	$(hkl)^{AB}$
5	0.163	1.00	1.00	(101)	1.00	(100)
6	0.177	1.08	1.09	(003)	1.09	(002)
					1.14	(101)
7	0.191	1.17	1.18	(102)		
13			1.61	(110)		
15	0.281	1.72	1.73	(104)	1.73	(110)
			1.90	(201)		
					1.92	(103)
19			1.95	(113)		
20			2.00	(202)	2.00	(200)
21			2.05	(105)	2.05	(112)
21.4					2.07	(201)
24	0.353	2.16	2.18	(006)	2.18	(004)

(hexagonal, space group P6$_3$/*mmc*), ABCABC... (trigonal, space group R$\bar{3}m$), and combinations of both have been reported [QW97, FKZ*94, HC04, SKB*96, ZHC*03]. Self-consistent field theory (SCFT) calculations by Matsen attributed higher thermodynamic stability to the ABCABC... stacking compared to the ABAB... stacking [Mat09]. In coherence with Masten's results the observed peak ratios correspond to an ABCABC... stacking as can be extracted from Table 6.2 which compares the experimental peak ratios to those expected for HPL morphologies with ABAB... and ABCABC... stacking. The lattice parameters can be obtained by solving Equation 6.2 which yields $a = 47.2$ nm and $c = 106.5$ nm.

$$\frac{1}{{d_{hkl}}^2} = \frac{4}{3}\left(\frac{h^2 + hk + k^2}{a^2}\right) + \frac{l^2}{c^2} \tag{6.2}$$

Reflections $\sqrt{6}, \sqrt{24}, \sqrt{54}$ result from the lamellae stacks of the HPL which have a periodicity of 35.5 nm ($\frac{c}{3} = \frac{d_{003}(HPL)}{3} = \frac{2\pi}{q_{003}}$). The other peaks ($l \neq 0$) can be attributed to the hexagonally packed cylinders penetrating the lamellae layers with a cylinder to

cylinder distance of $a = 47.2$ nm. A schematic image of the HPL structure with its lattice parameters a and c can be found in Figure 6.5 (c).

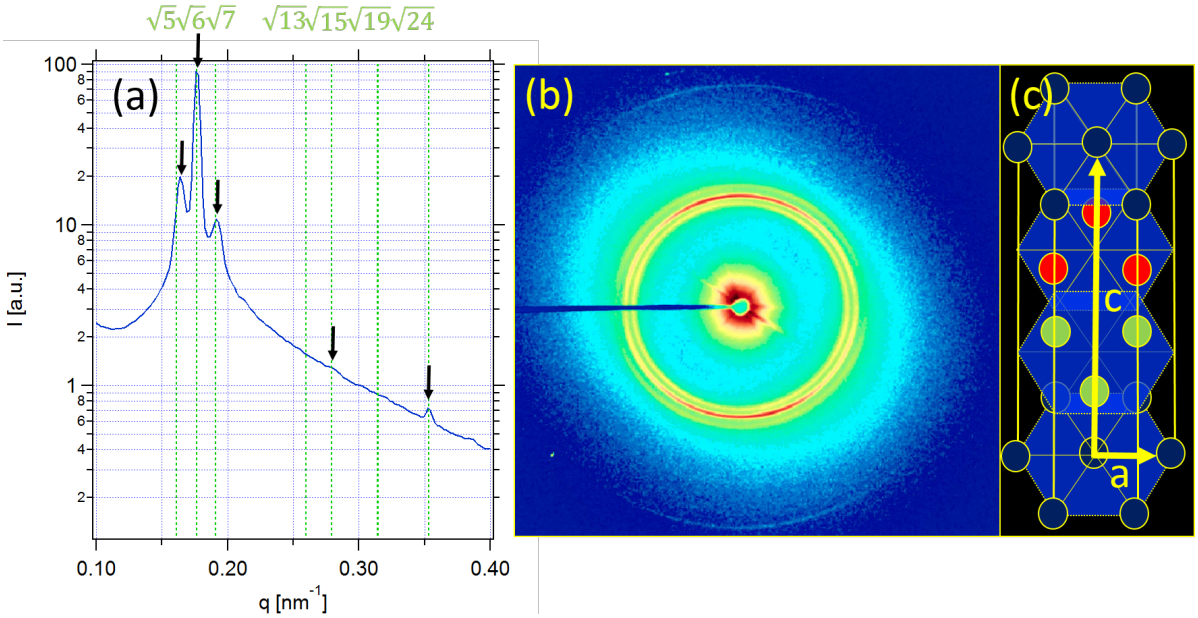

Figure 6.5.: (a) Intensity vs. q plot obtained via radial integration of the scattering image of the HPL microstructure (b). (c) Schematic representation of the HPL microstructure with lattice parameters a and c.

Figure 6.4 (c) and (b) clearly show that while the lamellae stacks of the HPL show a preferred direction parallel to the electric field vector, scattering from the reformed gyroid results in two isotropic Debye Scherrer rings implying a lack of long range order. Hence, the cylinder-to-gyroid transition involving an HPL intermediate does not lead to a preferred orientation of the G/Ia$\bar{3}$d phase.

Förster et al. [FKZ*94] analyzed the complex phase behavior of polystyrene-*block*-polyisoprene diblock copolymers in vicinity of the order-disorder transition. An epitaxial transition from a shear aligned HPL phase with ABCABC... stacking to the G/Ia$\bar{3}$d phase was reported. This epitaxial relationship resulted in a higher ordered gyroid. A 10 spot scattering pattern was observed for the G/Ia$\bar{3}$d phase. Indexation implied that the [111] direction of the G/Ia$\bar{3}$d phase coincided with shear direction. Nonetheless, the structure is not composed of a single crystal but of a 2D powder consisting of domains rotated randomly around the [111] lattice direction.

Opposed to this Schulz et al. [SKB*96] observed the formation of a nearly isotropic scattering pattern when analyzing the shear aligned HPL to gyroid transition in polystyrene-*block*-poly(2-vinylpyridine). They concluded that the gyroid phase grows without pre-

ferred orientation from the HPL phase. It was speculated whether a difference in HPL stacking sequence leads to the observed differences. Our observations are consistent with the results from Schulz et al. While the electric field-induced orientation was preserved during the cylinder to HPL transition the subsequently formed gyroid phase lacks long-range order implying a non-epitaxial transition.

6.3.3.2. B - Nucleation and Growth from the Cylinder Phase

In the following we will elucidate pathway B. In Figure 6.6 the scattering curves at various times during the transition after turning of an electric field of 5 kV/mm at 32 °C in a solution of G1 are displayed. Turning off the electric field is accompanied by a slight shift in q_{max} to smaller values and a sharpening of the cylinder peak. After an induction period of around 129 s the second gyroid peak starts appearing which subsequently grows over time. At 229 s the first gyroid peak approaches as a sharp peak from the broader cylinder peak. The coexistence of the two phases and the lack of further reflections implies that the G/Ia$\overline{3}$d phase forms directly from the cylinder phase through a nucleation and growth process without any transient morphology. The scattering image in Figure 6.6 (e) and the similar q_{max} values of the cylinder and gyroid structure indicated by the red and blue dashed line in Figure 6.6 (a) imply an epitaxial relationship between the two morphologies whereby the G/Ia$\overline{3}$d phase forms with a preferential direction from the cylinder phase. A 10-spot scattering pattern (Figure 6.6 (e)) is obtained which can be indexed - under consideration of the setup (Figure 6.1) - according to Förster et al. [FKZ*94]. In Figure 6.6 (d) the reflections are assigned to the corresponding lattice planes. The high intensity spots are expected to form angles of 19.47 °, 61.87 °, and 90 ° with the [111] direction. This implies a cubic phase with orientational order around the [111] direction which coincides with the direction of the electric field vector. Since the 10 reflections cannot be coplanar, the 10 spot scattering pattern suggests a lack of rotational order meaning that the sample is composed of individual grains rotated randomly around the [111] direction [FKZ*94].

The thin ring underneath the high intensity spots of the G/Ia$\overline{3}$d phase can most probably be attributed to residual cylinders. The anisotropic intensity distribution which is characterized by a higher scattering intensity perpendicular to **E** than parallel to **E** is caused through the preferred alignment of cylinders with their axis parallel to **E**. Hence, the transition was not fully completed at the end of the measurement.

Vilgid et al. [VAM*98] likewise observed an epitaxial hexagonal-to-gyroid transition without any transient structures when the transition was induced by a shallow temperature quench from the cylinder phase.

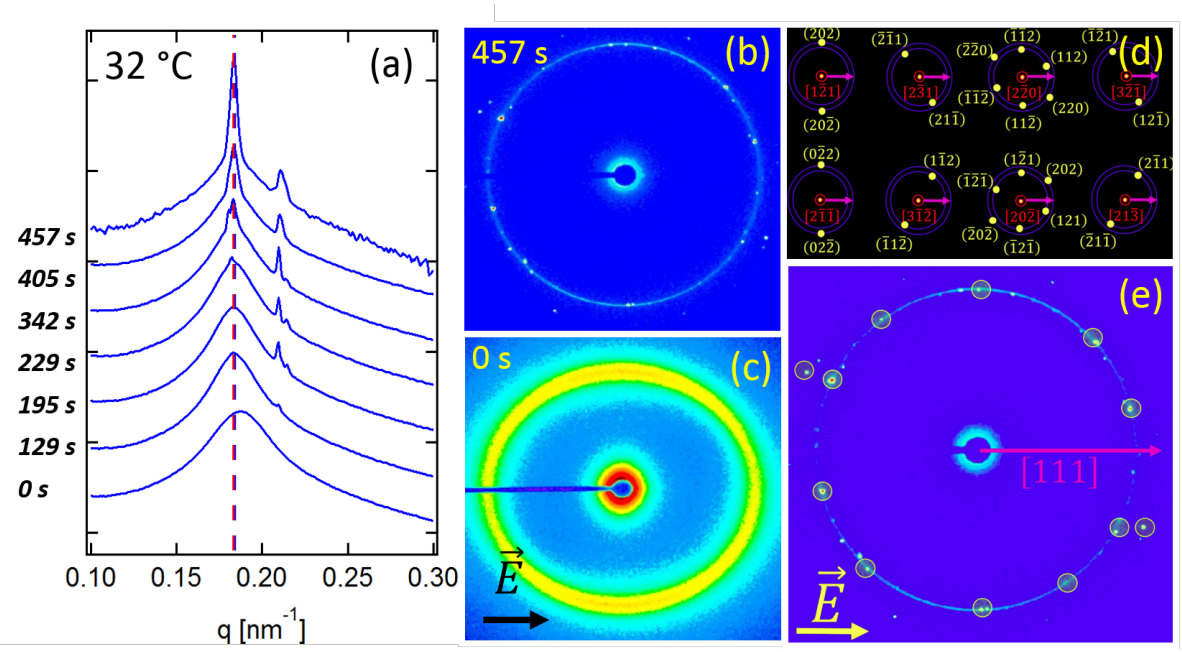

Figure 6.6.: (a) Intensity vs q plots at various times during the cylinder-to-gyroid transition after turning off the electric field. (b-c) Corresponding 2D SAXS scattering images at (b) 457 s and (c) 0 s. (d) Assignment of lattice planes to the high intensity spots. (e) Scattering image with the assignable spots marked by yellow circles.

6.3.3.3. C - Additional Junctions within the G/Ia$\bar{3}$d phase

The last mechanism observed is pathway C which will be described by analyzing the transition after turning of an electric field of 4 kV/mm at 25 °C in a solution of G1. This typical example of mechanism C is displayed in Figure 6.7. Upon application of an electric field domain fluctuations are increased and the order-disorder transition temperature is shifted to lower values. This results in significant broadening of the first order Bragg peak as long as the electric field is applied to the sample. Therefore, turning off the electric field initially leads to a sharpening of the cylinder peak. After 101 s the second gyroid peak starts appearing which is accompanied by two further peaks after 511 s marked by the black arrows in image 6.7 (a). According to the calculated peak positions the reflections can neither be attributed to an intermediate HPL structure (green dotted line) nor to distortions of the gyroid as observed for the opposite transition (pink dashed line). In this case the peaks cannot clearly be assigned. Figure 6.7 (c) displays the scattering pattern corresponding to the scattering curve at 721 s. The yellow arrows mark the additional Bragg reflections. Opposed to the transition involving an intermediate HPL morphology the additional peaks start appearing after the formation of the two

typical gyroid peaks has set in. Therefore, we conclude, that the upcoming reflections are caused by additional connections which are formed in the course of the cylinder-to-gyroid transition which subsequently rupture. A possible scenario was described by Matsen [Mat98]. According to his calculations the gyroid-to-cylinder transition proceeds via a low-energy epitaxial nucleation and growth pathway. He proposed that the transition is initiated by the formation of a fivefold junction that pinches off, breaks a cylinder and leaves behind a threefold junction. The two residual free ends of the cylinder are energetically unfavorable and form two fourfold junctions which break into threefold junctions. These junction points would lead to additional scattering peaks. However, since the corresponding peak ratios for this intermediate morphology have not been calculated we can only speculate about the exact mechanism at this point.

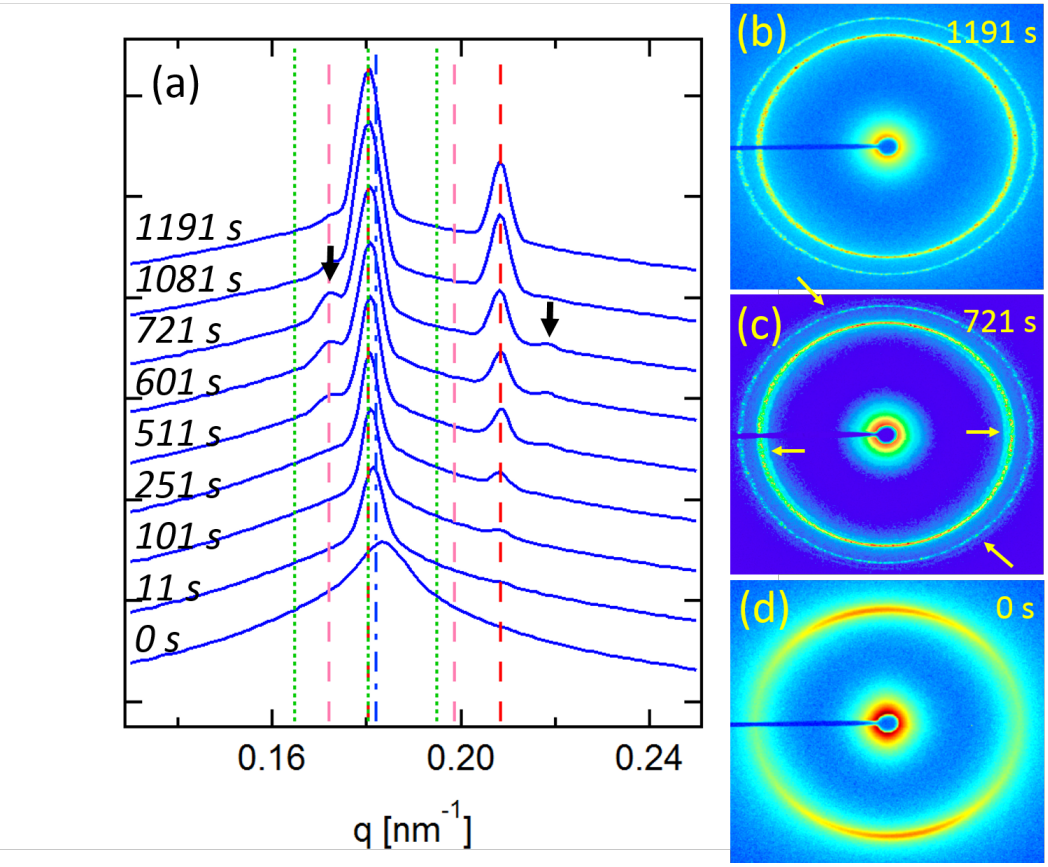

Figure 6.7.: (a) Intensity vs q plots at various times during the cylinder-to-gyroid transition. (b-d) 2D SAXS scattering images at (b) 1191 s, (c) 721 s, and (d) 0 s.

6.3.3.4. The Influence of Temperature and Electric field strength on the Mechanism and Ordering

Summarizing three different mechanisms were observed for the reformation of the G/Ia$\bar{3}$d phase from the cylindrical phase. In this section we will elucidate under which temperature and electric field conditions the individual mechanisms are exploited and compare the degree of ordering achieved.

In Figure 6.11 of the appendix the transition mechanisms are displayed for all analyzed field strengths, concentrations and temperatures. To clearly represent the effect of the individual parameters the results were summarized in Figure 6.8 (a) for concentration G1 and (b) for concentration G2. The plot assigns the pathways A, B and C to the corresponding field strength and temperature. The black X marks conditions under which no measurement was performed.

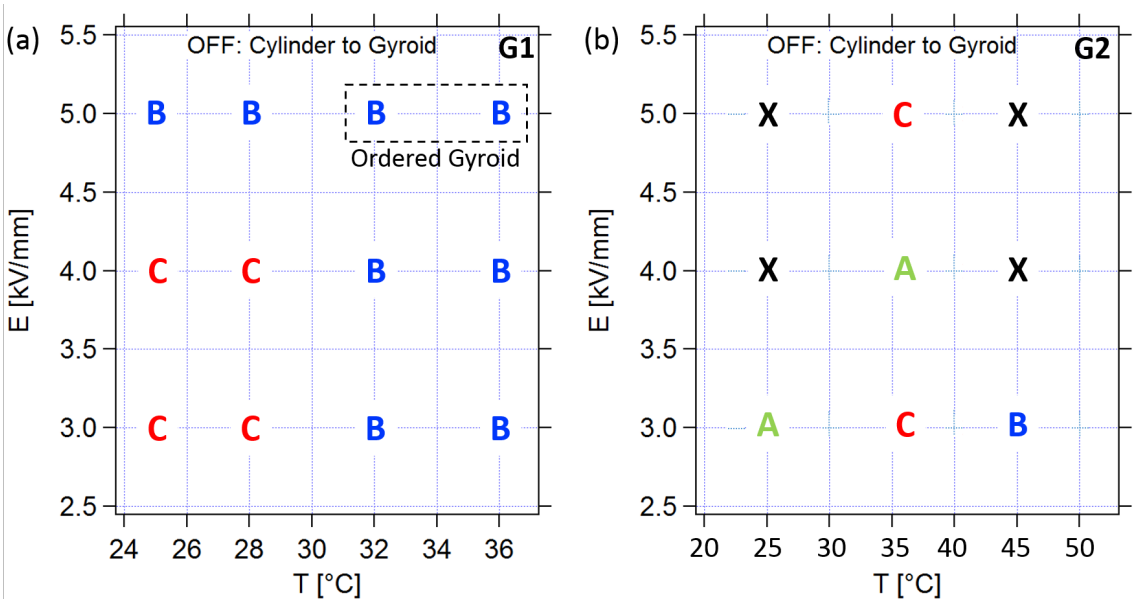

Figure 6.8.: Diagram assigning pathways A, B, and C to the corresponding temperature and electric field strength for solutions of G1 (a) and G2 (b). The black X marks conditions under which no measurements were performed.

Interestingly, the transition pathway seems to be influenced by the electric field strength although the electric field is no longer present during the transition. As discussed above the electric field has two major effects on the block copolymer phase diagram: the T_{ODT} is shifted to lower values and uniaxial phases are preferred over cubic phases, shifting the coexistence line. Hence, turning on and off the electric field can be regarded as a jump between two different phase diagrams. The Nucleation and Growth

mechanism without transient structures is clearly the favorable pathway at high field strengths and temperatures while lower field strengths and temperatures seemingly promote the formation of intermediate structures (pathways A and C). Pathway A involving the HPL intermediate is merely observed in the higher concentrated solution G2 which is further away from the order-disorder concentration (ODC). The ODC describes the polymer concentration at which the solution is disordered at room temperature. Increasing the polymer concentration has a similar effect as lowering the solution temperature. Therefore, it can be concluded that the HPL intermediate morphology only appears at higher concentrations and hence lower temperatures.

Viglid et al. [VAM*98] analyzed the temperature induced gyroid-to-cylinder transition in a poly(ethylene-*alt*-propylene)-poly(dimethylsiloxane) diblock copolymer and found an intermediate free nucleation and growth mechanism when induced by a shallow quench while deeper quenches gave rise to a metastable HPL. They concluded that the HPL intermediate is formed when the energy barrier for the cylinder-to-HPL transition is smaller than for the cylinder-to-gyroid transition which is the case at lower temperatures. The layer-like HPL is described to reduce the interfacial tension while the chain packing frustration associated with the intermediate is relieved by subsequent formation of the G/Ia$\overline{3}$d phase. Also the change in transition mechanism was speculated to result from exceeding the temperature limit of the HPL structure. This is consistent with our results on the effect of temperature on the transition mechanism: At lower temperatures the transition proceeds via metastable intermediates while a Nucleation and Growth pathway without intermediate structures is observed at higher temperatures. The free energy associated with the individual structures is altered by **E** and T. According to our measurements an increase in field strength has a similar effect on the mechanism as rising the temperature. At this point it has to be mentioned that the temperature of the solution was monitored *in-situ* via a tiny PT100 thermosensor during the entire experiment and no rise in temperature was recorded through application of an electric field. For further details on the sample cell we refer to chapter 3 of this thesis. Hence, it becomes evident that not only the overall temperature during the transition has influence on the mechanism but also the beginning and end states. When we regard the application of an electric field as a sudden jump from one phase diagram to the other and vice versa when the field is turned off, the free energy of the individual phases in the second phase diagram will defer more from those in the original phase diagram at given T and ϕ_A in case of a 5 kV/mm jump than in case of a 3 kV/mm jump. Hence, different stability regions of metastable structures might be crossed upon switching between phase diagrams.

In the last part of this chapter we will now focus on the conditions under which ordering can be achieved. We refer to Figure 6.13 and 6.14 which shows the scattering

images of the gyroids formed after the electric field is turned off. All gyroids formed from solution G2 are characterized by two isotropic Debye Scherrer rings implying a lack of orientational order independent of the transition mechanism. In case of solution G1 the gyroid structure is the more isotropic for lower temperatures and field strengths. For 32 °C and 36 °C higher ordered gyroids were formed when an electric field of 5 kV/mm is turned off (see Figure 6.13). From these observations it can be concluded, that the distance from the order-disorder transition temperature has influence on the degree of ordering rather than the transition mechanism.

6.3.4. Summary

The mechanisms of the electric field-induced gyroid-to-cylinder transition and of the reformation of the G/Ia$\bar{3}$d phase after turning off the electric field were analyzed. The gyroid-to-cylinder transformation proceeds via an initial distortion of the gyroid followed by the formation of cylinders. In case of the opposite transition three different mechanisms were observed: nucleation and growth of the gyroid from cylinders without any intermediate structures, a transition involving the formation of a metastable intermediate HPL structure, and a further metastable intermediate characterized by additional connections within the G/Ia$\bar{3}$d phase. Transitions with metastable intermediates were preferably found at lower temperatures and field strengths. Higher ordered gyroids could only be obtained in close vicinity of the T_{ODT} at the highest electric field strength analyzed (5 kV/mm).

6.4. Appendix

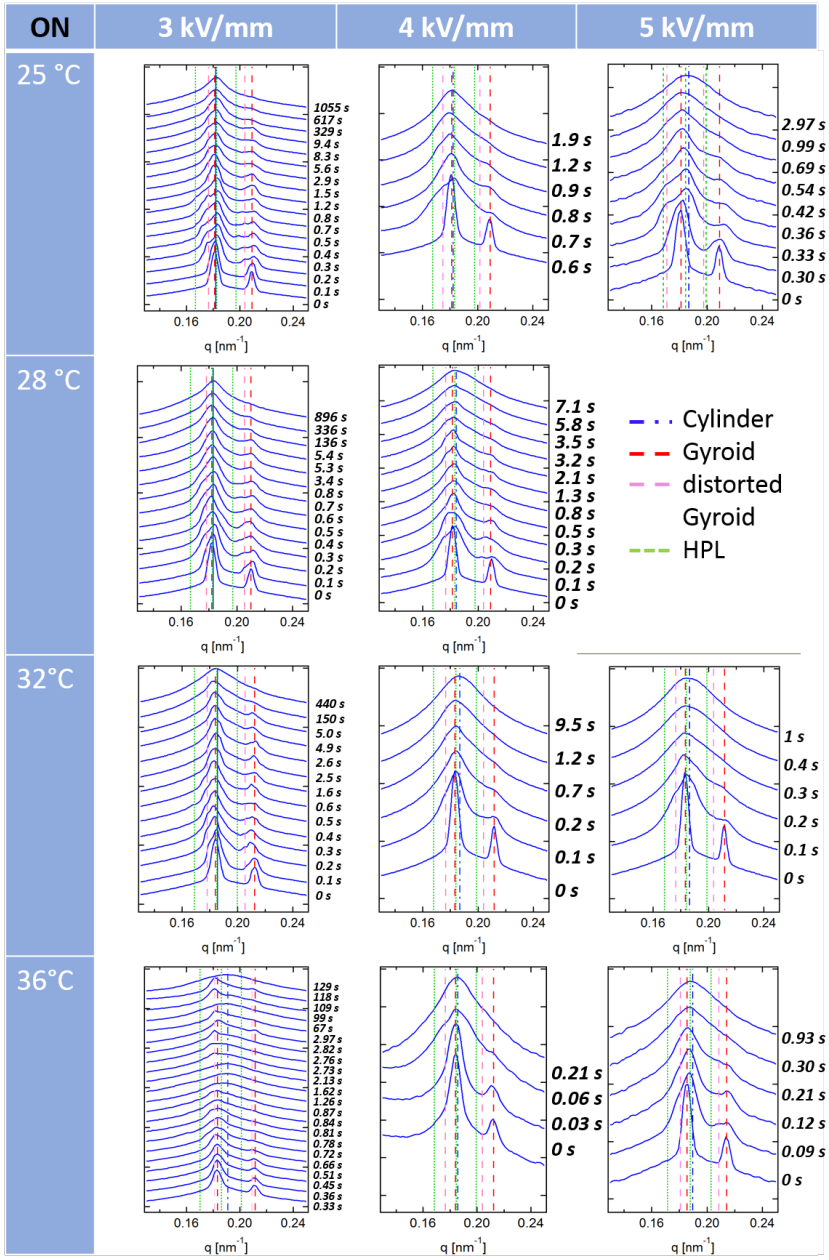

Figure 6.9.: Intensity vs q plots at various times during the electric field-induced gyroid-to-cylinder transition for temperatures of 25 °C, 28 °C, 32 °C, and 36 °C and electric field strengths of 3 kV/mm, 4 kV/mm, and 5 kV/mm.

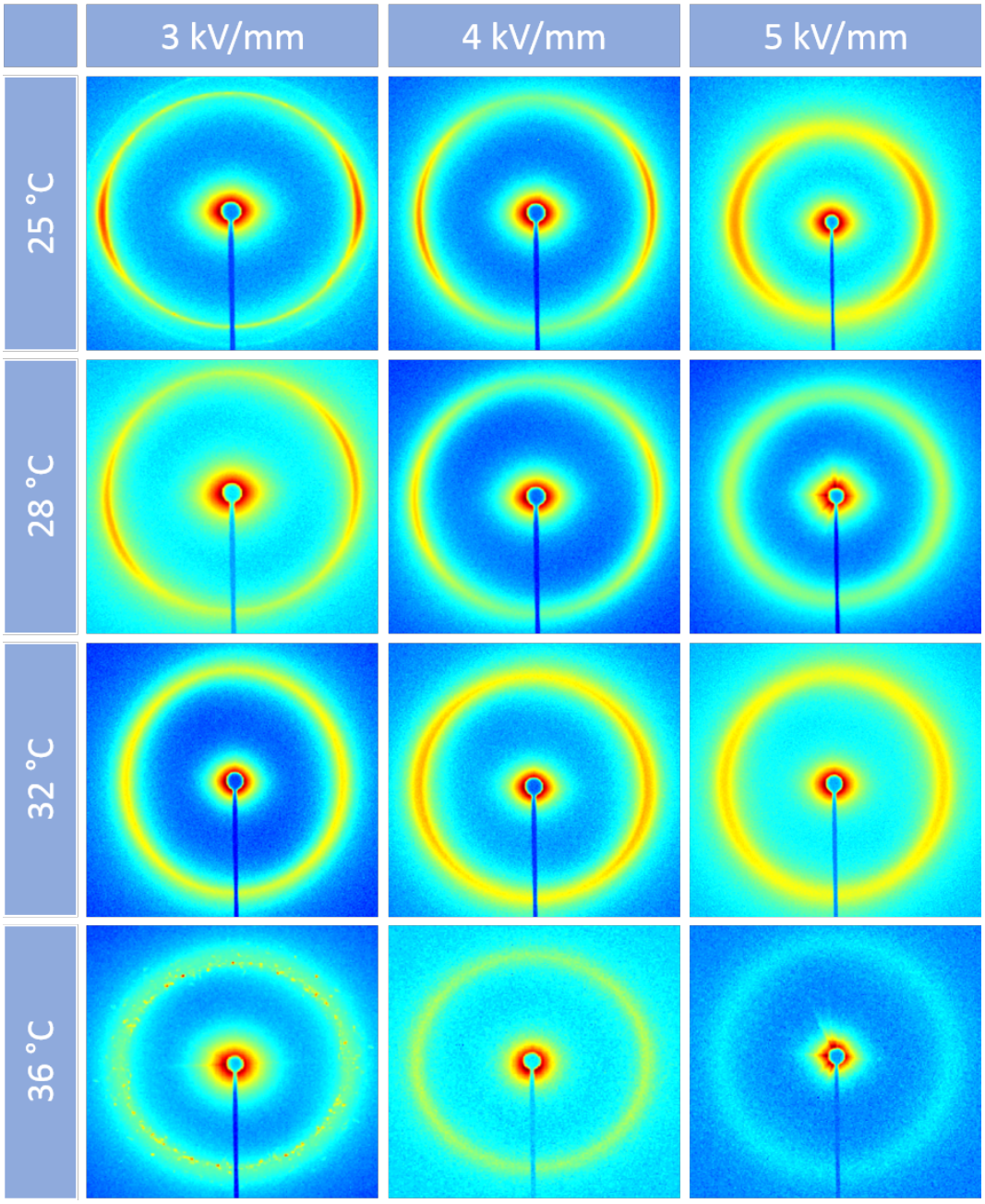

Figure 6.10.: 2D SAXS images of the cylinder phase formed from the gyroid structure by application of electric fields of 3 kV/mm, 4 kV/mm, and 5 kV/mm at temperatures of 25 °C, 28 °C, 32 °C, and 36 °C.

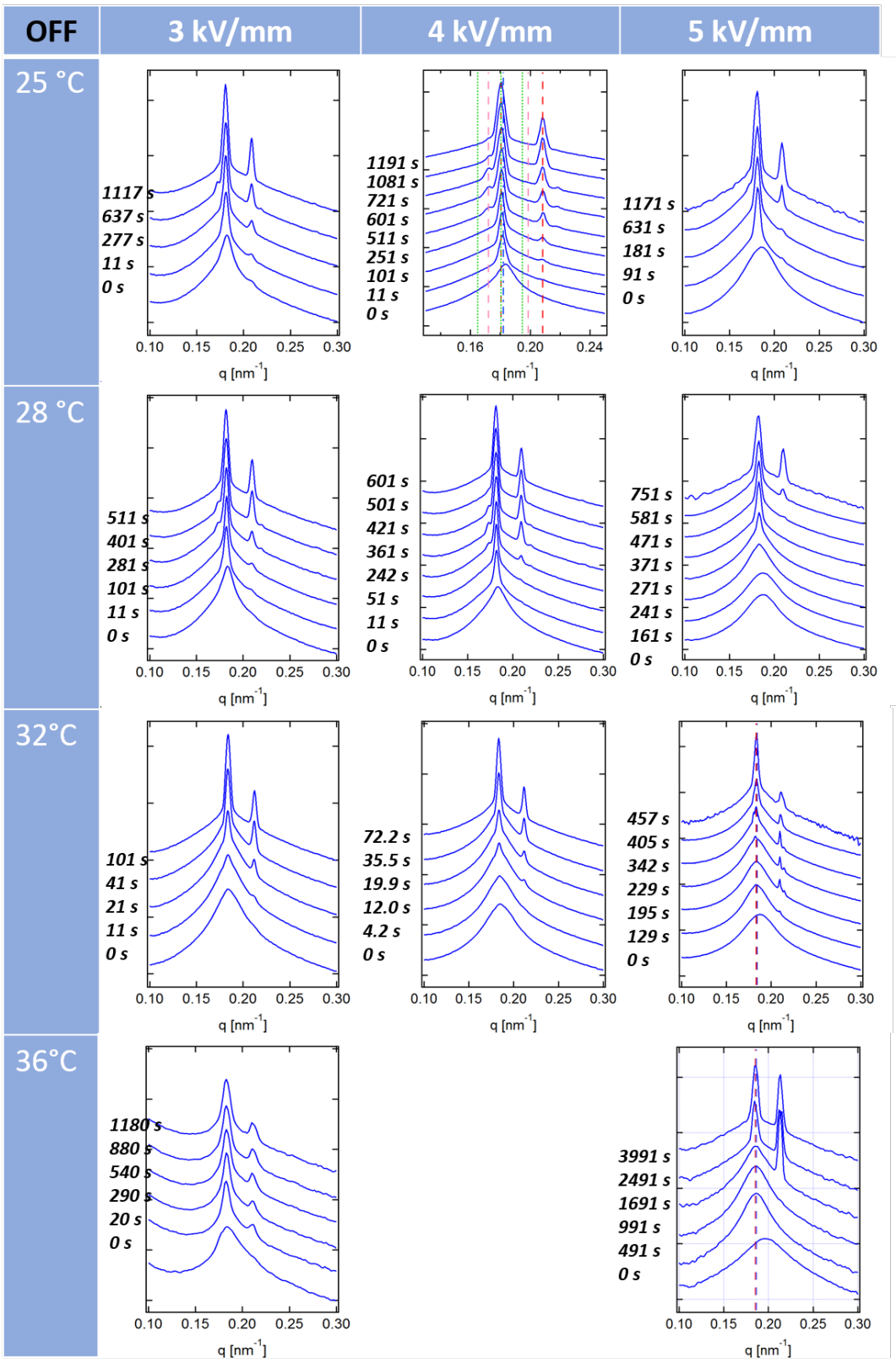

Figure 6.11.: Intensity vs q plots at various times during the cylinder-to-gyroid transition for temperatures of 25 °C, 28 °C, 32 °C, and 36 °C after turning off an electric field of 3 kV/mm, 4 kV/mm, and 5 kV/mm.

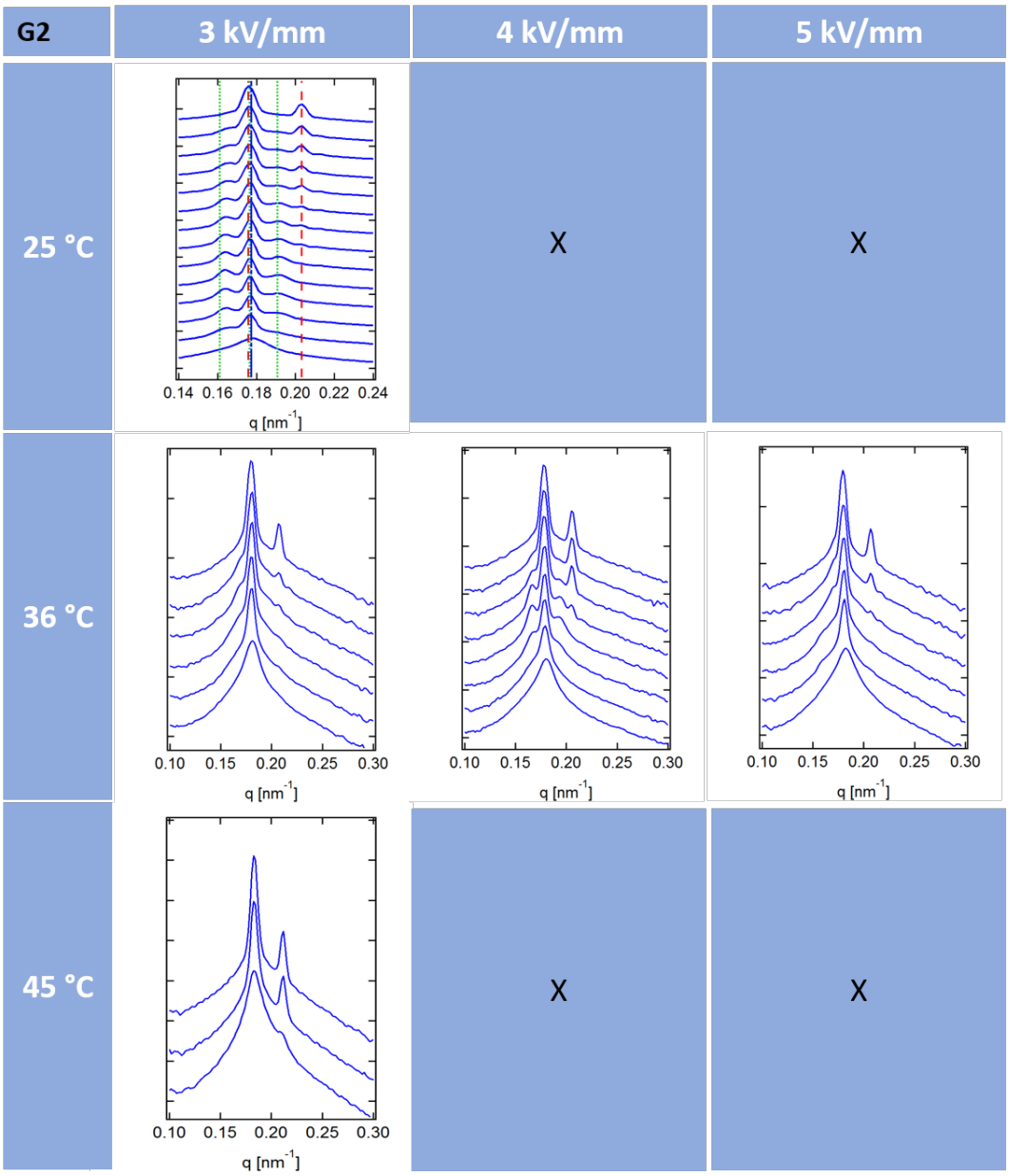

Figure 6.12.: Intensity vs q plots at various times during the cylinder-to-gyroid transition for temperatures of 25 °C, 36 °C, 45 °C after turning off an electric field of 3 kV/mm, 4 kV/mm, and 5 kV/mm.

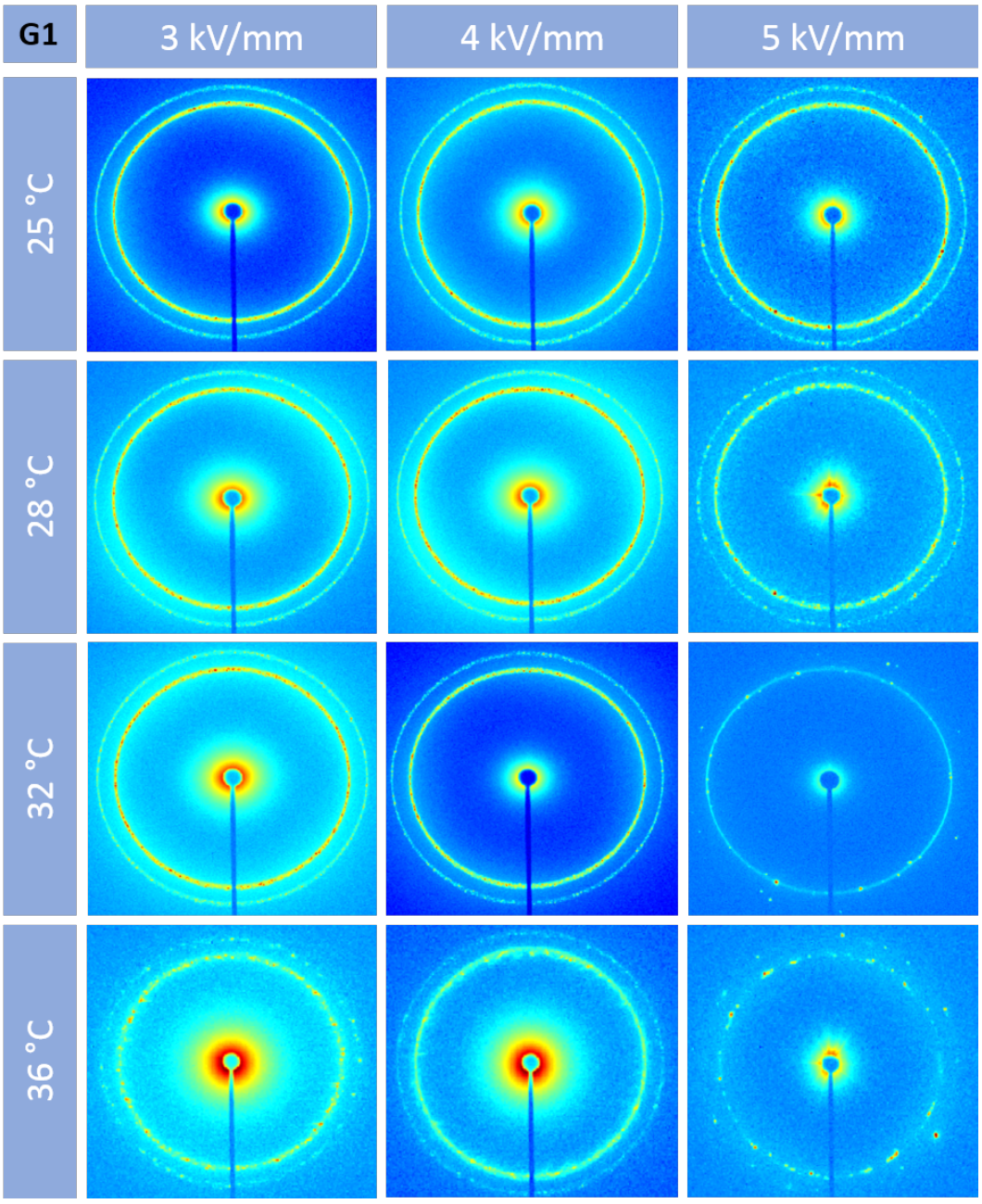

Figure 6.13.: 2D SAXS images of the reformed gyroid phase after turning off an electric field of 3 kV/mm, 4 kV/mm, and 5 kV/mm at temperatures of 25 °C, 28 °C, 32 °C, and 36 °C.

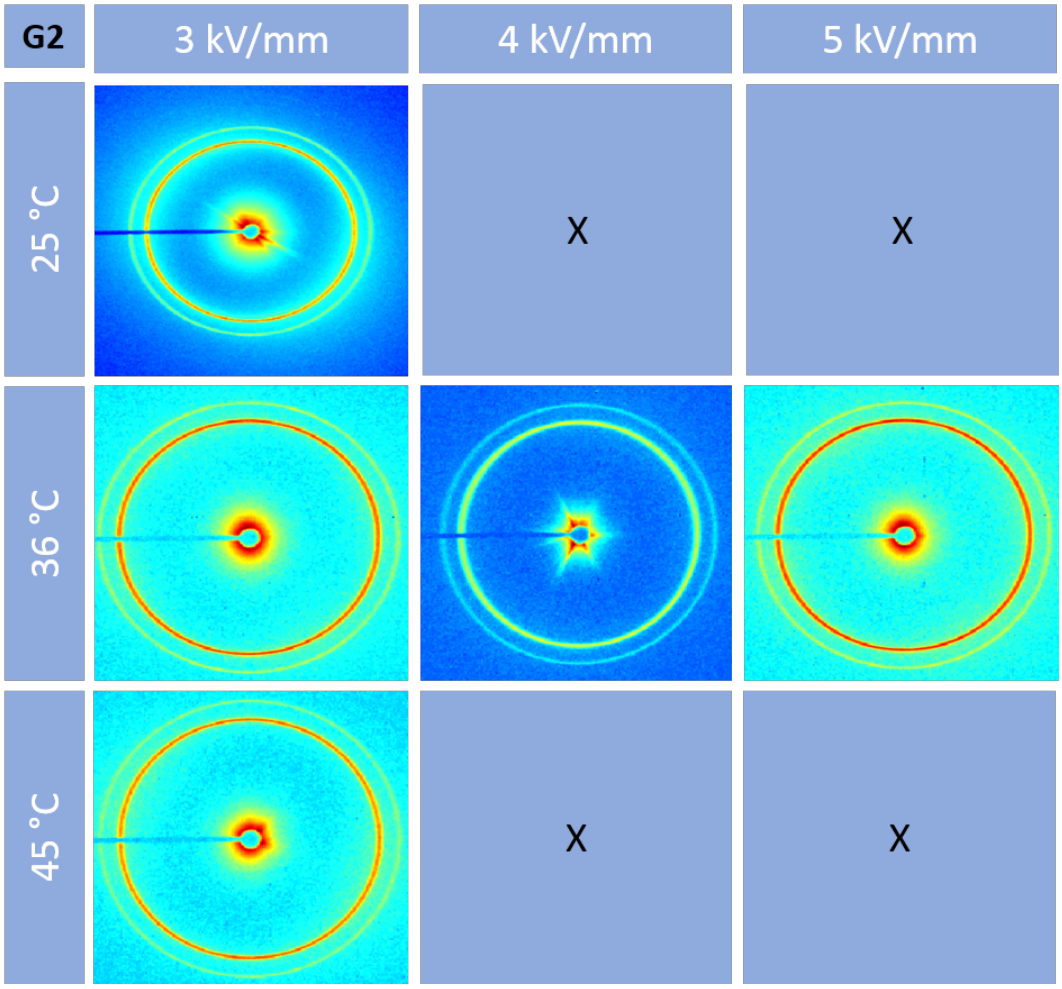

Figure 6.14.: 2D SAXS images of the reformed gyroid phase after turning off an electric field of 3 kV/mm, 4 kV/mm, and 5 kV/mm at temperatures of 25 °C, 36 °C, and 45 °C.

Part II.

Thin Films of Block Copolymers

7. Combining Graphoepitaxy and Electric Fields[1]

7.1. Introduction and Theoretical Background

The next two chapters of this thesis deal with the analysis of block copolymer thin films. Block copolymer thin films are promising materials for nanolithography with applications in microelectronics, information storage, photonic crystals and filtration [CRST06, CMR04, SYK10]. Their capability to self-assemble on the nanometer length scale - well below the resolution of conventional photolithography - renders them a cost-efficient alternative to electron beam lithography with high throughput [JHK*13]. Block copolymers with a large Flory-Huggins interaction parameter χ such as poly(styrene)-*block*-poly(dimethylsiloxane)(PS-*b*-PDMS), poly(styrene)-*block*-poly(ethylene oxide) or poly(2-vinylpyridine)-*block*-poly(dimethylsiloxane) feature several advantages. Owing to the enthalpic incompatibility between the blocks, microdomain sizes well below 10 nm can be obtained [BSM*12]. Furthermore line edge roughness [PG12] and defect density are reduced with increasing χ [BF90, TGH*12]. A downside to the high Flory-Huggins interaction parameter is the reduction of chain interdiffusivity which reduces the kinetics of self-assembly and impedes defect annihilation [LD95]. This can be ameliorated by the use of solvent vapor annealing, or by thermal annealing provided the elevated temperature does not degrade the polymer.

PS-*b*-PDMS, which was utilized in this study, not only has the benefit of a high χ-parameter ($\chi_{PS-PDMS} = 0.27$) [Nos95] but also offers an excellent etch selectivity between its blocks [JR07], a feature especially important for pattern transfer applications [GBA*14, TPO*11]. The PS block can selectively be removed by an oxygen plasma

[1]This Chapter and its figures have been published in modified form. [KBCI*15] Reprinted (adapted) with permission from C. C. Kathrein, W. Bai, J. A. Currivan-Incorvia, G. Liontos, K. Ntetsikas, A. Avgeropoulos, A. Böker, L. Tsarkova, and Caroline A. Ross, Combining Graphoepitaxy and Electric Fields toward Uniaxial Alignment of Solvent-Annealed Polystyrene-*b*-Poly(dimethylsiloxane) Block Copolymers, *Chemistry of Materials*, *27* **2015**, 68906898. Copyright 2015 American Chemical Society.

treatment which at the same time partially oxidizes the PDMS, leaving behind a silica-rich and stable etch mask.

One of the challenges in block copolymer lithography is achieving microdomain patterns with long-range order without expensive substrate prepatterning. Excellent order can be obtained by chemical- [KSS*03, SMK*05, RKD*08] or topographic templates [KSS*03, YJ*10, RKD*08, BYJ*08, SKD*07, KKM*07] which can direct the formation of an oriented, defect-free pattern. These templates are often made by electron beam lithography, but this technique is not suitable for large area patterning. Trenches or chemical prepatterns have instead been made using optical methods such as photolithography, interference lithography [LJR*06, JR09] or by step formation in miscut single crystal substrates [RLM*99, HHG*11].

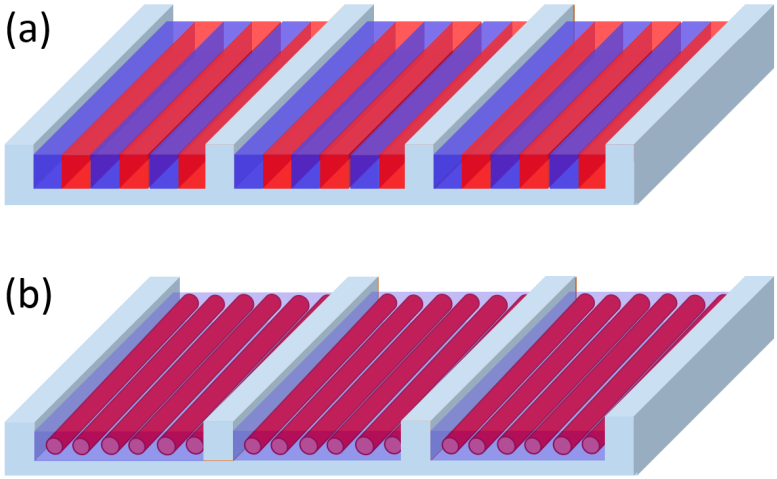

Figure 7.1.: Schematic image of (a) lamella and (b) cylindrical block copolymer nanostructures aligned by graphoepitaxy.

Graphoepitaxy usually provides orientational ordering of microdomains parallel to topographic features such as trench walls as schematically shown in Figure 7.1, and uniaxiality can extend across a trench with a width of tens or hundreds of microdomain spacings [SYK10, CRT*03, CMR04, SDS04b, SDS04a, PSR*07, RRZ*07, BYJ*08]. The correlation length of the pattern depends on the block copolymer composition, molecular weight, substrate chemistry, annealing conditions, and film thickness.

Several other processes produce oriented microdomain patterns [Dar07], including shear of the film [CKS*97, AWA*04], temperature [BBD*07, SGL*14] and swelling gradients [OTB09], flow [SDS04a, SDS04b, JR07], and electric fields [OHK*09, LPR*12, RPL*13, BEH*02a, BKE*02, BEH*03]. These processes lead to alignment however with-

out registration of the positions of microdomains with particular locations on the substrate. Also mass transport due to the polymer flow from a mesa into a trench upon annealing of a block copolymer on topographic substrates has been shown to orient the microdomains along the direction of flow. Such material flow is presumably caused by the inhomogenity of the film thickness upon spin coating on topographic substrates, resulting in a thickness gradient from the trench walls to the middle of the trench. This metastable arrangement however evolves into orientation of microdomains parallel to the trenches upon further annealing [SDS04a, SDS04b].

As described in previous chapters the driving force for the alignment under electric field is the reduced electrostatic energy of the microdomain interfaces oriented parallel to the electric field vector compared to those oriented perpendicular to the electric field vector [SPR*13]. The energy difference between the orientations is proportional to the square of the dielectric contrast $(\Delta\epsilon)^2$ between the blocks of the block copolymer [Tso09] and to the square of the electric field strength E^2. Since the difference in dielectric permittivity between PS and PDMS merely amounts to $\Delta\epsilon = \epsilon_{PS} - \epsilon_{PDMS} \approx 0.17$ [KKKB15] pure electric field-induced alignment is not expected to provide a strong driving force promoting a defect free ordering of microdomains.

A combination of graphoepitaxy for pattern registration and electric field-induced alignment to enhance the correlation length of the resulting microdomains is envisaged as a promising approach towards the directed self-assembly of block copolymers. Furthermore, this approach enables insights into the interaction between different driving forces which affect the alignment. Tong et al. [TS14] utilized electric fields to switch the orientation of a cylinder forming polystyrene-*block*-poly(ethylene-*alt*-propylene) block copolymer confined in about 200 nm wide, intersecting crossed channel architectures and showed that in the intersecting regions the block copolymer oriented in the direction of the electric field vector. However, there has not been any combinatorial study of the effects of electric field alignment supported by the graphoepitaxy. In this chapter we show that macroscopically uni-axial aligned striped patterns with few defects can be fabricated by a combination of graphoepitaxy and electric field-induced alignment. Another competitive effect we consider here is a mass transport due to the polymer flow from the trench walls. We observe that this flow effect competes with the with the orientational effect of the electric field at small trench width and at short annealing times. Further we analyze how the angle between the topographic features and the electric field vector affects the pattern quality and the time required for the ordering. The most important observation is that application of an electric field to block copolymer films supported by topograhically structured substrates allows to achieve perfect uni-axial orientation even when the separations between the trenches are as large as 20 μm, an order of magnitude larger than that required for graphoepitaxy alone. Interestingly, the

uni-axial orientation clearly occurs even when the trench walls and electric field vector were misaligned.

7.2. Experimental

7.2.1. Chrome Mask Preparation

A chromium mask for the electrode patterns was made by photolithography. Each electrode had dimensions of 0.5 cm × 0.5 cm, and pairs of electrodes were separated by a 40 μm wide gap. The chrome-coated glass substrate was exposed to UV-light to define the electrode features using a Heidelberg Instruments μPG 101 (10 mW, 60%) direct write exposure tool. Subsequently, the resist was developed in Microposit 352 developer for 60 s and then rinsed with deionized water. The substrate was then treated with CR7 acid for 70 s to remove the Cr layer. The mask was rinsed with acetone, methanol and isopropyl followed by an O_2 ash for 2 min.

7.2.2. Substrate Preparation

The substrates for the graphoepitaxy-electric field alignment experiments were prepared on polished float glass wafers. The wafers were cleaned in a 7:1:1 mixture of deionized water, ammonium hydroxide and hydrogen peroxide at 70 °C for 20 min. HMDS HP-Primer was spin-cast on the float glass wafer at 800 rpm for 1 s. After drying of the residual primer the positive photoresist S1813 Microposit was spin-cast on the wafer at 5000 rpm for 1 min. The wafer was cured at 110 °C for 2 min.

The float glass wafer was then placed under the chromium mask and exposed to UV-light for 30 s via a Tamarak Scientific Co Inc. light source. The wafer was rinsed with Microposit 352 developer for 45 s to remove the UV-exposed parts of the photoresist. 10 nm of Ti and 100 nm of Au were deposited on the wafer using an electron beam evaporator followed by lift-off to leave gold electrode patterns. For the lift-off process the wafer was heated to 85 °C in 1-methyl-2-pyrrolidone (NMP) for 1 h, followed by 5 s in the ultrasonic bath.

The fin structures for graphoepitaxy were prepared using direct-write photolithography with the Heidelberg Instruments μPG 101. Alignment was necessary to locate the features within the 40 μm electrode gap. HP-Primer as well as the S1813 photoresist were spin coated on the wafer as previously described, then exposed to UV-light (10 mW, 60%). The features had a width of 2 μm and a length 20 μm. The distance between two features varied in 1 μm steps between 1.5 μm and 20.5 μm. The angle of the features with respect to the electrode edges varied in 15° steps. The wafer was rinsed

with Microposit 352 developer for 45 s. Afterwards, 100 nm of SiO_2 were deposited on the wafer via sputter deposition, followed by lift-off. The substrates were cut with a Disco 3240 diesaw.

The resulting substrates consisted of two 100 nm thick gold electrodes separated by a 40 μm gap containing SiO_2 fins of a height of 100 nm, a length of 20 μm, a width of 2 μm and spacing of x = 1.5 μm and above. The angle α between the electric field vector and the fin direction was varied in 15° steps between 0° and 90°. Therefore, each substrate contains fins at α of $0°, 15°, 30°, 45°, 60°, 75°$ and 90°, with fin distances gradually increasing from 1.5 μm to 20 μm.

7.2.3. PDMS Brush Functionalization

A PDMS brush with a molecular weight of 0.8 kg/mol and a silanol end termination was spincoated on the wafer at 3000 rpm for 30 s from a 1 wt% soloution in toluene. The wafer was heated to 170 °C for 12 h under vacuum. The residual PDMS brush was subsequently removed by rinsing the wafer with toluene.

7.2.4. Block copolymer Self-assembly

Thin films of a 1.5 wt% solution of PS-*b*-PDMS in cyclohexane with a molecular weight of 53 kg/mol and a volume fraction of PDMS of 30% (PS-*b*-PDMS) were spincoated on the substrates at 8000 rpm for 30 s resulting in a block copolymer thickness of 50 nm. Solvent vapor annealing was performed in a reservoir system of a volume of 353.4 cm^3 with 3 mL of a 2:1 toluene-heptane mixture. The lid was screwed tightly to the chamber to minimize the solvent escape. The swelling ratio amounted to 2.0-2.1. The film thickness was monitored during the experiment via a Filmmetrics F20-UV.

When an electric field was applied ordering was enhanced by a solvent vapor preanneal, in which the structures were swollen in the solvent vapor for 30 min without the electric field followed by a subsequent anneal under application of an electric field of 12.5 V/μm. We note that immediate application of the electric field at the beginning of SVA did not produce a uniform microdomain array.

When no electric field was applied to the sample the substrates were exposed to the same solvent vapor annealing conditions for 4 h. The PDMS wetting layer forming on the sample surface during SVA due to the low surface energy of PDMS was removed via a 4 s CF_4 reactive ion etch. Subsequently, the sample was exposed to O_2 plasma for 22 s, leaving behind oxidized PDMS domains while simultaneously removing the PS.

7.2.5. Imaging of Nanostructures

Prior to image analysis 2 nm of Au were sputtered on the samples. Image analysis was performed with a Orion He-Ion microscope from Zeiss. AFM measurements were performed with a Nanoscope IV from Bruker.

7.2.6. Color Coding

To better visualize the orientation of the block copolymer as well as the residual defects the large scale images in Figure 7.5 and Figure 7.8 of the main text and in Figure 7.11 and Figure 7.12 of the appendix were color coded using ImageJ software, such that the color corresponds to the orientation angle β of the in-plane cylinders as presented in the color wheels in the respective Figures.

7.3. Results and Discussion

Four different kinds of substrates were utilized in the experiments: as-received Si wafers, Si wafers functionalized with a PDMS brush, two types of substrates supporting Au electrodes for the electric field experiments: with and without topographic features, denoted as EF-GE and EF substrates, respectively. EF-GE substrates contained trenches with varied separations within the 40 μm wide gap between the two electrodes. These substrates were also functionalized with a PDMS brush which presence has been shown to enhance the kinetics of self-assembly during solvent vapor annealing (SVA) [JR07], augmenting the grain sizes of ordered domains. This effect is illustrated in Figure 7.2, which compares films on as-received Si and on PDMS-brushed Si after annealing. A schematic illustration of the electrodes with topographical features for combined graphoepitaxy and electric field guided experiments (EF-GE substrates) is shown in Figure 7.5 (a).

In all electric field experiments a field strength of 12.5 V/μm was applied within the 40 μm gap between the two gold electrodes. The templates for graphoepitaxy consisted of fins made from SiO_2, which was chosen due to its low dielectric permittivity which reduces any effects of the fins on the electric field distribution within the gap. The distance between two fins (x) was varied in 1 or 2 μm steps between 1.5 μm and 20 μm. The angle between the direction of the fins and the electric field vector was varied in 15° increments between 0° and 90°. A detailed description of the substrate-fabrication procedure and further experimental details can be found in the Experimental section.

A 1.5 wt% solution of a poly(styrene)-*block*-poly(dimethylsiloxane) block copolymer with a PDMS volume fraction of 30% and a molecular weight of 53 kg/mol (PS-*b*-PDMS) in cyclohexane was spin coated on the substrates at 8000 rpm resulting in an

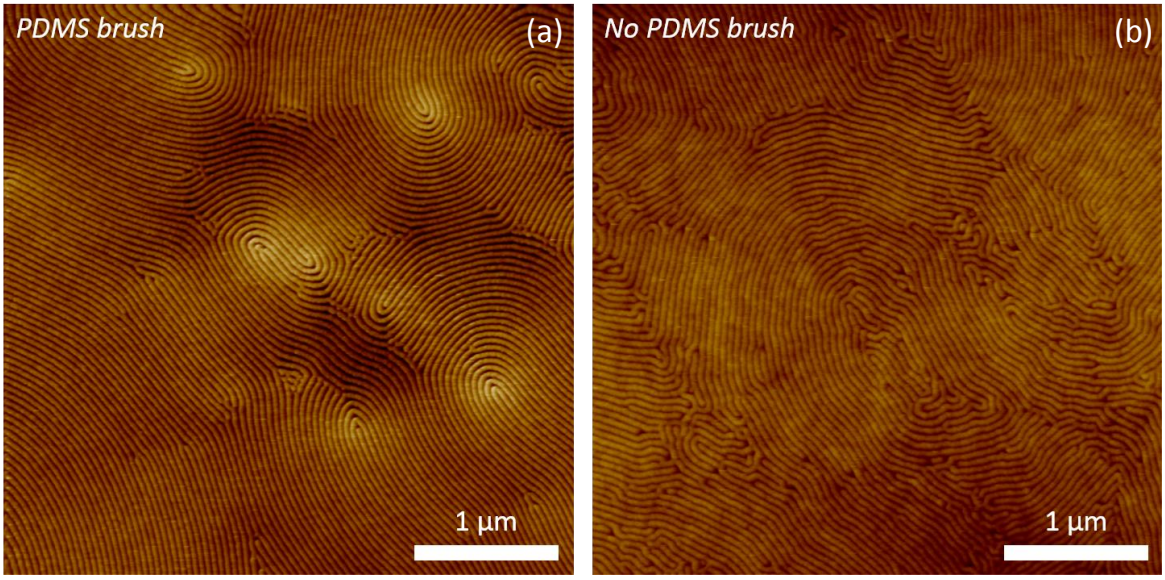

Figure 7.2.: AFM height images of PS-*b*-PDMS after solvent vapor annealing for 4 h under saturated vapor from a 2:1 toluene-heptane mixture on a Si wafer functionalized with a PDMS brush (a.) and on an uncoated Si wafer (b.) The initial film thickness after spin coating was 50 nm. During SVA the swelling ratio was 2.1. The PDMS brush accelerates the alignment kinetics and thus increases the initial domain size of the structures. Prior to AFM imaging the PDMS wetting layer and the PS block were removed by plasma etching. This figure was adapted from Ref. [KBCI*15].

initial film thickness of 50 nm. The block copolymer which was synthesized by anionic polymerization has a cylindrical morphology in bulk and period of $L_0 = 35$ nm [BIH00]. Solvent vapor annealing was performed in different mixtures of toluene and heptane vapors (produced in a closed chamber from liquids of pure toluene, or toluene:heptane volumetric mixtures in the ratio 5:1, 2:1, 4:3) at a swelling ratio of 2.0 - 2.1. The film thickness was monitored during the experiment via a Filmetrics F20-UV spectral reflectometer. Microdomains were imaged by scanning electron microscopy or helium ion microscopy after a short CF_4 plasma etch followed by an oxygen etch, which removed the top surface layer of PDMS, then removed the PS and oxidized the PDMS microdomains [JJTR08].

7.3.1. Solvent Vapor Annealing of PS-b-PDMS Thin Films

A mixture of solvents was used to anneal the PS-b-PDMS block-copolymer. Heptane is a good solvent for PDMS, whereas toluene is a solvent for both blocks but becomes more selective to the PS block in the presence of heptane [HBAKR15].

Therefore, as the fraction of heptane in the vapor increases, the effective volume fraction of PDMS increases. Previously, it was shown that a large variety of thin film morphologies can be obtained from the same block copolymer by merely changing the solvent vapor annealing conditions [BFG*14]. Solvent vapor annealing films of the PS-*b*-PDMS on PDMS-functionalized silicon in pure toluene and toluene:heptane mixtures of 5:1 and 2:1 yielded an in-plane cylindrical morphology. In mixtures containing higher fractions of heptane (toluene:heptane 4:3) the formation of in-plane lamellae and intermediate structures was observed. The lamellae are oriented in plane as a result of the much lower surface energy of PDMS, rendering the lamellar assembly useless for nanolithography purposes. Well-ordered microdomain arrays were produced for swelling ratios ($SR = \frac{h_{swollenfilm}}{h_{unswollenfilm}}$) in the range of 2.0 - 2.1 after 3 h of SVA, where h represents the film thickness.

7.3.2. Electric Field-Induced Alignment of Microdomains under Solvent Vapor Annealing

We first describe the results of electric field alignment of PS-*b*-PDMS in the absence of topographical templates. As can be seen in Figure 7.3, the efficiency of the electric field alignment was sensitive to the composition of the solvent mixture. When the block copolymer was annealed in pure toluene vapor under application of an electric field of 12.5 V/μm no induced alignment was observed (Figure 7.3 (a)), i.e. the 'grains' consisting of in-plane cylinders showed random orientations. Annealing in a vapor from a 5 : 1 toluene-heptane mixture did not produce a preferential orientation after 12 h of SVA, independent of the electric field strength. However, alignment in the direction of the electric field vector was observed after 2 h of SVA in vapor from a 2 : 1 mixture of toluene:heptane at an electric field strength of 12.5 V/μm as presented in Figure 7.5 (c). The results suggest that the PDMS minority block requires a certain degree of mobility, provided by heptane uptake, to be effectively aligned by the electric field. Despite the orientation of the structures, the images in Figure 7.3 (b) and Figure 7.4 display a clear collective tilt of the cylinders away from the direction of the electric field vector as well as several defects. As will be shown later on, this can be eliminated by combining electric field and graphoepitaxy.

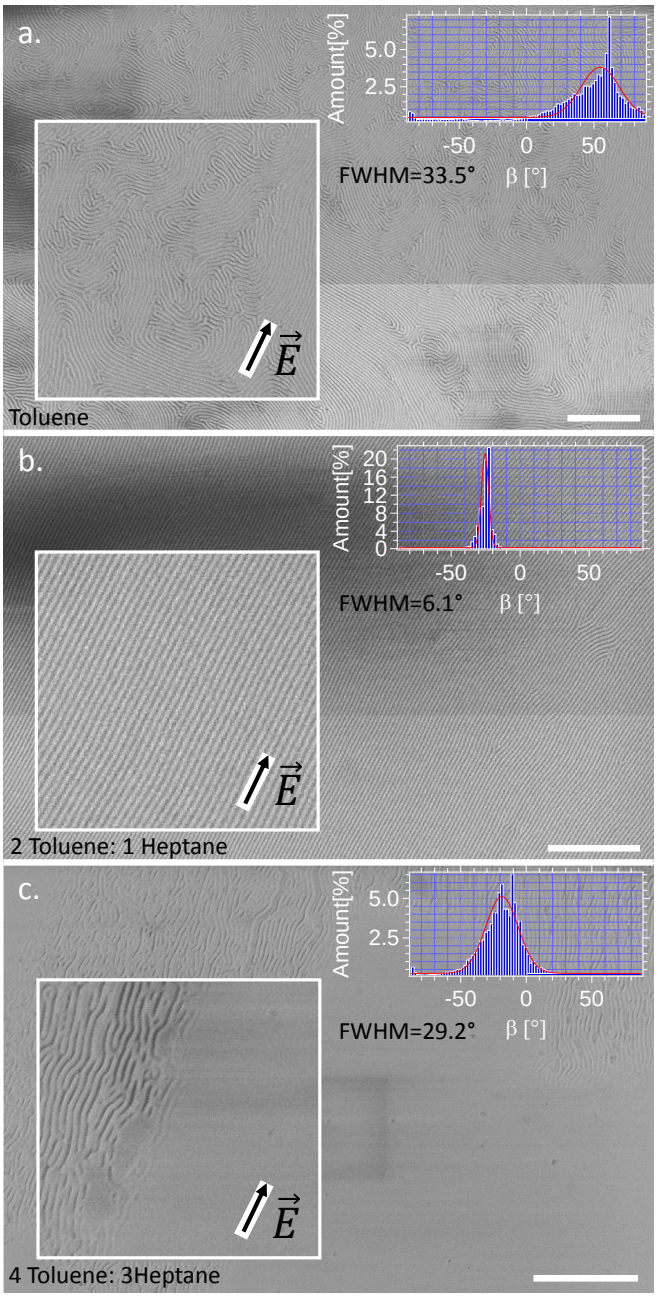

Figure 7.3.: SEM images of PS-*b*-PDMS after solvent vapor annealing for 3 h under saturated conditions at an electric field strength of 12.5 V/μm and a swelling ratio of 2.1 in a vapor of (a.) pure toluene, (b.) a 2:1 toluene-heptane mixture and (c.) a 4:3 toluene-heptane mixture. This figure was adapted from Ref. [KBCI*15].

Typically electric fields with strengths between 10 V/μm and 16 V/μm were reported to induce alignment in block copolymer films of poly(styrene)-*block*-poly(2-vinylpyridine) (PS-P2VP) upon solvent vapor annealing [LSP*13, OHK*09]. In case of thermal annealing of poly(styrene)-*block*-poly(methyl methacrylate) (PS-PMMA) higher field strengths upto 40 V/μm [TS14, XZGR04] had to be utilized to compensate the lower chain mobility in melts despite the fact that the dielectric contrast for PS-PMMA is higher than for PS-P2VP [KKKB15]. The field strength of 12.5 V/μm was chosen since it has a measurable alignment effect on the structure without damaging the copolymer. To quantify the

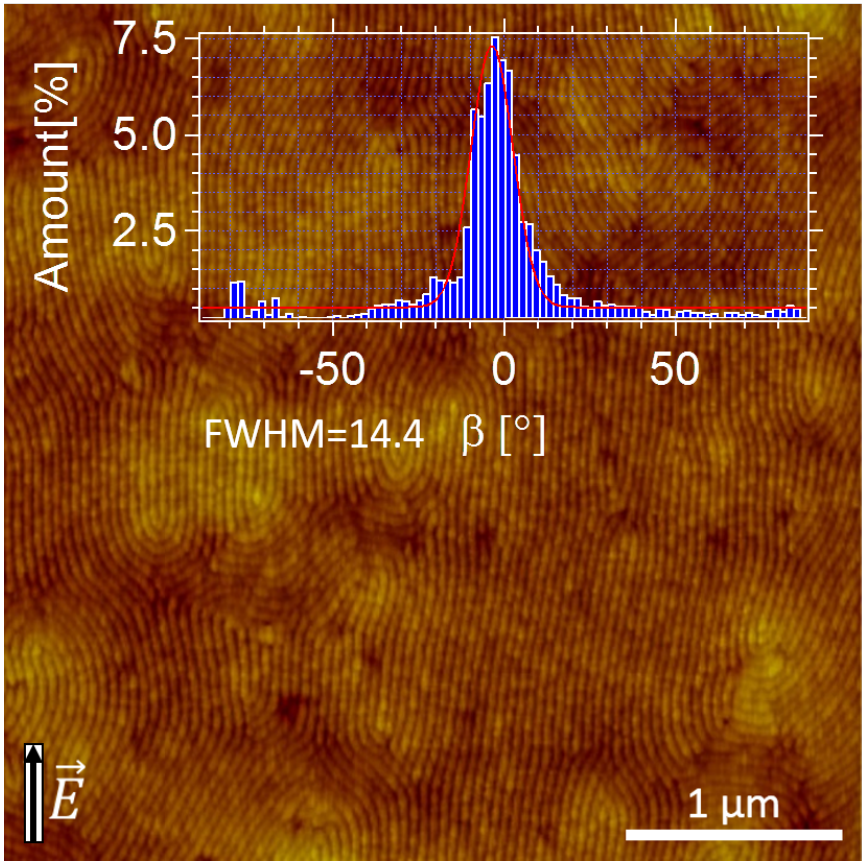

Figure 7.4.: AFM height image of PS-*b*-PDMS solvent vapor annealed for 3 h in a 2:1 toluene:heptane mixture at a swelling ratio of 2.1 under application of an electric field of 12.5 V/μm. This figure was adapted from Ref. [KBCI*15].

degree of orientational order obtained through the application of electric field, images have been processed with Fourier Analysis. The resulting histograms showing the percentage of the stripes versus orientation angle β are displayed in Figure 7.3 and Figure 7.4. Under optimized alignment conditions the full width half maximum (FWHM) of the

orientation distribution was found to lie between 6-15°. Due to the low dielectric contrast between PS and PDMS, which provides the driving force for electric-field-induced alignment, a defect-free structure formation cannot be produced by the application of electric field alignment alone in our system. Based on these results, successive experiments on EF-GE substrates have been performed in a vapor from a 2:1 toluene-heptane mixture which allowed sufficient mobility for the alignment of the microdomains and produced a cylindrical morphology which was visible as a grating pattern after etching.

7.3.3. Graphoepitaxial Alignment of Cylinder Forming PS-b-PDMS Block Copolymer

To analyze the orientational effect of graphoepitaxy, samples were solvent vapor annealed on GE-EF substrates without applying an electric field. A He-Ion image of the microdomain structure obtained after 4 h of SVA for fin spacings of 7 μm is displayed in Figure 7.5 (d). A 4 h anneal did not result in the preferential orientation of microdomains parallel to the fins in the range of fin spacing x between 1.5 μm and 20 μm. The color coding clearly indicates grains with different orientations. The histogram of orientation angles displays a broad alignment distribution with a FWHM of 24.7° according to a Gaussian fitting function.

The corresponding image for a 6 h anneal in a 2 : 1 toluene-heptane mixture at a swelling ratio of 2.1 when the spacing between two fins was 1.5 μm, which was the smallest fin spacing examined is found in Figure 7.7. This was the only spacing for which domain orientation parallel to the fins was found. With increasing x no alignment parallel to the fins was observed even after 12 h of SVA. Figure 7.6 presents a He-Ion microscope image of the SiO_2 sidewall of a graphoepitaxial fin and provides information on the edge quality of the topographic substrates. The sidewall produced from direct-write photolithography is characterized by a high edge roughness of around 80 nm, and the minimum trench width of 1.5 μm is $\sim$ 40 L_0, both factors limit the efficiency of microdomain ordering. We will demonstrate below how the combination of graphoepitaxy and electric field alignment can produce greater degrees of order and orientation than is obtained from either technique alone on such substrates.

7.3.4. Structure Orientation by Capillary Flow

An image of the structures after 4 h of SVA is shown in Figure 7.5 (e) for fin spacings of 5.5 μm. In the absence of an electric field, 4 h of SVA led to a preferred microdomain orientation perpendicular to the fins when the distance between trenches was in the

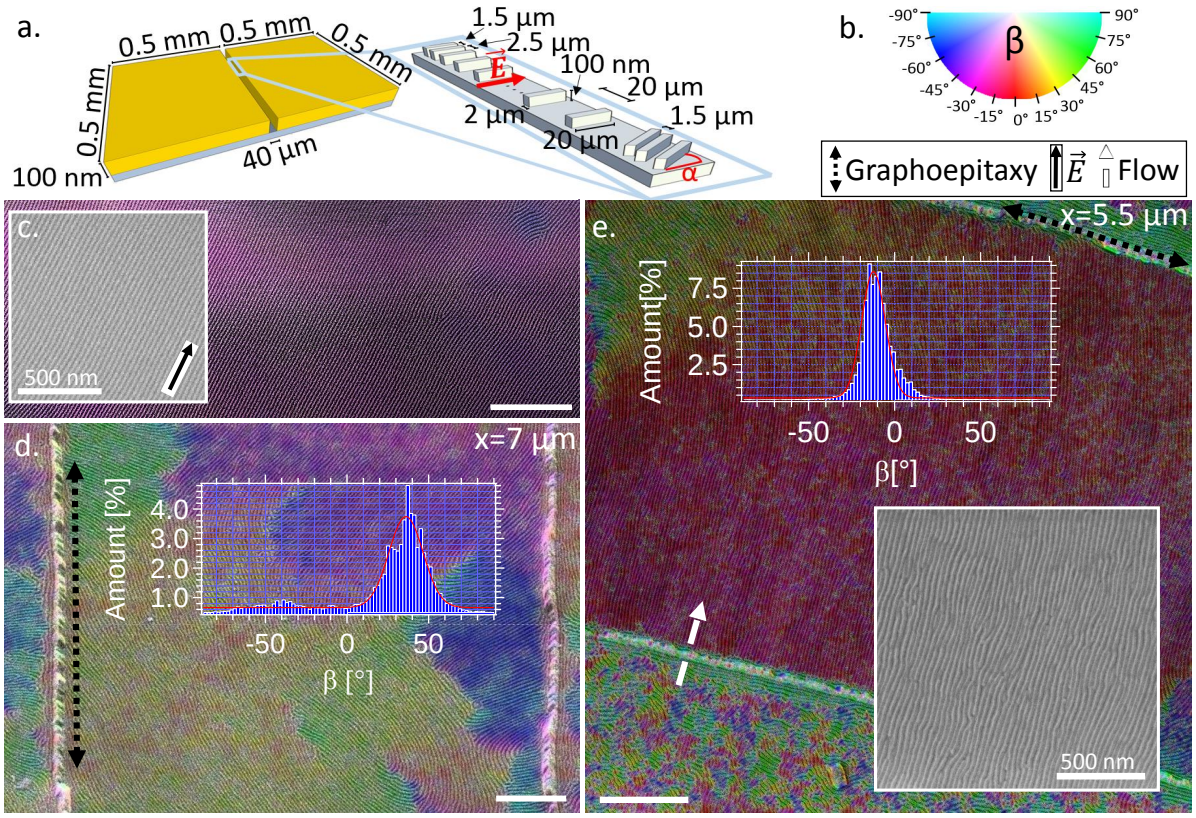

Figure 7.5.: (a.) Schematic illustration of the GE-EF substrate for block copolymer microdomain alignment by combined graphoepitaxy and electric field with the indicated dimensions of the features. (b.) Color wheel showing the angle of microdomain orientation β. (c.) Scanning electron microscope images of PS-*b*-PDMS after solvent vapor annealing for 3 h in vapor from a 2 : 1 toluene-heptane mixture at an electric field strength of 12.5 V/μm. The unlabeled scale bars represent 1 μm. (d.-e.) Color coded He-Ion microscope images of PS-*b*-PDMS after solvent vapor annealing for 4 h in vapor from a 2:1 toluene-heptane mixture on GE-EF substrates functionalized with a PDMS brush. x indicates the trench width (distance between the fins). No electric field was applied during solvent vapor annealing. Histograms presenting the fraction of cylinders in % versus the orientation angle β calculated from Fourier analysis of the images. The insets show a close-up of the block copolymer structure. This figure was adapted from Ref. [KBCI*15].

range between x = 1.5 μm and 6 μm. As indicated by the color coding in Figure 7.5 (e), at x = 5.5 μm the majority of block copolymer domains are oriented at an angle β between $-15°$ and $-30°$. However, regions where the direction of cylinders deviates from the orientation perpendicular to the fin walls can be observed when the trench

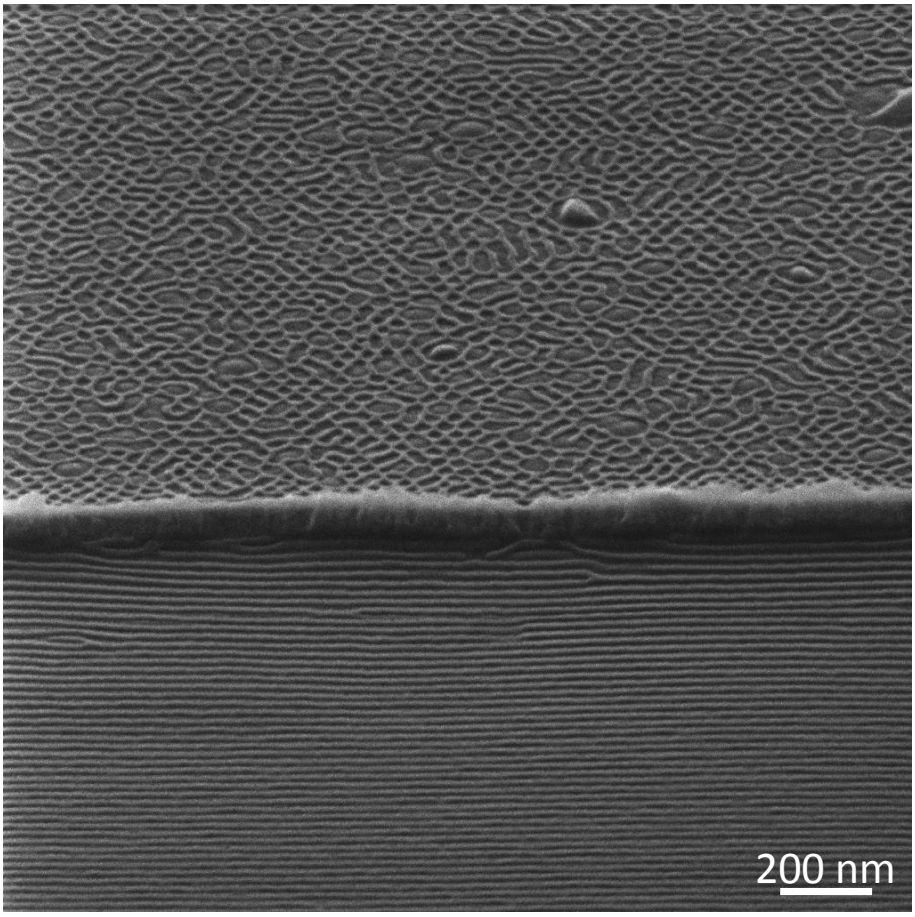

Figure 7.6.: He-Ion microscope image taken of the sidewall of a graphoepitaxy feature on the EF-GE Substrates at a tilt angle of 65°. This figure was adapted from Ref. [KBCI*15].

width approaches the upper limit of 6 μm (see the upper left-hand corner of Figure 7.5 (e)). The SEM image in the inset of Figure 1 e reveals waviness in the cylinder array. In accordance with earlier observations the alignment perpendicular to the trench walls is more pronounced for smaller x [SDS04a, SDS04b, JR07]. This perpendicular orientation is not stable upon annealing times of 6 h or longer. After 6 h of SVA cylinders are perfectly oriented parallel to the fins (Figure 7.7) on the substrates with 1.5 μm wide trenches, while for larger trench widths (2 μm - 6 μm), mixed structures with parallel and perpendicular orientation relative to the trenches with typical grain sizes between 1-2 μm^2 are observed. Between trenches wider than 6 μm no flow induced perpendicular alignment was observed independent of the annealing time.

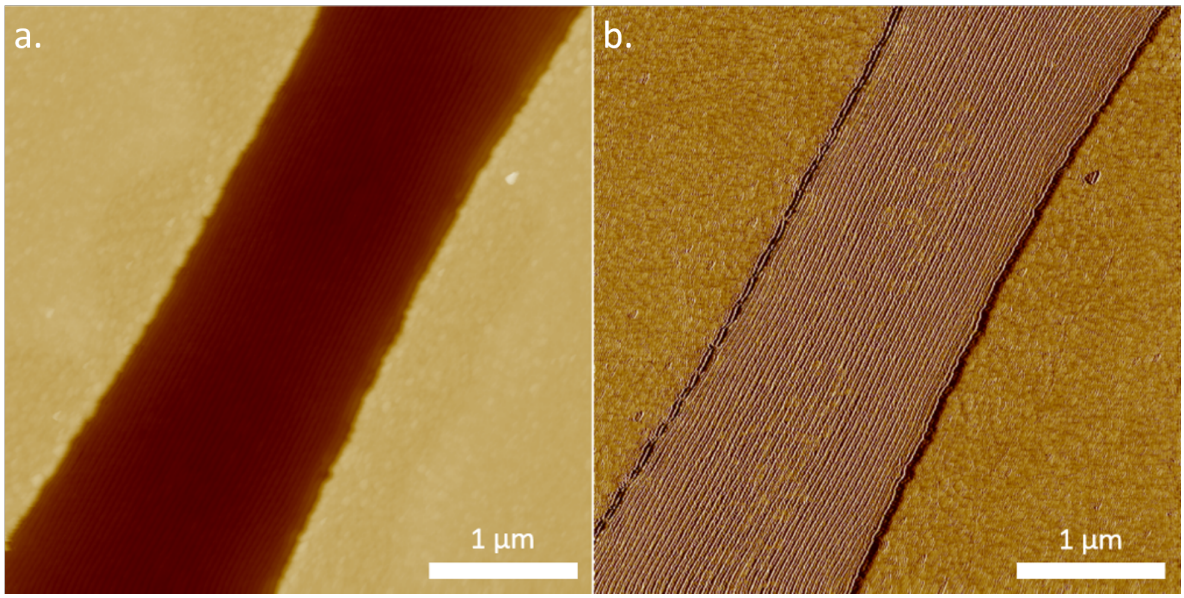

Figure 7.7.: AFM height (a.) and phase (b.) image of PS-*b*-PDMS aligned by graphoepitaxy between fins separated by x=1.5 μm. The sample was solvent vapor annealed in a 2:1 toluene-heptane mixture for 6 h at a swelling ratio of 2.1. This figure was adapted from Ref. [KBCI*15].

7.3.5. Combining Electric Field and Graphoepitaxy

The main results on the combination of graphoepitaxy and electric field are summarized in Figures 7.8 and 7.9, as well as in Figures 7.11 and 7.12. Figure 7.8 (a,b) shows structures with long-range order and a defect density of 0.07 ± 0.005 defects $/\mu m^2$ after 4 h of SVA in a 2:1 toluene-heptane mixture at a swelling ratio of 2.1. In the following the structures are analyzed with respect to the angle α between the orientation of graphoepitaxy and the electric field vector.

Figure 7.8 displays exemplary color coded low magnification He-Ion microscope images of the microdomain array at angles α of 0°, 30°, 60°, 90° as well as histograms with the distribution of the angles of cylinder orientation relative to the electric filed vector. Figures 7.11 and 7.12 present additional information on the preferential orientation of the microdomains depending on the angle α. **α=0°.** Figure 7.8 (a) shows a low magnification image of the block copolymer in the middle of a 20 μm trench when the electric field vector and graphoepitaxy promote alignment in the same direction, at $\alpha = 0$. In this case, the order extends across the full width of the trench for x up to 20 μm after only 4 h of annealing. In comparison, graphoepitaxy by itself provided alignment only within small trenches (1.5 μm) after 6 hours, and larger trench width x showed regions

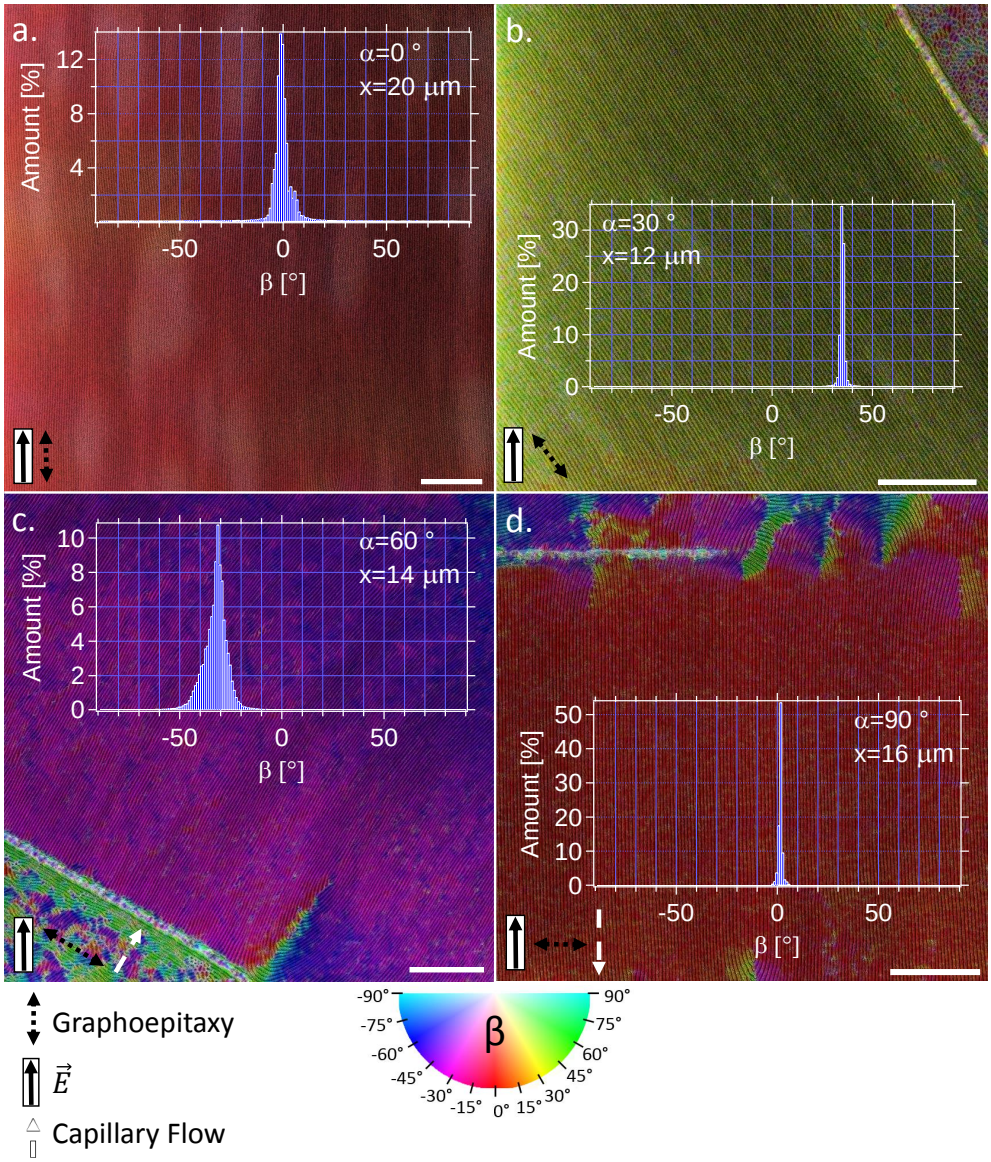

Figure 7.8.: He-Ion microscope images of PS-*b*-PDMS after solvent vapor annealing for 4 h from a 2:1 toluene-heptane mixture under the influence of both graphoepitaxy and an electric field of 12.5 V/μm. α indicates the angle between the electric field vector and the trench edges and x is the trench width. The direction of the graphoepitaxy, flow field and electric field are indicated by the arrows as indicated. The electric field direction is always vertical on the page; β is the angle between the orientation of cylinders and the electric field. For better visualization of the orientational order the images were color coded in accordance with β as indicated in the color wheel. (a.-b.) $\alpha = 0°$ and 30°. The direction of alignment is determined by the graphoepitaxy, but the electric field greatly enhances the correlation length as compared to pure graphoepitaxy. (c.-d.) $\alpha = 60°$ and 90°. The alignment is predominantly perpendicular to the trench wall. This figure was adapted from Ref. [KBCI*15].

of misoriented cylinders with a mixed orientation. The degree of ordering achieved by the combination of graphoepitaxy and electric field greatly exceeds the results obtained by graphoepitaxy or electric field alone.

α=15° and 30° When the angle α was 15° or 30°, alignment of the block copolymer parallel to the fins was found up to the trench widths of 14 μm. An image for $\alpha = 30°$ is shown in Figure 7.8 (b). Figure 7.11 (b) displays the image for $\alpha = 15°$. For a trench width of 16 μm and larger the cylinder orientation was parallel to the trenches at the sidewalls but tilted towards the direction of the electric field vector in the middle of the trench area.

α=45°. At an angle of 45°, alignment parallel to the sidewall was only found for trench widths of 8-14 μm as can be seen in Figure 7.11 (d), with tilts towards the electric field direction at the center of wider trenches.

However, processing the films on the GE-EF substrates with trench widths (x) smaller than 8μm gave qualitatively different results on the preferential domain orientation (Figure 7.8 (c,d) and Figure 7.12). For $\alpha = 45°$ (and higher angles) the domains were found to be oriented perpendicular to the sidewalls which was was attributed to a dominant flow-induced orientation. At $\alpha = 45°$ the electric field favors equally alignment parallel to the sidewall (β= 45 °) and perpendicular to the sidewall (β= -45°). The perpendicular alignment dominates for narrower trenches where flow effects are stronger, but gives way to parallel alignment in wider trenches. Longer anneals would likely promote the parallel alignment as seen by Jung et al. [JR07].

α=60°, 75°, 90°. For trenches making angles of 60° (Figure 7.8 (c)), 75° (Figure 7.12 (c)) and 90° (Figure 7.8 (d)) to the electric field vector the observed alignment was perpendicular to the fins independent of x. Compared to the films annealed without electric field, the perpendicular alignment was observed over a wider range of fin distances up to around 14 μm while the direction of orientation perpendicular to the side wall showed less deviation. The electric field therefore also improves the ordering of structures in which the predominant direction of orientation is perpendicular to the trench walls.

These results indicate that the topography has the greatest influence on determining the microdomain orientation during the annealing of this system, leading to in-plane cylinders lying either parallel or perpendicular to the sidewalls. However, the electric field appears to improve the orientation distribution and defectivity of the microdomain array, and it dominates the microdomain orientation in unpatterned substrates or far ($> 10\mu$m) from step edges.

When comparing the width of the orientational distribution displayed in the histograms in Figures 7.8, 7.11 and 7.12 it becomes evident that structures directed parallel to the side walls yield far better long range order than those oriented perpendicular to

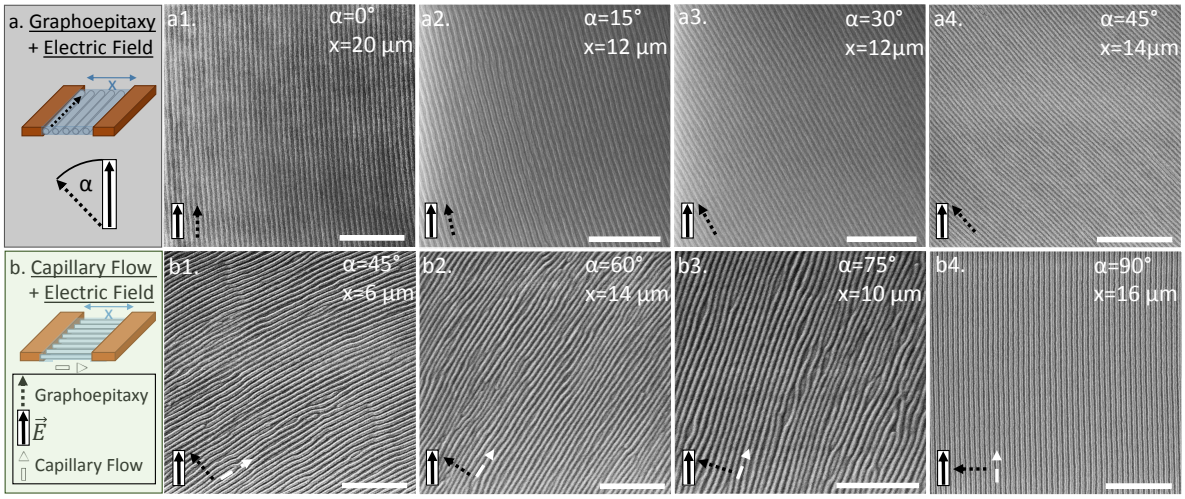

Figure 7.9.: He-Ion microscope images of PS-*b*-PDMS after solvent vapor annealing for 4 h on GE-EF substrates annealed in vapor from a 2:1 toluene-heptane mixture at an electric field strength of 12.5 V/μm. α indicates the angle between the electric field vector and the sidewalls, and x is the trench width. The direction in which the block copolymer is guided due to graphoepitaxy, flow and electric field are indicated by the black and white arrows as indicated. (a1.-a4.) are aligned parallel to the topographic features (b1.-b4.) show cylinders oriented perpendicular to the trench walls. The scale bars display 500 nm. This figure was adapted from Ref. [KBCI*15].

the topographic features. At angles α of 0°, 15° and 30° sharper peaks with FWHM 2 - 5 ° indicating better alignment are observed compared to angles of 60° and 75° with FWHM 10 - 16°. For $\alpha = 45°$, the larger trenches (8-14 μm) in which graphoepitaxy determined the orientation showed a sharper orientation distribution (FWHM = 5.9°) than the narrower trenches where alignment perpendicular to the trench walls dominated (FWHM = 14.8°), seen in Figure 7.11 (d) and (Figure 7.12 (a)). The only exception is the structure found at an angle $\alpha = 90°$ (Figure 7.8 (d)). Here the alignment perpendicular to the trench wall corresponds to the direction of the electric field vector and a narrow distribution of cylinder orientation is observed (FWHM = 1.4°). We now focus our discussion on the comparison of the higher magnification images in Figure 7.9. In each image the direction of the electric field vector, capillary flow and the sidewall is indicated in the bottom left. In the top right α states the angle between the direction of the sidewalls and the electric field vector while x gives the trench width.

In Figure 7.9 (a1-a4) the cylinders are parallel to the sidewalls due to graphoepitaxy. The rms edge roughness is low and there are typically 0.07 ± 0.005 defects per μm^2. In contrast the cylinders in Figure 7.9 (b1-b3) which are perpendicular to the sidewalls

show a larger number of defects of 1.5 ± 0.1 defects per μm^2 and an increased rms edge roughness. The predominant defect type are line breaks. Figure 7.9 (b4) resembles the well ordered structures of Figure 7.9 (a1-a4).

Figure 7.10 (a) summarizes the orientation as a function of the trench width x and the angle α between the direction of the topographic features and the electric field vector, for a given annealing time, 4 h. The blue circles indicate alignment dominated by graphoepitaxy while the red crosses display in plane orientation perpendicular to the trench walls. The green squares indicate cylinders which align in the direction of the electric field vector at the middle of the trench, leading to a polycrystalline structure.

The rearrangement of cylinders from perpendicular to the trench walls into a polycrystalline structure started to occur in samples annealed at 6 h or longer in the absence of an electric field. However, annealing for 12 h in the presence of an electric field preserved the perpendicular alignment. This is illustrated for a sample with α=60° and x=14 μm in Figure 7.10. The orientation remains perpendicular to the sidewall while the number of defects decreased compared to the structures found in Figure 7.9 (b1-b3). Furthermore, alignment perpendicular to the trenches was found over larger spacings ($x \leq 14$ μm) when an electric field was applied to the sample than obtained by capillary flow alone ($x \leq 6$ μm). For large spacings between 12 μm - 20 μm as presented in Figure 7.8 capillary flow is no longer a dominant effect. These observations indicate that the final orientation of cylinders is determined by thermodynamics rather than by kinetic effects such as capillary flow. The low dielectric contrast of 0.17 [KKKB15] between PS and PDMS is presumed to be the reason why the topographic effects dominate the electric field. The selective uptake of solvent during solvent vapor annealing can only slightly increase the dielectric contrast between the blocks. Toluene which preferentially swells the PS ($\epsilon_{PS} = 2.57$) domains has a dielectric constant of $\epsilon_{toluene} = 2.38$ while heptane which is more selective to PDMS ($\epsilon_{PDMS} = 2.40$) has a dielectric constant of $\epsilon_{heptane} = 1.92$. Considering the relatively similar dielectric constants of the individual components the dielectric contrast could at maximum increase to 0.3 upon the solvent vapor annealing conditions described here in case of selective solvent uptake. For comparison, the dielectric contrast of poly(styrene)-*block*-poly(methyl methacrylate), which is often utilized in studies on electric field-induced alignment of block copolymer thin films [XZGR04], is 2.15 [KKKB15], more than 12 times higher than that of the polymer used in this study. For block copolymers with a higher dielectric contrast between the blocks, or with ion-containing blocks, alignment in the direction of the electric field vector would at least be expected for the larger fin spacings. However, despite the modest dielectric contrast, it is clear that the electric field has a profound effect on the orientation, defect level, and kinetics of the PDMS microdomains, and the microdomain orientation is prevented from differing by more than 45° from the direction of the electric field vector.

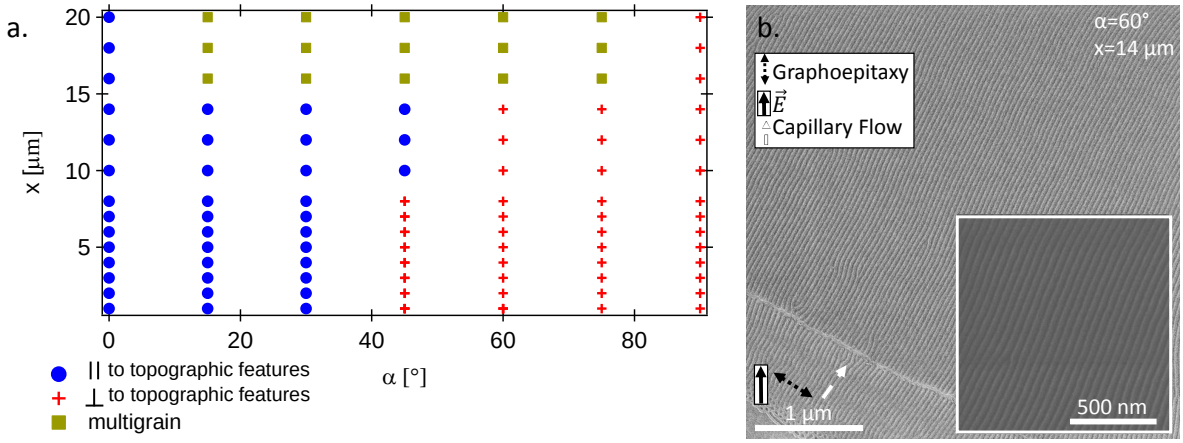

Figure 7.10.: (a.) Phase diagram showing the microdomain orientation as a function of trench width x and the angle between the electric field and the sidewalls. The blue circles indicate microdomain alignment parallel to the sidewalls while the red crosses mark alignment perpendicular to the sidewalls. The green squares indicate mixed structures which in some regions align in the direction of the electric field vector and align according to graphoepitaxy near the sidewalls. (b.) He-Ion microscope images of PS-b-PDMS after solvent vapor annealing for 12 h in a 2:1 toluene-heptane mixture at an electric field strength of 12.5 V/μm. The direction of alignment is perpendicular to the trench wall. This figure was adapted from Ref. [KBCI*15].

7.4. Conclusion

In this study a combination of topographical features and electric field alignment was applied to obtain well-ordered and oriented cylindrical microdomains from a 53 kg/mol PS-*b*-PDMS block copolymer during solvent vapor annealing in a toluene and heptane vapor. Without topographical features, the microdomains aligned with the electric field direction, but topographical patterning led to alignment of the cylinders in plane either parallel or perpendicular to the sidewalls. An electric field oriented within 45 ° of the sidewall promoted cylinder orientation parallel to the sidewall, whereas an electric field oriented between 45° and 90° of the sidewall promoted cylinder alignment perpendicular to the sidewall, over distances of 15 μm or more. The electric field enhanced the kinetics of self-assembly and enhanced the correlation length of the microdomains beyond what could be achieved with either topography or electric field alone. This combined approach produced long-range order in the block copolymer without expensive substrate prepatterning. The use of thermosolvent or other fast annealing processes [KKP*15] may further decrease the annealing time necessary to form a well ordered array.

7.5. Appendix

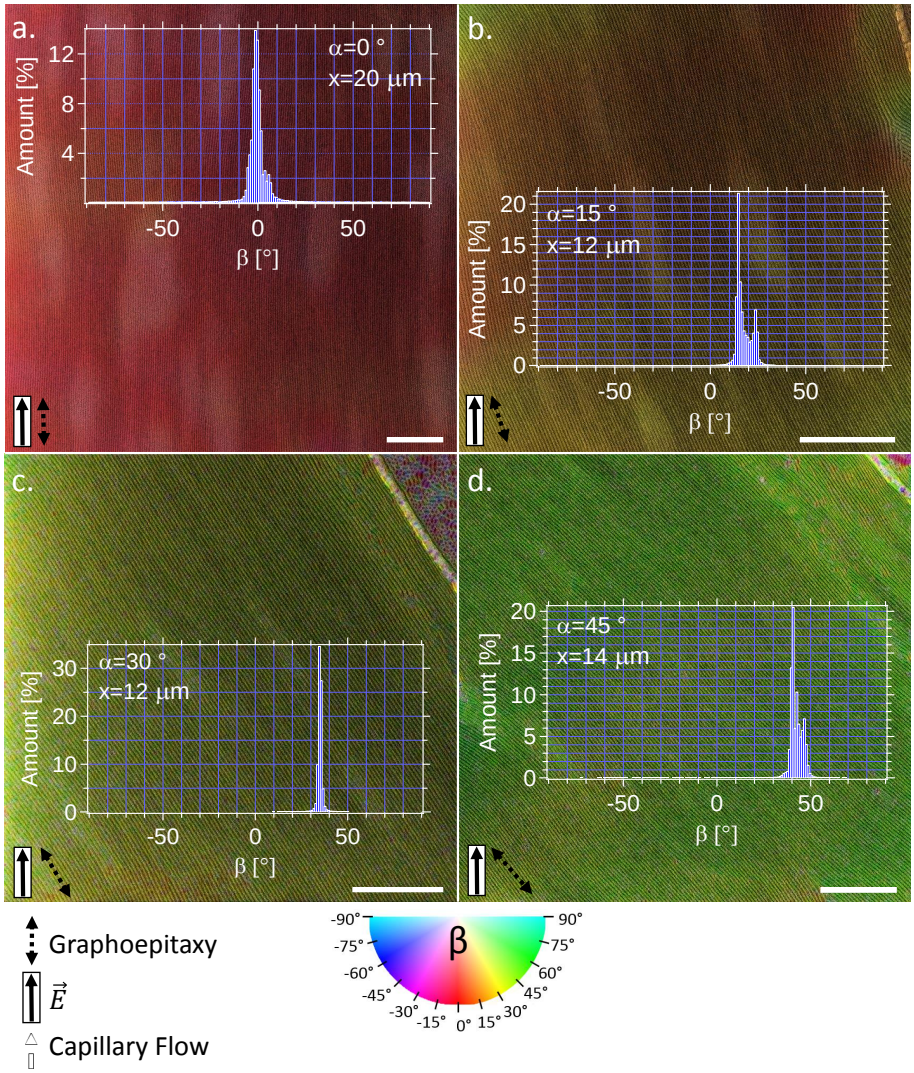

Figure 7.11.: He-Ion microscope images of PS-*b*-PDMS after solvent vapor annealing for 4 h in vapor from a 2:1 toluene-heptane mixture at an electric field strength of 12.5 V/μm. α indicates the angle between the electric field vector and the graphoepitaxy features. x indicates the distance between the fins. The direction in which the block copolymer is guided due to graphoeptiaxy and electric field are indicated by the white arrows. The direction of alignment is determined by graphoepitaxy. The electric field greatly enhances the length scale of long-range order achievable. All images were color coded to visualize the orientation of the block copolymer. This figure was adapted from Ref. [KBCI*15].

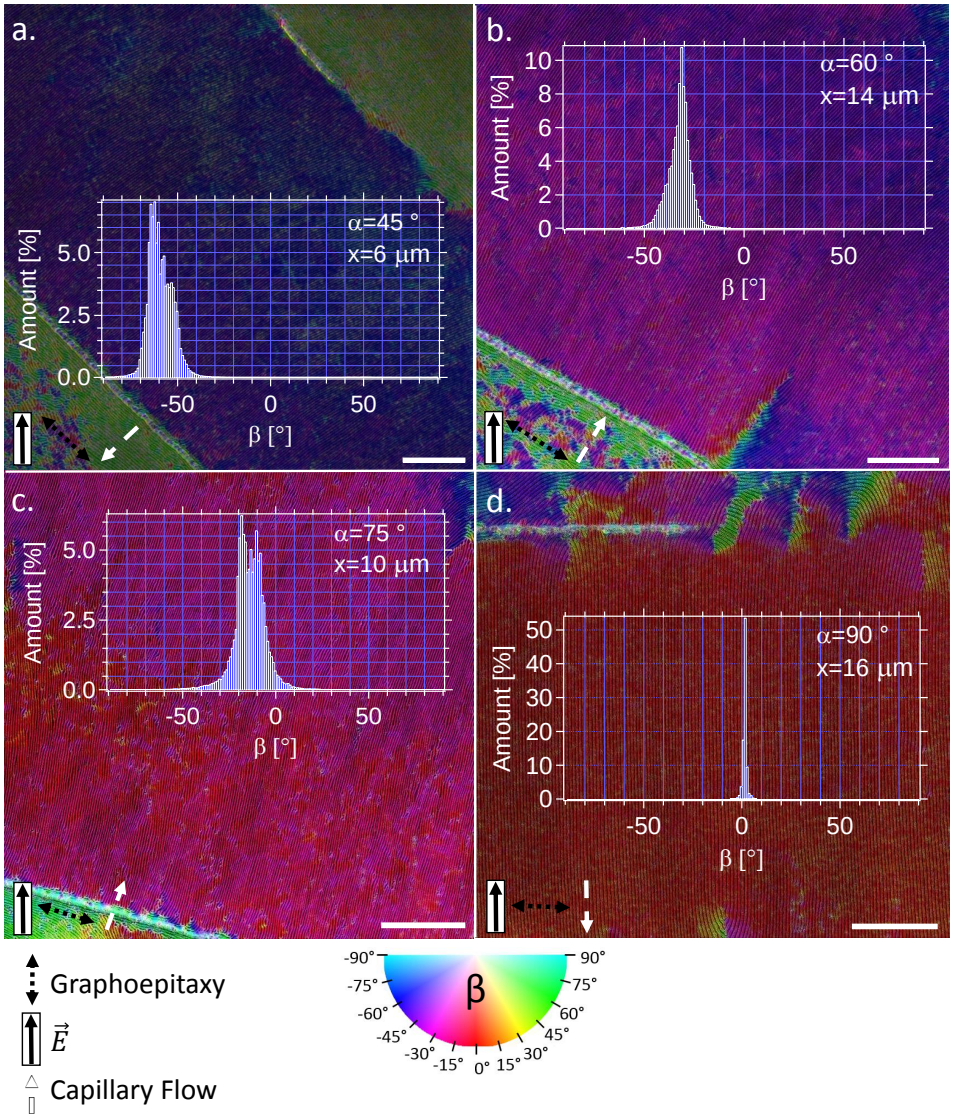

Figure 7.12.: He-Ion microscope images of PS-*b*-PDMS after solvent vapor annealing for 4 h in vapor from a 2:1 toluene-heptane mixture at an electric field strength of 12.5 V/μm. α indicates the angle between the electric field vector and the graphoepitaxy features. x indicates the distance between the fins. The direction in which the block copolymer is guided due to graphoeptiaxy, flow and electric field are indicated by the white arrows. The images were color coded according to the direction of block copolymer orientation. The color wheel in the bottom displays the color as a function of the angle. This figure was adapted from Ref. [KBCI*15].

8. Electric Field-Induced Transitions in Metalorganic 3-Miktoarm Star Terpolymers[1]

8.1. Introduction and Theoretical Background

Thin film morphologies obtainable from diblock copolymers are limited. Star-shaped 3-miktoarm triblock terpolymers (3μ-ABC) exhibit an extraordinary structural diversity and thin films of these materials are of interest in nanofabrication and nanolithography. In contrast to linear ABC terpolymers, the three blocks of a 3μ-ABC polymer are connected at a single junction point. In the microphase-separated structure the junction points tend to assemble along linear or curved trajectories defining the vertex between the three microdomains [YAH05]. Such geometrical constraint together with the minimization of unfavorable contacts between incompatible blocks gives rise to novel morphologies not observed for linear triblock terpolymers.

Simulations [GHD02], bulk- [HI93] and thin film studies [ACN*13] of different 3μ-ABCs revealed a large variety of structures such as several Archimedean tilings [HDTM07, HKT*06, YTH03] composed of coaxial prisms including the space groups c2mm, p3m1, p4mm, p6mm, and p4gm. Also, three-colored honeycomb structures were observed provided that the interaction parameters and volume fractions of the three components are of about equal value [DH96, TWS*04]. Strongly differing χ parameters were found to result in partial mixing of blocks minimizing the contact area between the constituents with the energetically most unfavorable interaction parameter [SHT98b, SHT98a]. Key parameters determining the morphology are the block lengths, the selectivity of solvents used for annealing, segment-segment interaction parameters, as well as chain deformation energies [SHT98b], and in the case of thin films, surface and interface energies are also important. The annealing conditions, for example variations in composition and

[1] This Chapter and its figures have been published in modified form [KBN*15]. C. C. Kathrein, W. Bai, A. Nunns, J. Gwyther, I. Manners, A. Böker, L. Tsarkova, and Caroline A. Ross, Electric-field-induced Morphological Transitions in Thin Films of Metalorganic 3-Miktoarm Star Terpolymers, *Soft Matter* **2016**, Advance Article, DOI:10.1039/C6SM00451B.

vapor pressure of solvents, also affect the resulting morphologies [ACN*13]. Further, specific functionalities of the blocks contribute to the hierarchical complexity of the nanostructures.

Polymers comprising polyferrocenylsilane (PFS) blocks represent an interesting class of materials since they combine the structural diversity of multiblock polymers with the unique physical properties of the PFS block, such as electroactivity and electrochromism which arise from the presence of transition metals in the polymer backbone [ZWM14, KM01]. These materials can be used as precursors for magnetic materials by oxidation or pyrolysis [FZT*93, LZR*08, GMY*02, RRV*97]. Upon iodine doping, PFS has also been shown to exhibit p-type conductivity [BSR*01]. Prior work showed that 3-miktoarm star terpolymers of polyisoprene-*arm*-polystyrene-*arm*-poly(ferrocenylethylmethylsilane) (3μ-ISF) form a variety of different thin film microstructures, influenced by the film thickness and by the partial pressure of chloroform vapor in the annealing chamber, which controls the swelling and relative volume fraction of the polyisoprene block [ACN*13]. This illustrates that small changes in the effective volume fraction can alter the thin film structure.

Previously electric fields have been shown to induce ordering and phase transitions in thin film and bulk diblock copolymers. The basic concept determining the behavior of *non-metal-containing* block copolymers in electric fields is the unfavorable electrostatic energy of block-block interfaces oriented perpendicular to the electric field vector (**E**) with respect to those aligned parallel to **E**. Electric-field-induced ordering and defect annihilation have been thoroughly investigated since the work of Amundson et al. in 1991 [AHD*91, OHK*06, OHK*09, BSK*06, BEH*03, WLBSR06, WXLB*06, MLU*96, AHQS93, AHQ*94]. Reorientation of dielectric interfaces parallel to the electric field vector is the anticipated response when a certain threshold voltage, dependent on the annealing conditions, is exceeded.

Polyferrocenylethylmethylsilane (PFEMS) block-containing copolymers are expected to have a notable response to an electric field due to the iron atoms complexed inside the microdomains, similar to the reported enhanced ordering effect of LiCl salt added to polystyrene-*block*-poly methyl methacrylate diblock copolymer [WXLB*06]. Earlier studies describe the influence of electrochemical oxidation and applied voltage on the electroactive PFS block. Electrochemical oxidation was analyzed by Shi et al. who observed a more than 70 % increase in the Kuhn segment length of poly(ferrocenylmethyl-(phenyl)silane) and poly(ferrocenyl dimethyl silane) polymers upon electrochemical oxidation of the ferrocenyl groups [SCW*04]. Due to the electrostatic interactions between positive charged segments a stretched conformation of chains is favored to maximize the distance between like charges [ZHSV06]. Analyzing the effects of voltage, Li et al. measured a widening of PFS cylinders by up to 100 % in a cylinder-forming polystyrene-

block-poly(ferrocenylethylmethylsilane) (PFEMS-*b*-PS) block copolymer with conductive probe atomic force microscopy upon application of a negative voltage bias between -4 V and -9 V [LZR*08]. The electric field strength is therefore envisaged to be an additional control parameter determining the thin film morphology.

In this chapter we report the effect of the electric field on the morphological development and ordering of nanostructures in swollen thin films of diblock copolymers and 3-miktoarm star terpolymers containing a functional PFEMS block. The ordering and morphological behavior of the diblock copolymers exhibit two effects of an electric field: an increase in the volume fraction of the PFEMS block by oxidation of the ferrocenyl groups leading to a morphological transformation, and orientation of the dielectric interfaces parallel to **E**. Microdomains of 3-miktoarm star terpolymers exhibit ordering and a sequence of phase transitions with increasing electric field strength. At moderate field strengths the observed phase transitions can be attributed to the electrostatic energy penalty associated with dielectric interfaces not aligned parallel to **E** [OHK*06, OHK*09, BSK*06, BEH*03, WLBSR06, WXLB*06, MLU*96, AHQS93, AHQ*94]. At higher electric field strengths the electroactive response of the PFEMS block becomes the dominant factor determining the morphological transition. Such dual responsive behavior facilitates structural switchability and provides a high degree of ordering upon application of electric field stimuli.

8.2. Experimental

8.2.1. Polymers

PS-*b*-PFEMS sphere- and lamellae forming polymers were synthesized as described earlier [RCPB*05]. The sphere-forming diblock copolymer had a molecular weight of 100 kg/mol and a volume fraction of PFEMS of 16%, while the lamellae-forming PS-*b*-PFEMS had a volume fraction of PFEMS of 43 % and a molecular weight of 58 kg/mol (PDI=1.04). The later was blended with polystyrene homopolymer (homo-PS) (7.7 kg/-mol, PDI=1.1) to obtain a cylindrical morphology. The volume fraction of homo-PS was 17 wt%.

The 3-miktoarm star terpolymers were synthesised according to Nunns et al. [NRM13] A 3-miktoarm star terpolymer with a composition of 39 vol% of polyisoprene, 35 vol% of polystyrene and 26 vol% of poly(ferrocenylethylmethylsilane) was utilized in which the individual blocks had molecular weights of 23 kg/mol, 22.5 kg/mol and 20.5 kg/mol, respectively. To promote the formation of ordered microdomains, 15 wt% of homo-PS with a molecular weight of 12.5 kg/mol and a PDI of 1.04 was added to the copolymer [ACN*13].

8.2.2. Thin Film Preparation

Thin films of the sphere-forming polystyrene-*block*-polyferrocenylethylmethylsilane (PS-*b*-PFEMS) were spin coated for 30 s at 4000 revolutions per minute (rpm) from 2 wt% solutions in toluene. The initial film thickness prior to solvent vapor annealing was 50 nm. 2 wt% solutions of the cylinder forming PS-*b*-PFEMS/homo-PS blend in toluene were prepared by spin coating at 3000 rpm for 30 s yielding an initial film thickness of 50 nm. 45 nm thick films of the 3μ-ISF/homo-PS blend were obtained by spin coating from a 1.5 wt% solution of the polymer in toluene at 3000 rpm for 30 s.

8.2.3. Solvent Vapor Annealing

The thin films exhibited swelling ratios ($SR = \frac{h_{swollenfilm}}{h_{unswollenfilm}}$) of $1.7 - 1.8$ upon exposure to a continous flow of chloroform vapor produced by bubbling N_2 gas through a $CHCl_3$ reservoir and directing the vapor through the solvent vapor annealing chamber. Swelling ratios were controlled by adding a separate stream of N_2. The annealing chamber had a volume of 353.4 cm^3. A quartz lid was tightly screwed to the top of the chamber which allowed the measurement of the swelling ratio via a Filmmetrics F20-UV spectral reflectometer during the experiment. The thin films were exposed to the solvent vapor for two hours and were then quenched within 1 s by removing the lid of the chamber.

8.2.4. Electric Field

Experiments were conducted on oxidized silicon wafers and on glass slides with two gold electrodes, each 0.5 cm $\times$ 0.5 cm and 100 nm thick. Experiments at fixed electric field were performed on samples with gold electrodes separated by a 40 μm wide gap. An electric field of 10 V/μm was applied between the electrodes during solvent vapor annealing.

To vary the electric field strength within a single experiment, substrates with a stepwise varying gap size between 9.3 μm and 78 μm were utilized as schematically shown in Figure 8.1 (c). This led to electric field strengths between 1.9 V/μm and 16 V/μm when a voltage of 150 V was applied between the two gold electrodes. This assured comparable conditions of film thickness and swelling ratio during solvent vapor annealing leaving the electric field strength as the only variable.

8.2.5. Imaging

Prior to imaging the thin films were exposed to O_2 plasma for 12 s which selectively removed the PI and PS domains and oxidized the PFEMS domains. AFM measurements

were performed with a Nanoscope IV from Bruker using a super fine probe (μmash HiRES-W/8/A/BS, 75 kHz, 3.5 Nm). An Orion He-Ion microscope from Zeiss was used to image samples coated with a 2 nm thick layer of sputtered Au. To stain the samples after annealing, the thin films were placed in a chamber with an aqueous solution of OsO_4 (4 wt%) for 4 h. OsO_4 selectively binds to the PI domains increasing its contrast in the He-Ion images.

8.3. Results and discussion

Thin films of a cylinder and a sphere forming PS-*b*-PFEMS block copolymer or blend, as well as of a 3-miktoarm star terpolymer with PS, PI and PFEMS blocks were analyzed after solvent vapor annealing in chloroform, with and without an applied electric field.

8.3.1. Sphere-forming PS-b-PFEMS Diblock Copolymers

Figure 8.1 (a) displays a 50 nm thin film of a 100 kg/mol PS-*b*-PFEMS block copolymer with a volume fraction of PFEMS of 16% solvent vapor annealed in $CHCl_3$ vapor for 2 h. After removal of the PS matrix via an O_2 plasma etch, AFM analysis reveals poorly ordered PFEMS spheres with diameter of 43 nm $\pm$ 2 nm. In contrast, Figure 8.1 (b) displays a film that was solvent vapor annealed under the same conditions but including an electric field of 10 V/μm. Closepacked spheres coexist with regions of striped patterns (in-plane cylinders) with random orientations relative to the direction of the electric field. Considering that the film thickness is sufficient to accomodate only a monolayer of in-plane cylinders, we believe the closepacked features are spheres rather than vertical cylinders. Furthermore, vertical cylinder formation is unlikely to be induced by the electric field because this maximizes unfavorable dielectric interfaces perpendicular to **E**. This morphological behavior suggests that on the one hand, the electric field induces ordering of the spherical morphology, and on the other hand, promotes an order-order phase transition from spheres to cylinders.

It is known that in bcc or gyroid morphologies, frustration occurs independent of the orientation of the microdomains with respect to **E** [Tso09, XZS*04]. Sphere ordering does not lead to a reduction of dielectric interfaces perpendicular to **E**. In these cases, electric fields induce phase transitions into uniaxial structures when the composition of the block copolymer is near a phase boundary [Tso09].

Xu et al. demonstrated that the improvement of the long-range order in a bcc phase of a non-metal-containing block copolymer upon application of electric fields can only be accomplished by first inducing an order-order phase transition from spheres into a

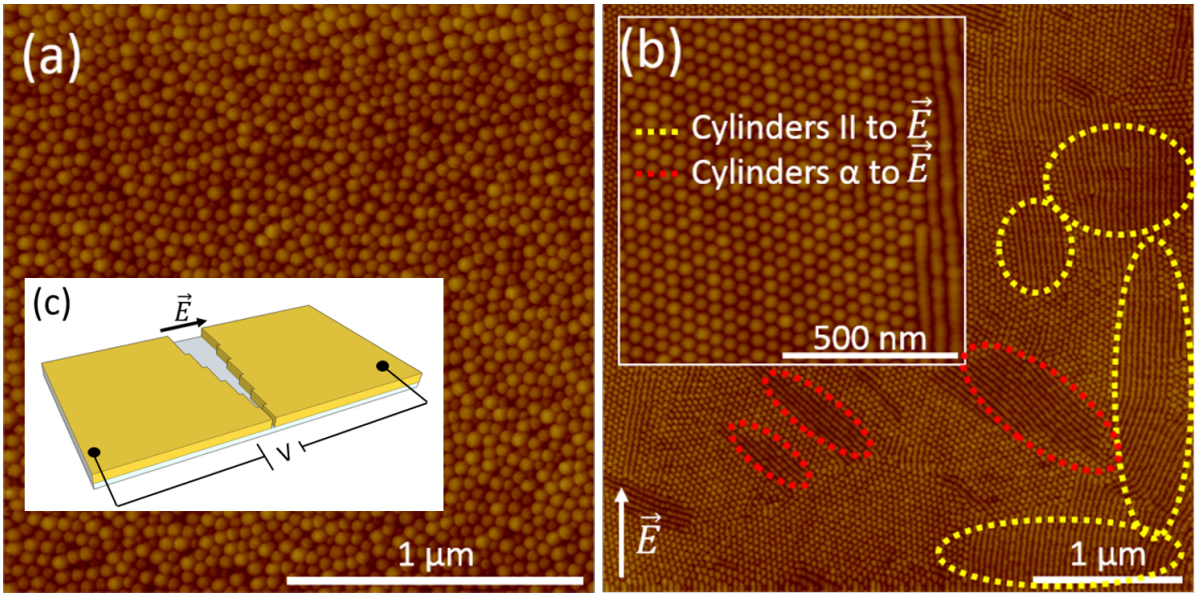

Figure 8.1.: AFM height images of sphere-forming PS-*b*-PFEMS block copolymer thin films after solvent vapor annealing in $CHCl_3$, (a) without and (b) with application of an in-plane electric field of 10 V/μm. The electric field induces ordering as well as a sphere-to-cylinder transition. Cylinders parallel to **E** are marked with a yellow dashed line while those at angles to **E** are indicated by a red dashed line. (c) Schematic image of the substrates. This figure was adapted from Ref. [KBN*15].

cylindrical microdomain structure which is aligned by the electric field, and by subsequent reformation of the bcc structure [XZS*04]. This stands in clear contrast to the results of our experiments which show that improved ordering can be achieved in bcc forming thin films of PS-*b*-PFEMS without requiring a phase transition into an uniaxial phase. We therefore conclude that the improved order may be related to polarization of the iron-containing PFEMS spheres, which is specific for block copolymers with a metal-containing minority block.

On the other hand, electrochemical oxidation [SCW*04] as well as application of voltage [LZR*08] have been reported to alter the microstructure of PFEMS-containing block copolymers due to the effective increase of the volume fraction of the electroactive PFEMS block. As example, Peter et al. reported electrochemically induced volume and morphology changes in surface grafted PFS layers upon applying voltages between 400 mV and 600 mV. [PHK*04] The change of volume in these redox-active monolayers was attributed to a reversible oxidation increasing the charge density in the polymer backbone. It was postulated that the increased charge density attracts additional counterions as well as solvent molecules, resulting in an overall increase of the layer thickness.

In our case, the effective increase of the volume fraction of the PFEMS block may lead to a thermodynamically driven phase transition in sphere-forming PFEMS-*b*-PS diblock copolymer to form the cylinder phase, unlike the kinetically-driven transformation discussed above. The additional charges associated with the oxidation of the ferrocenyl groups might increase the selective solvent uptake of the PFEMS block resulting in an enhanced PFEMS volume fraction and therefore a sphere to cylinder phase transition. The electric field would further enhance the polarity difference between polar PFEMS and non-polar PS, increasing chloroform solubility in PFEMS [Bar90, Gar66]. The possibility of this scenario is supported by the fact that only about half of the striped domains are oriented along the direction of the electric field, so the reduction of the fraction of the electrostatically unfavorable interfaces oriented perpendicular to the electric field vector is not the overriding factor determining the cylinder formation.

8.3.2. Cylinder-forming PS-b-PFEMS Diblock Copolymer Blends

Further insights into the response of PFEMS-containing block copolymers towards electric field was gained by considering the behavior of a cylinder-forming block copolymer blend. Figure 8.2 (a) and (b) displays AFM images of surface structures in 50 nm thick films of PS-*b*-PFEMS/homo-polystyrene (homo-PS) blend upon 3 h of annealing in chloroform vapor without and with applied electric field, respectively. The thin films of the cylinder-forming PS-*b*-PFEMS blend were prepared by adding polystyrene homopolymer to a lamellae- forming PS-*b*-PFEMS block copolymer. The unblended diblock copolymer exhibits an in-plane lamellar morphology.

Figure 8.2 (a) displays cylindrical domains which have been equilibrated under solvent vapor without application of electric field for 3 h. Image analysis revealed a correlation length of ordered grains of 600 nm. When an electric field of 10 V/μm was applied (Figure 8.2 (b)) the correlation length was enhanced to several μm^2.

The cylinder-forming PS-*b*-PFEMS/homo-PS blend was also analyzed on electrodes with varying gap size to alter the electric field strength. In Figure 8.2 (c) the increase in PFEMS volume is plotted against the electric field strength. The cylinder widths were measured from He-Ion microscope images via Image J software. For each field strength the average width was measured from five areas of three different images each. The increase in cylinder volume was calculated according to $V_{add.}[\%] = (\frac{{r_2}^2}{{r_1}^2} \times 100) - 100$, in which r_1 is the PFEMS cylinder radius at zero electric field while r_2 is the radius measured at the respective electric field strength. Exemplary He-Ion images corresponding to the field strengths 1.7 V/μm and 10.9 V/μm are displayed in Figure 8.2 (d,e). The results clearly show an increase in cylinder width with electric field strength when a threshold voltage of 2 V/μm is exceeded. We presume this electroactive response oc-

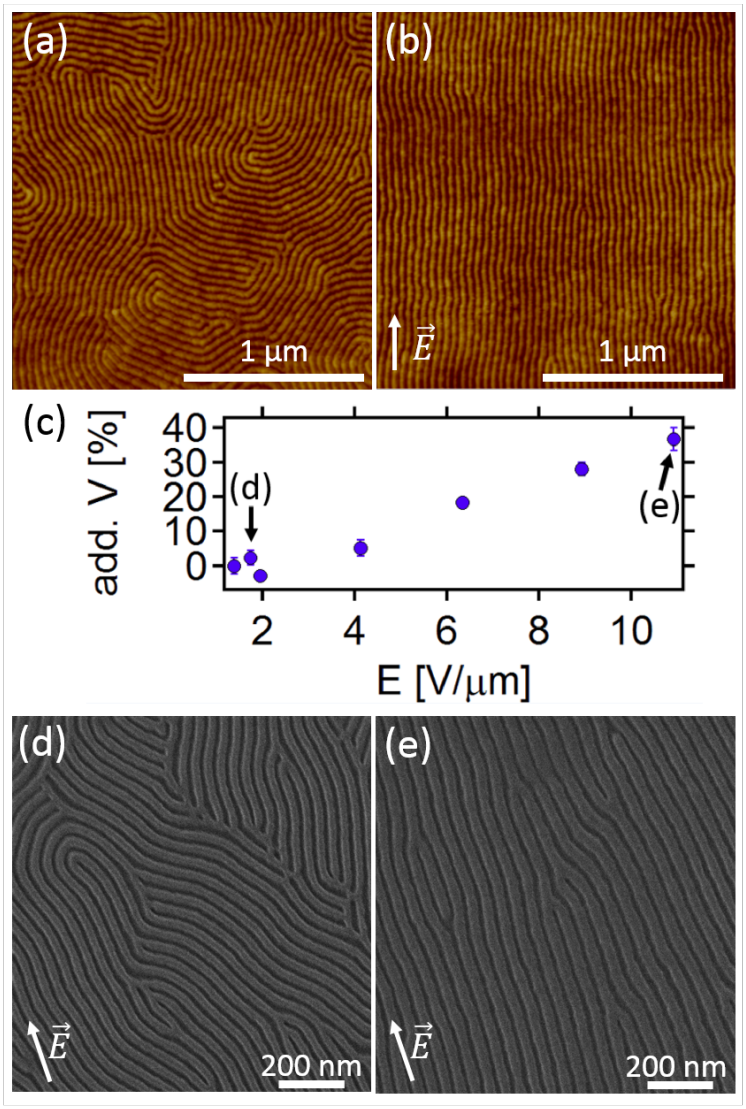

Figure 8.2.: (a,b) AFM height images of a cylinder-forming PS-*b*-PFEMS/homo-PS blend after solvent vapor annealing in chloroform (a) without and (b) with the application of an electric field of 10 V/μm. (c) Graph showing the increase in PFEMS cylinder volume in % vs the applied electric field strength in V/μm. He-Ion images of the cylinder forming PS-*b*-PFEMS/homo-PS blend after solvent vapor annealing under application of an electric field of (d) 1.7 V/μm and (e)10.9 V/μm. The oxidized PFEMS block appears light gray, and the dark gray regions correspond to the removed PS block. This figure was adapted from Ref. [KBN*15].

curs because the high voltage partially induces an oxidation from Fe(II) to Fe(III). The positive charges along the polymer backbone promote a stretched polymer chain confor-

mation increasing the distance between like-charged segments. Considering the dipole moment of chloroform it is assumed that the increased positive charge in the polymer backbone enhances the selective solvent uptake of chloroform by the PFEMS block compared to the unoxidized polymer [PHK*04]. This results in an increase in the PFEMS volume fraction and therefore in PFEMS cylinder width. In our case the highest applied field strength led to an increase by about 37 %, significantly less than the up to 100 % widening measured with conductive probe atomic force microscopy in cylinder forming PFEMS-*b*-PS block copolymer upon application of a negative voltage bias between -4 V and -9 V [LZR*08]. This implies that only parts of the ferrocenyl groups were oxidized [ZHSV06]. For block copolymers such as polystyrene-*block*-poly(methyl methacrylate) or polystyrene-*block*-polyisoprene which are solely composed of organic blocks no alteration in volume fraction is anticipated upon application of electric field.

The results reveal that the electric field has a profound effect on the ordering and phase transitions of PS-*b*-PFEMS block copolymers. This is due to two factors: an increase in the volume fraction of the PFEMS block by oxidation of the ferrocenyl groups which can drive a morphological transformation, and the anticipated orientation of the dielectric interfaces to lie parallel to **E**. We now show how these factors affect the microphase separation of 3-miktoarm star terpolymers of PS, PI and PFEMS.

8.3.3. Surface Structures in Solvent Annealed Films of 3μ-ISF/Homo-PS Blends

Surface structures of the 3μ-ISF/homo-PS blend in 45 nm thick films were analyzed after annealing in chloroform vapor and compared to those subjected to electric field of varying strength during solvent vapor annealing. Choi et al. [CNS*14] previously reported that the film thickness can have a major influence on the thin film morphology of miktoarm star terpolymers. To exclude differences in film thickness from spin-coating or terracing, the morphology at different field strengths was compared on a single sample. A schematic image of the sample is given in Figure 8.1 (c).

The analysis and identification of the thin film structure can be complicated by surface fields, i.e. the difference in interfacial energies between the block copolymer constituents at the film surface [LTK10], which may lead to a distortion of a unit cell [Tsa12, KTK07], as well as redistribution of the blocks at film interfaces, inducing non-bulk morphologies [KHL*02]. A further variable is introduced by the addition of PS homopolymer which enhances chain relaxation. Without the addition of this compatibilizer the equilibrium structure of 3μ-ISF in thin films is lamellar, with the majority PI block segregated to the free surface due to its low surface tension, while the two other blocks form the bottom layer of the lamella.

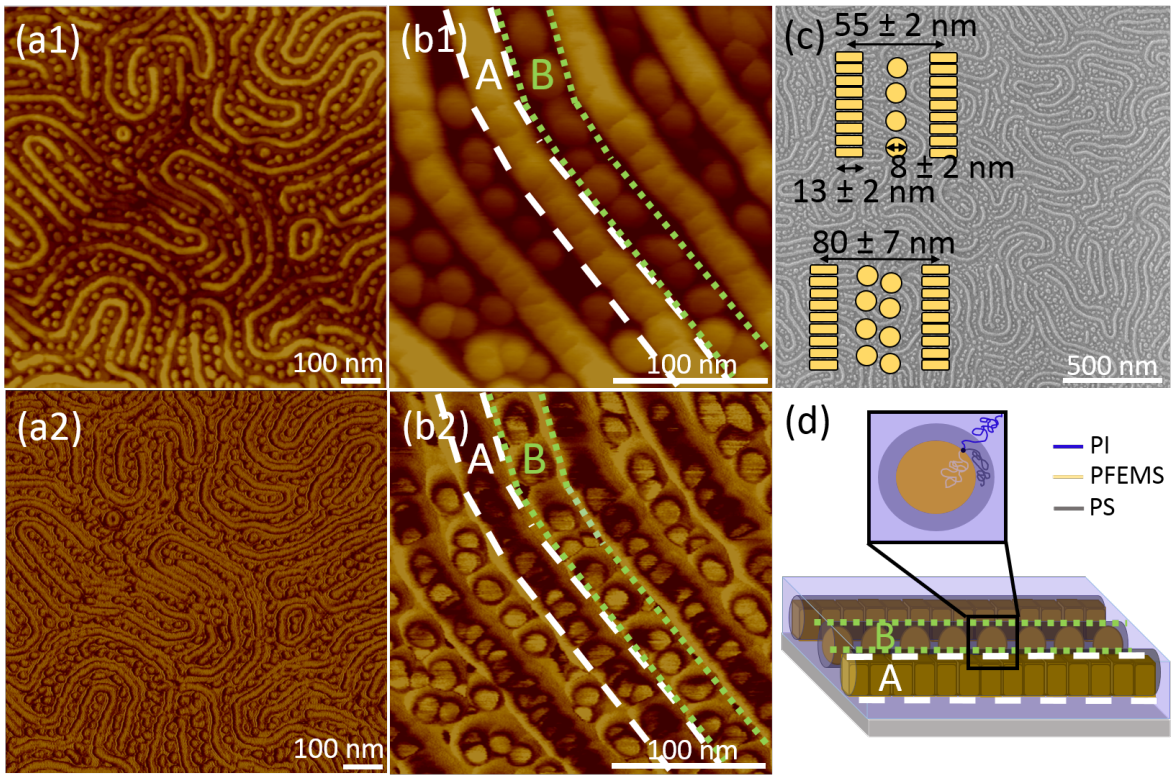

Figure 8.3.: AFM height (a1, b1) and phase (a2, b2) images of the 3μ-ISF/homo-PS blend after solvent vapor annealing in chloroform for 3 h. A and B mark the two different types of spheres. (c) He-Ion image of the same sample. (d) Schematic of the observed structure formed through partial mixing of the PI and the PS block. This figure was adapted from Ref. [KBN*15].

Surface structures in blended 3μ-ISF films are shown in Figure 8.3 (a,b) where (b) is higher magnification. (a1,b1) are height and (a2,b2) are phase images. Prior to imaging, an O_2 plasma etch was applied to remove the top wetting layer of the soft PI block in order to reveal underlying microphase-separated structures. The plasma etches away the PI domains faster than the PS domains [ACN*13], and simultaneously oxidizes the PFEMS block. As shown in Figure 8.3 (a1), the 3μ-ISF copolymer assembles into alternating stripes and dot-like structures, which appear as two types of spheres (marked as A and B structures) in the close-up images in Figure 8.3 (b1, b2). While A-type structures appear as higher (brighter) cylinders in the height images (b1), the phase images (b2) reveal soft (dark) shells around a hard core, where the core is most likely made of the oxidized PFEMS block. In contrast, in B-type spheres the hard core is surrounded by two shells: a thin layer of harder shell formed, presumably, by PS

homopolymer and an outer dark (soft) PI shell. The two types of structures also differ in their shapes, with type B having a spherical morphology, and type A spheres having a distorted anisotropic shape, making them directionally assembled into cylinders.

Considering the room temperature χ parameters $\chi_{\text{PFEMS-}b\text{-PS}} \sim 0.08 < \chi_{\text{PI-}b\text{-PS}} \sim 0.1 < \chi_{\text{PI-}b\text{-PFEMS}} \sim 0.17$ [ACN*13], and the fact that the degree of polymerization (N) of the three blocks is of about equal value, it becomes apparent that the contact between PI and PFEMS is energetically most unfavorable. Therefore, the contact area between PFEMS and PI is minimized by the formation of a PS shell surrounding the PFEMS microdomains. This requires partial mixing of the PS and PI domains [SHT98b] as schematically demonstrated in Figure 8.3 (d) since the three blocks are connected at a single junction point. A schematic illustration of the proposed structure is given in Figure 8.3 (d). A possible reason for the formation of two different types of spheres could be the addition of PS homopolymer. Yamauchi et al. found that the addition of poly(dimethylsiloxane) homopolymer to a 3 miktoarm star terpolymer of polyisoprene-*arm*-polystyrene-*arm*-poly(dimethylsiloxane) led to defects through irregular distribution of the homopolymer throughout the microdomain structure [YAH05]. Therefore, we conclude that the homo-PS is selectively adsorbed to every second row of spheres (B) forming a thicker PS shell around them which allows a wider spacing between the spheres and a non-distorted spherical morphology. The close packing and deformation of the spheres (A) agglomerated into cylindrical structures can be attributed to the strong tendency of the polymer to decrease the unfavorable PI/PFEMS contact under these annealing conditions. Furthermore, the formation of two different types of spheres underlines that the volume ratios between the blocks are not ideal for single pattern formation but are intermediate to two different structures [YAH05].

Figure 8.3 (c) shows a He-Ion image of the sample. Prior to imaging the PI domains were selectively stained with OsO_4. The mean dimensions of the structures were measured via image J software and displayed as insets in Figure 8.3 (c). The PFEMS domains appear light gray in the He-Ion images while the PI and PS phases are darker gray and hard to distinguish.

8.3.4. Effect of Electric Field Strength on the Thin Film Structure of 3μ-ISF/homo-PS

To analyze the effect of the electric field on the thin film structure, 45 nm thick films of the 3μ-ISF/homo-PS blend were spin coated on substrates with a stepwise varying gap size between the two gold electrodes, so that the electric field strength was varied between 2.0 V/μm and 16.0 V/μm in a single film.

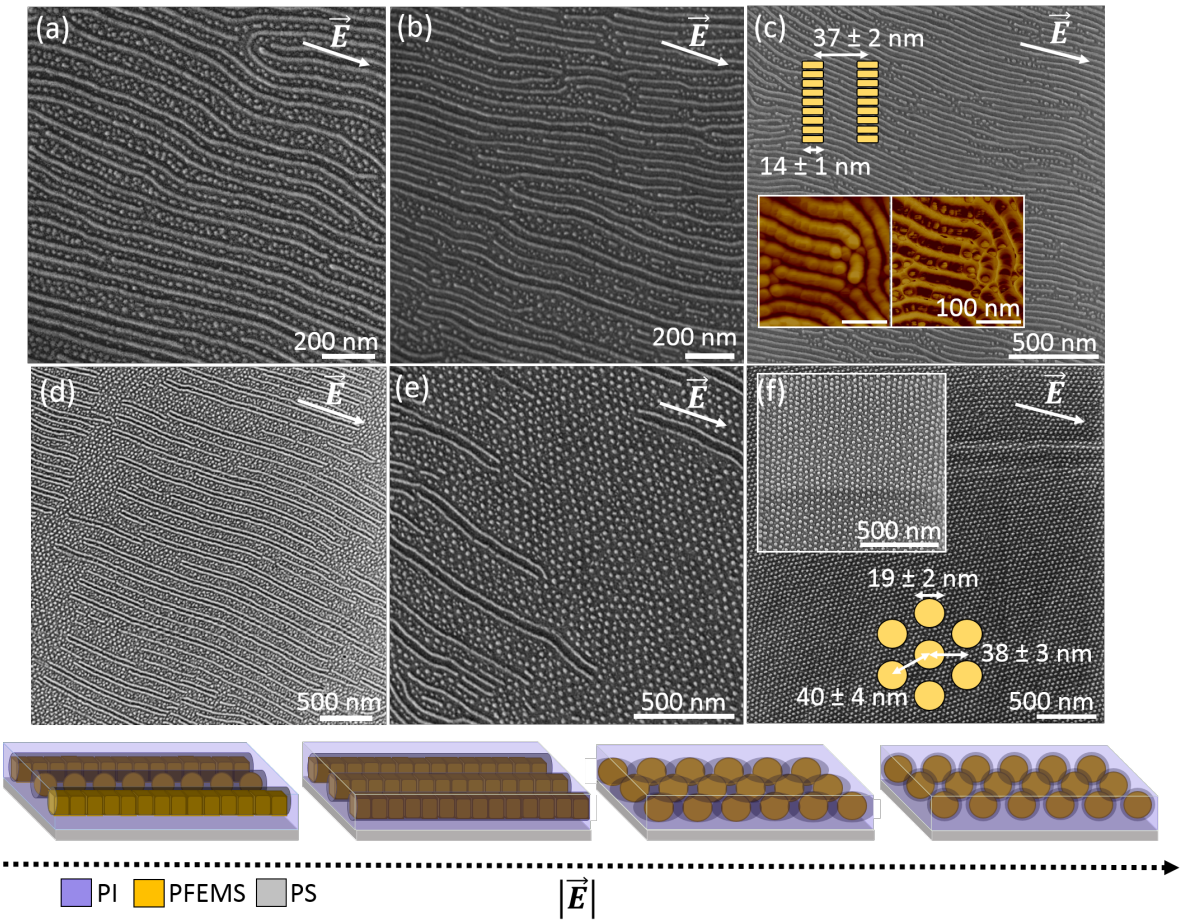

Figure 8.4.: He-Ion microscope images of the 3μ-ISF/homo-PS blend after solvent vapor annealing for 3 h at an electric field strength of (a) 2.0 V/μm, (b) 2.4 V/μm, (c) 2.7 V/μm, (d) 3.2 V/μm, (e) 3.9 V/μm and (f) 4.8 V/μm. The dimensions of the structures were measured from the He-Ion images and are indicated in the schematics in the images displaying the PFEMS block. The inset in (a) shows the AFM height and phase images of the structure measured with an ultrafine probe. Below the image a schematic of the proposed structural evolution upon application of **E** is given. This figure was adapted from Ref. [KBN*15].

The structural evolution with increasing electric field is displayed in the He-Ion images in Figure 8.4 and may be compared to the structure annealed in zero field (Figure 8.3). A schematic of the structures is given underneath the images. The dimensions of the pattern features were measured via image J software and are indicated in the images. Since the structural evolution with increasing field strength is monitored on a single sample (see Figure 8.1 (c)) the film thickness, terracing, and plasma etching conditions

are constant at different field strengths. Furthermore, a smooth transition from one structure to the next is observed which also supports the assumption that the structural evolution is not caused through different terracing conditions upon altering the field strength.

At moderate electric field strengths the cylinders of micellar aggregates start aligning in direction of the electric field vector, decreasing the area of PI/PS and PS/PFEMS interfaces perpendicular to **E** (Figure 8.4 (a)). The area of perpendicular interfaces is even further minimized when the spherical type-B spheres deform into type-A spheres with further assembly into a cylindrical aggregate at higher |**E**| as displayed in Figure 8.4 (b, c). The AFM height and phase image in the inset of Figure 8.4 (c) show that the structure still comprises tightly connected type-A spheres. Up to this point the behavior can be explained as the anticipated response of a copolymer upon exposure to an electric field.

Further increase of |**E**| results in a second phase transformation into well-ordered spherical domains (type-C spheres) as displayed in Figure 8.4 (d-f). Upon evaluation of the structural dimensions, it becomes apparent that the spherical micellar structure forms from the cylindrical one (type-A spheres). The distance between two rows of type-C spheres in Figure 8.4 (f) is 38 nm ± 3 nm and is therefore in the range of the spacing measured between two rows of type- A spheres (37 nm ± 2 nm) in Figure 8.4 (c). Due to this structural evolution the micellar arangement is well ordered since the cylinders formed from the distorted type-A spheres were aligned by the electric field prior to the phase transformation. A schematic of the structural evolution with increasing electric field strength is displayed in the bottom of Figure 8.4.

On first sight this second phase transition seems counterintuitive since the portion of interfaces perpendicular to **E** is again increased. This can be explained when considering the results obtained from the diblock copolymers of PFEMS-*b*-PS under application of an electric field. The dominant driving forces inducing the phase transition from B-type into C-type spheres are the increase in PFEMS volume fraction due to the electroactive response of the PFEMS block. The additional positive charge increases the selective solvent uptake of the PFEMS block and forces the polymer to maximize the distance between like-charged segments thus resulting in a micellar arrangement with an average center to center distance of 40 nm. As previously demonstrated by Aissou et al., small changes in the relative volume fractions of the blocks greatly influence the thin film morphology [ACN*13]. While the relative amount of PI can be altered by controlling the swelling degree, the volume fraction of PFEMS can selectively be tuned by the electric field strength applied to the thin film structure.

8.4. Conclusion

This chapter reports the first analysis of the effect of electric fields on the structure formation in 3-miktoarm star terpolymer thin films with PI, PS and PFEMS blocks blended with homo-PS, as well as the effect of electric field on sphere- and cylinder forming diblock copolymers and blends. In the diblock copolymers, electric field increased the volume fraction of PFEMS, drove a sphere-cylinder transition, and led to alignment of cylinders. In the star terpolymer blend, the solvent-annealed film consisted of two types of spheres. Electric field drove two different phase transitions. At moderate electric fields, ordering and a phase transition due to a reduction of dielectric interfaces perpendicular to **E** is found. At higher electric field strengths, the electroactivity of PFEMS is exploited to induce a morphological transition as the oxidation of the ferrocenyl groups in the PFEMS block increases the PFEMS volume fraction. Furthermore, charging effects are also expected to have an influence on the morphology. This work therefore demonstrates the extensive tunability of the microdomain morphology and orientation of block copolymers with an iron-containing block by annealing in an electric field which could make them useful in nanofabrication or surface patterning applications.

9. Conclusion

In this thesis new insights into the effect of electric fields on phase transitions and ordering of block copolymer nanostructures could be gained. While the bulk analysis of block copolymer solutions was performed at the DWI - Leibniz Institut für Interaktive Materialien at RWTH Aachen University the experiments on thin films were conducted in the group of Prof. Caroline A. Ross at the Massachusetts Institute of Technology.

In the first part of this thesis we show how birefringence measurements can be used to analyze block copolymers under the influence of electric fields. In some cases e.g. when determining the order-disorder transition temperature the birefringence measurements with their excellent time resolution can substitute the synchrotron SAXS measurements which enables extensive analysis as demonstrated in Chapter 4. In other cases e.g. when evaluating order-order transitions between uniaxial and cubic morphologies birefringence measurements are a valuable supplementary method to synchrotron SAXS since they allow the preanalysis of samples and screening of experimental conditions under which the transition takes place. Consequently, the limited measurement period at the synchrotron can be used very effectively. Additionally reorientation kinetics, threshold voltages and the kinetics of electric field-induced mixing can be monitored via optical analysis. To assure constant conditions the sample cell developed in this thesis (Chapter 3) was designed in such a way that it can likewise be used for birefringence and SAXS measurements by simply switching the glass slides for Teflon covered capon sheets. An incorporated PT100 thermosensor and Peltier element allows precise temperature regulation while the parallel gold electrodes connected to a Heinzinger power source assure the formation of homogeneous electric fields of tunable field strength.

In Chapter 4 the intensively discussed question why homogeneous dc electric fields induce mixing of block copolymer microphases, while theoretical considerations predict a shift of the T_{ODT} in the opposite direction could be answered. The electric field-induced shift in T_{ODT} was analyzed for various block copolymers at different electric field strengths. A correlation between the dielectric contrast of the block copolymer constituents and the degree to which the T_{ODT} is shifted to lower values upon application of the electric field was found. Furthermore, it could be demonstrated that the effect becomes more pronounced with increasing chain length of the polymer.

In Chapter 5 the difference in time constants τ between two reorientation mechanisms (Rotation of Grains, Nucleation and Growth) under the influence of electric fields is exploited to analyze the effect of nanoparticles on the reorientation mechanism. While previous studies analyzed the switch in reorientation mechanism of block copolymer solutions under the influence of strong dc electric fields via synchrotron SAXS, we show how the mechanistic alteration can be detected using birefringence analysis. We found that the nanoparticles enlarge the temperature range in which nucleation and growth is the prevailing pathway of realignment.

A further phase transition analyzed in this thesis is the electric field-induced gyroid-to-cylinder transition. The screening of samples and experimental conditions was performed via birefringence measurements. Subsequently, the samples were measured under optimized conditions via time-resolved *in-situ* synchrotron SAXS at the European Synchrotron Radiation Facility (ESRF) in Grenoble, France. The mechanism of the electric field-induced gyroid-to-cylinder transition and the reverse transition after turning off the electric field were unveiled. While the previous one proceeds via an initial distortion of the gyroid phase and subsequent growth of cylinders, three different mechanisms were found for the later. Lower temperatures and field strengths promote the transition via metastable intermediate structures. The intermediate structures found were an HPL and additional connections within the gyroid phase. At higher field strengths and temperatures an intermediate free nucleation and growth pathway from the cylinder phase is observed.

The research to the last two chapters of this thesis was pursued at the MIT. In Chapter 7 we show how long range ordering can be improved in thin films of cylinder forming polystyrene-*block*-poly(dimethylsiloxane) by a combined directing effect of graphoepitaxy and electric fields. The angle α between the electric field vector and the topographic guides for the graphoepitaxy approach was varied between 0 ° and 90 ° in 15 ° steps. Furthermore, the trench width was altered stepwise between 1.5 μm and 20 μm. The length scale of long-range ordering could be enhanced by an order of magnitude by this combined approach even if the direction in which the polymer is guided by graphoepitaxy and electric field did not coincide. Between α of 0 ° and 45 ° the block copolymer oriented parallel to the topographic guides while the cylinders aligned perpendicular to the electric field for α between 45 ° and 90 °. Through the combined approach the fabrication of highly ordered block copolymer structures is possible by using macroscopically pre-patterned photolithographic substrates.

Further structural diversity can be achieved by adding a third block to the polymer. Hence, Chapter 8 focuses on electric field-induced phase transitions in thin films of star-shaped 3-miktoarm triblock terpolymers composed of PI, PS and PFEMS. We show that the metalorganic PFEMS block alters the behavior of the polymer upon exposure to elec-

tric fields compared to the other block copolymers analyzed in this thesis. Additionally, to the previously described effect of ordering the volume fraction of PFEMS is enhanced with increasing electric field strength due to oxidation of the ferrocenyl groups. Therefore, different electric field strength dependent morphological transitions are observed. The results demonstrate the multiple tunability of the ordered microdomain structure by simple stimuli application.

Summarizing different aspects of electric field-induced ordering and phase transitions in various block copolymer systems were analyzed in this thesis enhancing the understanding of the effect of electric fields on the block copolymer phase diagram and pointing out possible future applications.

10. Glossary

Table 10.1.: Abbreviations and Polymers

AFM	Atomic Force Microscopy
BCP	Block Copolymer
BDS	Broadband Dielectric Spectroscopy
BSE	Backscattered Electrons
CL	Cylinder
ESRF	European Synchrotron Radiation Facility
FE	Field Emission
FWHM	Full Width Half Maximum
G	Gyroid
HPL	Hexagonal Perforated Lamella
L	Lamella
NG	Nucleation and Growth
NMR	Nuclear Magnetic Resonanz
ODT	Order Disorder Transition
PDI	Polydispersity Index
PDMS	Poly(dimethylsiloxane)
PEEK	Polyetheretherketone
PEM	Photo elastic modulator
PFEMS	Polyferrocenylethylmethylsilane
PFS	Polyferrocenylsilane
PHEMA	Polyhydroxyethylmethacrylate
PI	Polyisoprene
PMMA	Polymethylmethacrylate
POM	Polarization Optical Microscopy
PS	Polystyrene
PS-*b*-PDMS	Polystyrene-*block*-poly(dimethylsiloxane)
PS-*b*-PI	Polystyrene-*block*-polyisoprene
PS-*b*-PMMA	Polystyrene-*block*-poly(methyl methacrylate)

PS-*b*-P2VP	Polystyrene-*block*-poly(2-vinylpyridine)
PtBMA	Poly(tert-butyl methacrylate)
P2VP	Poly(2-vinylpyridine)
RG	Reorientation of Grains
S	Sphere
SANS	Small Angle Neutron Scattering
SAXS	Small Angle X-ray Scattering
SE	Secondary Electrons
SEM	Scanning Electron Microscopy
SSL	Strong Segregation Limit
SVA	Solvent Vapor Annealing
TA	Thermal Annealing
T_{ODT}	Order Disorder Transition Temperature
3-μISF	polyisoprene-*arm*-polystyrene-*arm*-poly(ferrocenylethylmethylsilane)
WSL	Weak Segregation Limit

Table 10.2.: Abbreviations and Physical Constants

A	Amplitude
α	Thermoelectric strength
B	Magnetic Flux Density
b_i	Scattering Length
c	Speed of Light
D	Electric Displacement Density
Δ	Phase Shift
$\Delta\epsilon$	Dielectric Contrast
E	Electric Field Strength
e	Ellipticity
e	Electron charge
ϵ	Dielectric Constant
f	Eree Energy Density
ϕ	Compositional Order Parameter

f_A, f_B	Volume Fractions
F_es	Electrostatic Energy
Γ	Phaseretardation
γ	Conductivity
H	Magnetic Field Strength
$\langle h^2 \rangle_0$	mean-square unperturbed end-to-end distance
h	Planck Constant
I	Intensity
λ	Wavelength
m_e	Electron mass
μ	Chemical Potential
N	Degree of Polymerization
n	Refractive Index
n_e	Extraordinary Refractive Index
n_o	Ordinary Refractive Index
p	Pressure
P_2	Orientational Order Parameter
q	Scattering wave vector
r_p	Complex Reflectivity p-polarization
r_s	Complex Reflectivity s-polarization
ρ	Particle Density
$\rho(\mathbf{r})$	Charge Distribution
ρ_r	Complex reflectance ratio
T	Temperature
t	Time
τ	Reorientational time constant
θ	Azimuth
T_c	Critical temperature
T_{ODT}	Order Disorder Transition Temperature
U	Internal Energy
V	Volume
χ	Flory Huggins Interaction Parameter
ω	Angular Frequency

Bibliography

[AB77] Azzam R. M. A., Bashara N. M.: *Ellipsometry and Polarized Light*. North-Holland Personal Library, 1977.

[ACN*13] Aissou K., Choi H. K., Nunns A., Manners I., Ross C. A.: Ordered Nanoscale Archimedean Tilings of a Templated 3-Miktoarm Star Terpolymer. *Nano Lett. 13*, 2013, 835–839.

[AGM*04] Abuzaina F. M., Garetz B. A., Mody J. U., Newstein M. C., Balsara N. P.: Birefringence and Depolarized Light Scattering from Ordered Block Copolymers with Anisotropic Distributions of Grain Orientations Produced by Shear Flow. *Macromolecules 37*, 2004, 4185–4195.

[AHD*91] Amundson K., Helfand E., Davis D. D., Quan X., Patel S. S., Smith S. D.: Effect of an electric field on block copolymer microstructure. *Macromolecules 24*, 1991, 6546–6548.

[AHPQ92] Amundson K., Helfand E., Patel S. S., Quan X.: Optical characterization of ordering and disordering of block copolymer microstructure. *Macromolecules 25*, 1992, 1935–1940.

[AHQ*94] Amundson K., Helfand E., Quan X., Hudson S. D., Smith S. D.: Alignment of Lamellar Block Copolymer Microstructure in an Electric Field. 2. Mechanisms of Alignment. *Macromolecules 27*, 1994, 6559–6570.

[AHQS93] Amundson K., Helfand E., Quan X., Smith S. D.: Alignment of Lamellar Block Copolymer Microstructure in an Electric Field. 1. Alignment Kinetics. *Macromolecules 26*, 1993, 2698–2703.

[AWA*04] Angelescu D. E., Waller J. H., Adamson D. H., Deshpande P., Chou S. Y., Register R. A., Chaikin P. M.: Macroscopic Orientation of Block Copolymer Cylinders in SingleLayer Films by Shearing. *Adv. Mater. 16*, 2004, 1736–1740.

[Bar90] Barton A. F. M.: *Handbook of Polymer-Liquid Interaction Parameters and Solubility Parameters*. CRC Press, 1990.

[BBD*07] Berry B. C., Bosse A. W., Douglas J. F., Jones R. L., Karim A.: Orientational order in block copolymer films zone annealed below the order-disorder transition temperature. *Nano Lett. 7*, 2007, 2789–2794.

[BEH*02a] Böker A., Elbs H., Hänsel H., Knoll A., Ludwigs S., Zettel H., Urban V., Abetz A., Müller A., Krausch G.: Microscopic mechanisms of electric-field-induced alignment of block copolymer microdomains. *Phys. Rev. Lett. 89*, 2002, 135502–135504.

[BEH*02b] Böker A., Elbs H., Hänsel H., Knoll A., Ludwigs S., Zettl H., Urban V., Abetz V., Müller A. H. E., Krausch G.: Microscopic Mechanisms of Electric-Field-Induced Alignment of Block Copolymer Microdomains. *Phys. Rev. Lett. 89*, 13, 2002, 135502–135504.

[BEH*03] Böker A., Elbs H., Hänsel H., Knoll A., Ludwigs S., Zettl H., Zvelindovsky A. V., Sevink G. J. A., Urban V., Abetz V., Müller A. H. E., Krausch G.: Electric Field Induced Alignment of Concentrated Block Copolymer Solutions. *Macromolecules 36*, 2003, 8078–8087.

[BF90] Bates F. S., Fredrickson G. H.: Block Copolymer Thermodynamics: Theory and Experiment. *Annu. Rev. Phys. Chem. 41*, 1990, 525–557.

[BFG*14] Bai W., F H. A., Gotrik K. W., Choi H. K., Aissou K., Liontos G., Ntetsikas K., Alexander-Katz A., Avgeropoulos A., Ross C. A.: Thin Film Morphologies of Bulk-Gyroid Polystyrene-block-polydimethylsiloxane under Solvent Vapor Annealing. *Macromolecules 47*, 2014, 6000–6008.

[BIH00] Bellas V., Iatrou H., Hadjichristidis N.: Controlled Anionic Polymerization of Hexamethylcyclotrisiloxane. Model Linear and Mikroarm Star Co- and Terpolymers of Dimethylsiloxane with Styrene and Isoprene. *Macromolecules 33*, 2000, 6993–6997.

[BKE*02] Böker A., Knoll A., Elbs H., Abetz V., Müller A. H. E., Krausch G.: Large Scale Domain Alignment of a Block Copolymer from Solution Using Electric Fields. *Macromolecules 35*, 2002, 1319–1325.

[BLB03] Buxton G. A., Lee J. Y., Balazs A. C.: Computer simulation of morphologies and optical properties of filled diblock copolymers. *Macromolecules 36*, 2003, 9631–9637.

[BMT05] Bockstaller M. R., Mickiewicz R. A., Thomas E. L.: Block copolymer nanocomposites: Perspectives for tailored functional materials. *Adv. Mater. 17*, 11, 2005, 1331–1349.

[BPS92] Balsara N. P., Perahia D., Safinya C. R.: Birefringence detection of the order-to-disorder transition in block copolymer liquids. *Macromolecules 25*, 1992, 3896–1940.

[BQG86] Binning G., Quate C. F., Gerber C.: Atomic Force Microscope. *Phys. Rev. Lett. 56*, 1986, 930.

[BSK*06] Böker A., Schmidt K., Knoll A., Zettl H., Hänsel H., Urban V., Abetz V., Krausch G.: The influence of incompatibility and dielectric contrast on the electric field-induced orientation of lamellar block copolymers. *Polymer 47*, 2006, 849–857.

[BSM*12] Bates C. M., Seshimo T., Maher M. J., J D. W., Cushen J. D., Dean L. M., Blachut G., Ellison C. J., Willson C. G.: Polarity-Switching Top Coats Enable Orientation of Sub-10-nm Block Copolymer Domains. *Science 338*, 2012, 775–779.

[BSR*01] Bakueva L., Sargent E. H., Resendes R., Bartole A., Manners I.: Electronic properties of semiconducting poly(ferrocenylsilane) thin films with vapor-phase iodine diffusion doping. *J. Mater. Sci: Mater. Electron. 12*, 2001, 21–25.

[BT04] Bockstaller M., Thomas E.: Proximity Effects in Binary Block Copolymer/Particle Blends. *Phys. Rev. Lett. 93*, 2004, 166106, 1–4.

[BW59] Born M., Wolf E.: *Principal of optics Electromagnetic theory of propagation interference and diffraction of light.* Cambridge University Press, 1959.

[BYJ*08] Bita I., Yang J. K., Jung Y. S., Ross C. A., Thomas E. L., Berggren K. K.: Graphoepitaxy of self-assembled block copolymers on two-dimensional periodic patterned templates. *Science 321*, 2008, 939–943.

[CIK*97] Chen Z.-R., Issaian A. M., Kornfield J. A., Smith S. D., Grothaus J. T., Satkowski M. M.: Dynamics of Shear-Induced Alignment of a Lamellar Diblock: A Rheo-optical, Electron Microscopy, and X-ray Scattering Study. *Macromolecules 30*, 1997, 7096–7114.

[CK98] Chen Z.-R., Kornfield J. A.: Flow-induced alignment of lamellar block copolymer melts. *Polymer 39*, 1998, 4679–4699.

[CKKP05] Chiu J. J., Kim B. J., Kramer E. J., Pine D. J.: Control of nanoparticle location in block copolymers. *Journal of the American Chemical Society 127*, 14, Apr. 2005, 5036–7.

[CKS*97] Chen Z. R., Kornfield J. A., Smith S. D., Grothaus J. T., Satkowski M. M.: Pathways to macroscale order in nanostructured block copolymers. *Science 277*, 1997, 1248–1253.

[CMR04] Cheng J. Y., Mayes A. M., Ross C. A.: Nanostructure engineering by templated self-assembly of block copolymers. *Nat. Mater. 3*, 2004, 823.

[CNS*14] Choi H. K., Nunns A., Sun X. Y., Manners I., Ross C. A.: Thin Film Knitting Pattern Morphology from a Miktoarm Star Terpolymer. *Advanced Materials 26*, 2014, 2474–2479.

[CRP*03] Cheng J. Y., Rettner C. T., P S. D., Kim H. K., Hinsberg W. D.:. *Adv. Mater. 15*, 2003, 1599.

[CRST06] Cheng J. Y., Ross C. A., Smith H. I., Thomas E. L.: Templated Self-Assembly of Block Copolymers: Top-Down Helps Bottom-Up. *Adv. Mater. 18*, 2006, 2505–2521.

[CRT*03] Cheng J. Y., Ross C. A., Thomas E. L., Smith H. I., Vancso G. J.: Templated Self-Assembly of Block Copolymers: Effect of Substrate Topography. *Adv. Mater. 15*, 2003, 1599–1602.

[Dar07] Darling S. B.: Directing the self-assembly of block copolymers. *Prog. Polym. Sci. 32*, 2007, 1152–1204.

[DH96] Dotera T., Hatano A.: The diagonal bond method: A new lattice polymer model for simulation study of block copolymers. *J. Chem. Phys. 105*, 1996, 8413–8427.

[DK65] Debye P., Kleboth K.: Electrical Field Effect on the Critical Opalescence. *J. Chem. Phys. 42*, 1965, 3155–3162.

[DMS*06] Daoulas K. C., Müller M., Stoykovich M. P., Park S., Papakonstantopoulos Y. J., dePablo J. J., Nealey P. F., Solak H. H.:. *Phys. Rev. Lett. 96*, 2006, 036104.

[DPCGHB98] De Pablo P. J., Colchero J., Gomez-Herrero J., Baro A. M.: Jumping mode scanning force microscopy. *Appl. Phys. Lett. 73*, 1998, 3300–3302.

[DPCL*00] De Pablo P. J., Colchero J., Luna M., Gomez-Herrero J., Baro A. M.: Tip-sample interaction in tapping-mode scanning force microscopy. *Phys. Rev. B 61*, 2000, 14179–14183.

[EK04] Elbs H., Krausch G.: Ellipsometric determination of Flory-Huggins interaction parameters in solution. *Polymer 45*, 2004, 7935–7942.

[EUD*01] Edrington A. C., Urbas A. M., DeRege P., Chen C. X., Swager T. M., Hadjichristidis N., Xenidou M., Fetters L. J., Joannopoulos J. D., Fink Y., Thomas E. L.: Polymer-Based Photonic Crystals. *Advanced Materials 13*, 2001, 421–425.

[FEMK00] Fukunaga K., Elbs H., Magerle R., Krausch G.: Large-scale alignment of ABC block copolymer microdomains via solvent vapor treatment. *Macromolecules 33*, 2000, 947–953.

[FKZ*94] Förster S., Khandpur A. K., Zhao J., Bates F. S., Hamley I. W., Ryan A. J., Bras W.: Complex Phase Behavior of Polyisoprene-Polystyrene Diblock Copolymers Near the Order-Disorder Transition. *Macromolecules 27*, 1994, 6922–6935.

[FL89] Fredrickson G. H., Leibler L.: Theory of Block Copolymer Solutions: Nonselective Good Solvents. *Macromolecules 22*, 1989, 1238–1250.

[FZT*93] Foucher D. A., Ziembinski R., Tang B. Z., Macdonald P. M., Massey J., Jaeger C. R., Vancso G. J., Manners I.: Synthesis, characterization, glass transition behavior, and the electronic structure of high-molecular-weight, symmetrically substituted poly(ferrocenylsilanes) with alkyl or aryl side groups. *Macromolecules 26*, 1993, 2878–2884.

[Gar66] Gardon J. L.: The influence of polarity upon the solubility parameter concept. *Journal of paint technology 38*, 1966, 43–57.

[GBA*14] Girardot C., Böhme S., Archambault S., Salaün M., Latu-Romain E., Cunge G., Joubert O., Zelsmann M.: Pulsed Transfer Etching of PSPDMS Block Copolymers Self-Assembled in 193 nm Lithography Stacks. *Appl. Mater. Interfaces 6*, 2014, 16276–16282.

[GHBM00] Giessibl F. J., Hembacher S., Bielefeldt H., Mannhart J.: Subatomic Features on the Silicon(111)-(7x7) Surface Observed by Atomic Force Microscopy. *Science 289*, 2000, 422–425.

[GHD02] Gemma T., Hatano A., Dotera T.: Monte Carlo Simulations of the Morphology of ABC Star Polymers Using the Diagonal Bond Method. *Macromolecules 35*, 2002, 3225–3237.

[GKCK96] Gupta V. K., Krishnamoorti R., Chen Z.-R., Kornfield J. A.: Dynamics of Shear Alignment in a Lamellar Diblock Copolymer: Interplay of Frequency, Strain Amplitude, and Temperature. *Macromolecules 29*, 1996, 875–884.

[GKKS95] Gupta V. K., Krishnamoorti R., Kornfield J. A., Smith S. D.: Evolution of Microstructure during Shear Alignment in a Polystyrene-Polyisoprene Lamellar Diblock Copolymer. *Macromolecules 28*, 1995, 4464–4474.

[GMCO13] Gopinadhan M., Majewski P. W., Choo Y., Osuji C. O.: Order-disorder transition and alignment dynamics of a block copolymer under high magnetic fields by in situ X-ray scattering. *Phys. Rev. Lett. 110*, 2013, 078301.

[GMY*02] Ginzburg M., MacLachlan M. J., Yang S.-M., Coombs N., Coyle T. W., Raju N. P., Greedan J. E., Herber R. H., Ozin G. A., Manners I.: Genesis of Nanostructured, Magnetically Tunable Ceramics from the Pyrolysis of Cross-Linked Polyferrocenylsilane Networks and Formation of Shaped Macroscopic Objects and Micron Scale Patterns by Micromolding Inside Silicon Wafers. *J. Am. Chem. Soc. 124*, 2002, 2625–2639.

[GPH05] Grigorova T., Pispas S., Hadjichristidis N.: Magnetic field induced orientation in diblock copolymers with one crystallizable block. *Macromolecules 38*, 2005, 7430–7433.

[GR13] Gotrik K. W., Ross C. A.: Solvothermal Annealing of Block Copolymer Thin Films. *Nano Lett. 13*, 2013, 5117–5122.

[GSTAT07] Gunkel I., Stepanow S., Thurn-Albrecht T., Trimper S.: Fluctuation Effects in the Theory of Microphase Separation of Diblock Copolymers in the Presence of an Electric Field. *Macromolecules 40*, 2007, 2186–2191.

[Gur94] Gurovich E.: On Microphase Separation of Block Copolymers in an Electric Field: Four Universal Classes. *Macromolecules 27*, 1994, 7339–7362.

[HBAKR15] Hannon A. F., Bai W., Alexander-Katz A., Ross C. A.: Simulation methods for solvent vapor annealing of block copolymer thin films. *Soft Matter 11*, 2015, 3794–3805.

[HC04] Hamley I. W., Castelletto V.: Small-angle scattering of block copolymers in melt, solution and crystal states. *Prog. Polym. Sci. 29*, 2004, 909–948.

[HCLB98] Huang C., Chapman B. R., Lodge T. P., Balsara N. P.: Quantifying the "Neutrality" of Good Solvents for Block Copolymers: Poly(styrene-b-isoprene) in Toluene, Benzene, and THF. *Macromolecules 31*, 1998, 9384–9386.

[HDA02] Huynh W. U., Dittmer J. J., Alivisatos A. P.: Hybrid nanorod-polymer solar cells. *Science 295*, 2002, 2425–2427.

[HDTM07] Hayashida K., Dotera T., Takano A., Matsushita Y.: Polymeric Quasicrystal: Mesoscopic Quasicrystalline Tiling in ABC Star Polymers. *Physical Review Letters 98*, 2007, 195502.

[HHG*11] Hong S. W., Huh J., Gu X., Lee D. H., Jo W. H., Park S., Xu T., Russell T. P.: Unidirectionally aligned line patterns driven by entropic effects on faceted surfaces. *PNAS 109*, 2011, 1402–1406.

[HI93] Hadjichristidis N., Iatrou H.: Morphology and Miscibility of Miktoarm Styrene-Diene Copolymers and Terpolymers. *Macromolecules 26*, 1993, 5812–5815.

[HKT*06] Hayashida K., Kawashima W., Takano A., Shinohara Y., Amemiya Y., Nozue Y., Matsushita Y.: Archimedean Tiling Patterns of ABC Star-Shaped Terpolymers Studied by Microbeam Small-Angle X-ray Scattering. *Macromolecules 39*, 2006, 4869–4872.

[HL98] Hanley K. J., Lodge T. P.: Effect of dilution on a block copolymer in the complex phase window. *J. Polym. Sci., Part B: Polym. Phys. 36*, 1998, 3101–3113.

[HT72] Helfand E., Tagami Y.: Theory of the interface between immiscible polymers. II. *J. Chem. Phys. 56*, 1972, 3592.

[HTF97] Hashimoto T., Tsutsumi K., Funaki Y.: Nanoprocessing Based on Bicontinuous Microdomains of Block Copolymers: Nanochannels Coated with Metals. *Langmuir 13*, 1997, 6869–6872.

[HUM99] Hong K., Uhrig D., Mays J. W.:. *Current Opinion in Solid State and Materials Science 4*, 1999, 531–538.

[ISK*05] Imai M., Sakai K., Kikuchi M., Nakaya K., Saeki A., Teramoto T.: Kinetic pathway to double-gyroid structure. *J. Chem. Phys. 122*, 2005, 214906.

[JBCM03] Jaramillo T. F., Baeck S. H., Cuenya B. R., McFarland E. W.: Catalytic activity of supported Au nanoparticles deposited from block copolymer micelles. *JACS 125*, 2003, 7148–7149.

[JGG*02] Jain A., Gutmann J. S., Garcia C. B. W., Zhang Y., Tate M. W., Gruner S. M., Wiesner U.: Effect of filler dimensionality on the order-disorder transition of a model block copolymer nanocomposite. *Macromolecules 35*, 2002, 4862–4865.

[JHK*13] Jeong J. W., Hur Y. H., Kim H., Park W. I., Kim M. J., Kim B. J., Jung Y. S.: Proximity Injection of Plasticizing Molecules to Self-Assembling Polymers for Large-Area, Ultrafast Nanopatterning in the Sub-10-nm Regime. *ACS Nano 7*, 2013, 6747–6757.

[JJTR08] Jung Y. S., Jung W., Tuller H. L., Ross C. A.: Nanowire Conductive Polymer Gas Sensor Patterned Using Self-Assembled Block Copolymer Lithography. *Nano Letters 8*, 2008, 3776–3780.

[JR07] Jung Y. S., Ross C. A.: Orientation-controlled self-assembled nanolithography using a polystyrene-polydimethylsiloxane block copolymer. *Nano Lett. 7*, 2007, 2046–2050.

[JR09] Jung Y. S., Ross C. A.: Well-Ordered Thin-Film Nanopore Arrays Formed Using a Block-Copolymer Template. *Small 5*, 2009, 1654–1659.

[KBCI*15] Kathrein C. C., Bai W., Currivan-Incorvia J. A., Liontos G., Ntetsikas K., Avgeropoulos A., Böker A., Tsarkova L., Ross

C. A.: Combining Graphoepitaxy and Electric Fields toward Uniaxial Alignment of Solvent-Annealed Polystyrene-b-Poly(dimethylsiloxane) Block Copolymers. *Chem. Mater. 27*, 2015, 6890–6898.

[KBN*15] Kathrein C. C., Bai W., Nunns A., Gwyther J., Manners I., Böker A., Tsarkova L., Ross C. A.: Electric Field induced Morphological Transitions in Thin Films of Metalorganic 3-Miktoarm Star Terpolymers. *Macromolecules*, 2015.

[KFB*95] Khandpur A. K., Förster S., Bates F. S., Hamley I. W., Ryan A. J., Bras W., Almdal K., Mortensen K.: Polyisoprene-Polystyrene Diblock Copolymer Phase Diagram near the Order-Disorder Transition. *Macromolecules 28*, 1995, 8796–8806.

[KHH*08] Kim T. H., Hwang J., Hwang W. S., Huh J., Kim H., Kim S. H., Hong J. M., Thomas E. L., Park C.: Hierarchical ordering of block copolymer nanostructures by solvent annealing combined with controlled dewetting. *Adv. Mater. 20*, 2008, 522–527.

[KHL*02] Knoll A., Horvat A., Lyakhova K. S., Krausch G., Sevink G. J. A., Zvelindovsky A. V., Magerle R.: Phase Behavior in Thin Films of Cylinder-Forming Block Copolymers. *Phys. Rev. Lett. 89*, 2002, 035501.

[KKKB15] Kathrein C. C., Kipnusu W. K., Kremer F., Böker A.: Birefringence Analysis of the Effect of Electric Fields on the Order-Disorder Transition Temperature of Lamellae Forming Block Copolymers. *Macromolecules 48*, 2015, 3354–3359.

[KKM*07] Kim S. O., Kim B. H., Meng D., Shin D. O., Koo C. M., Solak H. H., Wang Q.: Novel complex nanostructure from directed assembly of block copolymers on incommensurate surface patterns. *Adv.. Mater. 19*, 2007, 3271.

[KKP*15] Kim J. M., Kim Y., Park W. I., Hur Y. H., Jeong J. W., Sim D. M., Baek K. M., Lee J. H., Kim M.-J., Jung Y. S.: Eliminating the TradeOff between the Throughput and Pattern Quality of Sub15 nm Directed SelfAssembly via Warm Solvent Annealing. *Adv. Func. Mater. 25*, 2015, 306–315.

[KLL*08] Kalra V., Lee J., Lee J. H., Lee S. G., Marquez M., Wiesner U., Joo Y. L.: Controlling nanoparticle location via confined assembly in electrospun block copolymer nanofibers. *Small 4*, 2008, 2067–2073.

[KM01] Kulbaba K., Manners I.: Polyferrocenylsilanes: Metal-containing polymers for materials science, self-assembly and nanostructure applications. *Macromol. Rapid Commun. 22*, 2001, 711–724.

[KNP07] Kaittanis C., Naser S. A., Perez J. M.: One-step, nanoparticle-mediated bacterial detection with magnetic relaxation. *Nano Letters 7*, 2007, 380–383.

[KPH09] Kim H. C., Park S. M., Hinsberg W. D.: Block copolymer based nanostructures: materials, processes, and applications to electronics. *Chem. Rev. 110*, 2009, 146–177.

[KS02] Kremer F., Schönhals A.: *Broadband Dielectric Spectroscopy.* Springer, Berlin, 2002.

[KSS*03] Kim S. O., Solak H. H., Stoykovich M. P., Ferrier N. J., de Pablo J. J., Nealey P. F.: Epitaxial self-assembly of block copolymers on lithographically defined nanopatterned substrates. *Nature 424*, 2003, 411–414.

[KSZF03] Kyrylyuk A. V., Sevink G. J. A., Zvelindovsky A. V., Fraaije J. G. E. M.: Simulations of electric field induced lamellar alignment in block copolymers in the presence of selective electrodes. *Macromol. Theory Simul. 12*, 7, 2003, 508–511.

[KTK07] Knoll A., Tsarkova L., Krausch G.: Nanoscaling of Microdomain Spacings in Thin Films of Cylinder-Forming Block Copolymers. *Nano Lett. 7*, 2007, 843–846.

[LD95] Lodge T. P., Dalvi M. C.: Mechanisms of Chain Diffusion in Lamellar Block Copolymers. *Phys. Rev. Lett. 75*, 1995, 657–660.

[Lei80] Leibler L.: Theory of microphase separation in block copolymers. *Macromolecules 13*, 1980, 1602–1617.

[LF92] Lodge T. P., Fredrickson G. H.: Optical Anisotropy of Tethered Chains. *Macromolecules 25*, 1992, 5643–5650.

[LHKZ07] Ly D. Q., Honda T., Kawakatsu T., Zvelindovsky A. V.: Kinetic Pathway of Gyroid-to-Cylinder Transition in Diblock Copolymer Melt under an Electric Field. *Macromolecules 40*, 2007, 2928–2935.

[LHKZ08] Ly D. Q., Honda T., Kawakatsu T., Zvelindovsky A. V.: Hexagonally perforated lamella-to-cylinder transition in a diblock copolymer thin film under an electric field. *Macromolecules 41*, 12, 2008, 4501–4505.

[LHKZ09] Ly D. Q., Honda T., Kawakatsu T., Zvelindovsky A. V.: Electric field-induced transitions in perforated lamella of ABA triblock copolymer thin film. *Soft Matter 5*, 23, 2009, 4814–4822.

[LJK*02] Lee H. H., Jeong W.-Y., Kim J. K., Ihn K. J., Kornfield J. A., Wang Z.-G., Qi S.: Orientational Proliferation and Successive Twinning from Thermoreversible Hexagonal –Body-Centered Cubic Transitions. *Macromolecules 35*, 2002, 785–794.

[LJR*06] Lee W., Ji R., Ross C. A., Gösele U., Nielsch K.: Wafer-Scale Ni Imprint Stamps for Porous Alumina Membranes Based on Interference Lithography. *Small 2*, 2006, 978–982.

[LLP04] Landau L. D., Lifshitz E. M., Pitaevskii L. P.: *Electrodynamics of Continuous Media*. Elsevier Butterworth-Heinemann, 2004.

[Loo65] Looyenga H.: Dielectric constants of heterogeneous mixtures. *Physica 31*, 1965, 401–406.

[LPH*13] Ly D. Q., Pinna M., Honda T., Kawakatsu T., Zvelindovsky A. V.: Kinetic pathways of sphere-to-cylinder transition in diblock copolymer melt under electric field. *J. Chem. Phys. 138*, 7, 2013, 074904.

[LPJ*95] Lodge T. P., Pan C., Jin X., Liu Z., Zhao J., Maurer W. W., Bates F. S.: Failure of the dilution approximation in block copolymer solutions. *J. Polym. Sci., Part B: Polym. Phys. 33*, 1995, 2289–2293.

[LPR*12] Liedel C., Pester C. W., Ruppel M., Lewin C., Pavan M. J., Urban V. S., Shenhar R., Bösecke P., Böker A.: Block Copolymer Nanocomposites in Electric Fields: Kinetics of Alignment. *ACS Macro Letters 2*, 2012, 53–58.

[LSP*13] Liedel C., Schindler K. A., Pavan M. J., Lewin C., Pester C. W., Ruppel M., Urban V. S., Shenhar R., Böker A.: Electric-Field-Induced Alignment of Block Copolymer/Nanoparticle Blends. *Small 9*, 2013, 3276–3281.

[LTK10] L. Tsarkova S. G. J. A., Krausch G.: Nanopattern Evolution in Block Copolymer Films: Experiment, Simulations and Challenges. vol. 227 of *Advances in Polymer Science*. 2010, pp. 33–73.

[LZR*08] Li J. K., Zou S., Rider D. A., Manners I., Walker G. C.: Differential Conductivity in Self-Assembled Nanodomains of a Diblock Copolymer Using Polystyrene-block-Poly(ferrocenylethylmethylsilane. *Adv. Mater. 20*, 2008, 1989–1993.

[LZS06] Lyakhova K. S., Zvelindovsky A. V., Sevink G. J. A.: Kinetic pathways of order-to-order phase transitions in block copolymer films under an electric field. *Macromolecules 39*, 8, 2006, 3024–3037.

[Mat98] Matsen M. W.: Cylinder to Gyroid Epitaxial Transitions in Complex Polymeric Liquids. *Physical Review Letters 80*, 20, 1998, 4470–4473.

[Mat06] Matsen M. W.: Converting the nanodomains of a diblock-copolymer thin film from spheres to cylinders with an external electric field. *J. Chem. Phys. 124*, 7, 2006, 74906.

[Mat09] Matsen M. W.: Fast and accurate SCFT calculations for periodic block-copolymer morphologies using the spectral method with Anderson mixing. *Eur. Phys. J. E: Soft Matter Biol. Phys. 30*, 2009, 361–369.

[MB97] Matsen M. W., Bates F. S.: Block copolymer microstructures in the intermediate-segregation regime. *Journal of Chemical Physics 106*, 6, 1997, 2436–2448.

[MEO10] Mauter M. S., Elimelech M., Osuji C. O.: Nanocomposites of vertically aligned single-walled carbon nanotubes by magnetic alignment and polymerization of a lyotropic precursor. *ACS Nano 4*, 2010, 6651–6658.

[MLU*96] Morkved T. L., Lu M., Urbas A. M., Ehrichs E. E., Jaeger H. M., Mansky P., Russell T. P.: Local Control of Microdomain Orientation in Diblock Copolymer Thin Films with Electric Fields. *Science 273*, 1996, 931–933.

[Mor01] Mortensen K.: *Advanced Functional Molecules and Polymers vol. 2: Processing and Spectroscopy.* Overseas Publishers Association, 2001, ch. 8, Structu, pp. 223–269.

[MUY*02] Maldovan M., Urbas A., Yufa N., Carter W., Thomas E.: Photonic properties of bicontinous cubic microphases. *Phy. Rev. B 65*, 2002, 165123, 1–5.

[Nos95] Nose T.: Coexistence curves of polystyrene/poly (dimethylsiloxane) blends. *Polymer 36*, 1995, 2243–2248.

[NRM13] Nunns A., Ross C. A., Manners I.: Synthesis and Bulk Self-Assembly of ABC Star Terpolymers with a Polyferrocenylsilane Metalloblock. *Macromolecules 46*, 2013, 2628–2635.

[OAWT14] Orzechowski K., Adamczyk M., Wolny A., Tsori Y.: Shift of the Critical Mixing Temperature in Strong Electric Fields. Theory and Experiment. *J. Phys. Chem. B 118*, 2014, 7187–7194.

[OF95] Onuki A., Fukuda b.-i.: Electric Field Effects and Form Birefringence in Diblock Copolymers. *Macromolecules 28*, 1995, 8788–8795.

[OHK*06] Olszowka V., Hund M., Kuntermann V., Scherdel S., Tsarkova L., Böker A., Krausch G.: Large scale alignment of a lamellar block copolymer thin film via electric fields: a time-resolved SFM study. *Soft Matter 2*, 2006, 1089–1094.

[OHK*09] Olszowka V., Hund M., Kuntermann V., Scherdel S., Tsarkova L., Böker A.: Electric Field Alignment of a Block Copolymer Nanopattern: Direct Observation of the Microscopic Mechanism. *ACS Nano 3*, 5, 2009, 1091–1096.

[Onu95] Onuki A.: Electric-field effects in fluids near the critical point. *Europhys. Lett. 29*, 1995, 611.

[Orz98] Orzechowski K.: Electric field effect on the upper critical solution temperature. *Chemical Physics 240*, 1998, 275–281.

[OTB09] Olszowka V., Tsarkova L., Böker A.: 3-dimensional control over lamella orientation and order in thick block copolymer films. *Soft Matter 5*, 4, 2009, 812–819.

[PG12] Patrone P. N., Gallatin G. M.: Modeling Line Edge Roughness in Templated, Lamellar Block Copolymer Systems. *Macromolecules 45*, 2012, 9507–9516.

[PHK*04] Peter M., Hempenius M. A., Kooij E. S., Jenkins T. A., Roser S. J., Knoll W., Vancso G. J.: Electrochemically Induced Morphology and Volume Changes in Surface-Grafted Poly(ferrocenyldimethylsilane) Monolayers. *Langmuir 20*, 2004, 891–897.

[PRS*11] Pester C. W., Ruppel M., Schoberth H. G., Schmidt K., Liedel C., van Rijn P., Schindler K. A., Hiltl S., Czubak T., Mays J., Urban V. S., Böker A.: Piezoelectric Properties of Non-Polar Block Copolymers. *Advanced Materials 23*, 2011, 4047–4052.

[PSR*07] Park S., Stoykovich M. P., Ruiz R., Zhang Y., Black C. T., Nealey P. F.: Directed Assembly of Lamellae-Forming Block Copolymers by Using Chemically and Topographically Patterned Substrates. *Adv. Mater. 19*, 2007, 607–611.

[PSR*15] Pester C. W., Schmidt K., Ruppel M., Schoberth H. G., Böker A.: Electric-Field-Induced Order-Order Transition from Hexagonally Perforated Lamellae to Lamellae. *Macromolecules 48*, 17, 2015, 6206–6213.

[PSZ09] Pinna M., Schreier L., Zvelindovsky A. V.: Mechanisms of electric-field-induced alignment of block copolymer lamellae. *Soft Matter 5*, 2009, 970–973.

[PW99] Pereira G. G., Williams D. R. M.: Diblock Copolymer Melts in Electric Fields: The Transition from Parallel to Perpendicular Alignment Using a Capacitor Analogy. *Macromolecules 32*, 1999, 8115–8120.

[PZ08] Pinna M., Zvelindovsky A. V.: Kinetic pathways of gyroid-to-cylinder transitions in diblock copolymers under external fields: cell dynamics simulation. *Soft Matter 4*, 2008, 316–327.

[QW97] Qi S., Wang Z.-G.: On the Nature of the Perforated Layer Phase in Undiluted Diblock Copolymers. *Macromolecules 30*, 1997, 4491–4497.

[RBA*95] Rosedale J. H., Bates F. S., Almdal K., Mortensen K., Wignall G. D.: Order and Disorder in Symmetric Diblock Copolymer Melts. *Macromolecules 28*, 1995, 1429–1443.

[RCPB*05] Rider D. A., Cavicchi K. A., Power-Billard K. N., Russell T. P., Manners I.: Diblock Copolymers with Amorphous Atactic Polyferrocenylsilane Blocks: Synthesis, Characterization, and Self-Assembly of Polystyrene-block-poly(ferrocenylethylmethylsilane) in the Bulk. *Macromolecules 38*, 2005, 6931–6938.

[RG79] Reich S., Gordon J. M.: Electric field dependence of lower critical phase separation behavior in polymerpolymer mixtures. *J. Polym. Sci., Part B: Polym. Phys. 17*, 1979, 371.

[RKD*08] Ruiz R., Kang H., Detcheverry F. A., Dobisz E., Kercher D. S., Albrecht T. R., Pablo J. J., Nealey P. F.: Density multiplication and improved lithography by directed block copolymer assembly. *Science 321*, 2008, 936–939.

[RLM*99] Rockford L., Liu Y., Mansky P., Russell T. P., Yoon M., Mochrie S. G. J.: Polymers on nanoperiodic, heterogeneous surfaces. *Phys. Rev. Lett. 82*, 1999, 2602.

[Roe00] Roe R.-J.: *Methods of X-ray and Neutron Scattering in Polymer Science*. Oxford University Press, 2000.

[RPL*13] Ruppel M., Pester C. W., Langner K. M., Sevink G. J. A., Schoberth H. G., Schmidt K., Urban V. S., Mays J. W., Böker A.: Electric Field Induced Selective Disordering in Lamellar Block Copolymers. *ACS Nano 7*, 2013, 3854–3867.

[RRV*97] Rulkens R., Resendes R., Verma A., Manners I., Murti K., Fossum E., Miller P., Matyjaszewski K.: Ring-Opening Copolymerization of Cyclotetrasilanes and Silicon-Bridged [1]Ferrocenophanes: Synthesis and Properties of Polysilane-Poly(ferrocenylsilane) Random Copolymers. *Macromolecules 30*, 1997, 8165–8171.

[RRZ*07] Ruiz R., Ruiz N., Zhang Y., Sandstrom R. L., Black C. T.: Local Defectivity Control of 2D Self-Assembled Block Copolymer Patterns. *Adv. Mater. 19*, 2007, 2157–2162.

[RZ04] Rzoska S. J., Zhelezny V.: *Nonlinear dielectric phenomena in complex liquids*. Kluwer Academic Publishers: Dodrecht, 2004.

[SBMG80] Sengers J. V., Bedeaux D., Mazur P., Greer S. C.: Behavior of the dielectric constant of fluids near a critical point. *Physica A 104*, 1980, 573.

[SBZ*05] Schmidt K., Böker A., Zettl H., Schubert F., Hänsel H., Fischer F., Weiss T. M., Abetz V., Zvelindovsky A. V., Sevink G. J. A., Krausch G.: Influence of Initial Order on the Microscopic Mechanism of Electric Field Induced Alignment of Block Copolymer Microdomains. *Langmuir 21*, 2005, 11974–11980.

[SCW*04] Shi W. Q., Cui S., Wang C., Wang L., Zhang X., Wang X. J., Wang L.: Single-chain elasticity of poly(ferrocenyldimethylsilane) and poly(ferrocenylmethylphenylsilane). *Macromolecules 37*, 2004, 1839–1842.

[SDS04a] Sundrani D., Darling S. B., Sibener S. J.: Guiding Polymers to Perfection: Macroscopic Alignment of Nanoscale Domains. *Nano Lett. 4*, 2004, 273–276.

[SDS04b] Sundrani D., Darling S. B., Sibener S. J.: Hierarchial Assembly and Compliance of Aligned Nanoscale Polymer Cylinders in Confinement. *Langmuir 20*, 2004, 5091–5099.

[SGL*14] Singer J. P., Gotrik K. W., Lee J., Kooi S. E., Ross C. A., Thomas E. L.: Alignment and reordering of a block copolymer by solvent-enhanced thermal laser direct write. *Polymer 55*, 2014, 1875–1882.

[SGR12] Son J. G., Gotrik K. W., Ross C. A.: High-aspect-ratio perpendicular orientation of PS-b-PDMS thin films under solvent annealing. *ACS Macro Lett. 1*, 2012, 1279–1284.

[SHGC05] Schultz A. J. A., Hall C. K., Genzer J., Carolina N.: Computer simulation of block copolymer/nanoparticle composites. *Macromolecules 35*, 2005, 1060–1071.

[SHT98a] Sioula S., Hadjichristidis N., Thomas E. L.: Direct Evidence for Confinement of Junctions to Lines in a 3 Miktoarm Star Terpolymer Microdomain Structure. *Macromolecules 31*, 1998, 8429–8432.

[SHT98b] Sioula S., Hadjichristidis N., Thomas E. L.: Novel 2-Dimensionally Periodic Non-Constant Mean Curvature Morphologies of 3

Miktoarm Star Terpolymers of Styrene, Isoprene, and Methyl Methacrylate. *Macromolecules 31*, 1998, 5272–5277.

[SKB*96] Schulz M., Khandpur A. K., Bates F. S., Almdal K., Mortensen K., Hajduk D. A., Gruner S. M.: Phase Behavior of Polystyrene-Poly(2-vinylpyridine) Diblock Copolymers. *Macromolecules 29*, 1996, 2857–2867.

[SKD*07] Stoykovich M. P., Kang H., Daoulas K., Liu G., Liu C. C., de Pablo J. J., Muller M., Nealey P. F.: Directed self-assembly of block copolymers for nanolithography: fabrication of isolated features and essential integrated circuit geometries. *ACS Nano 1*, 2007, 168.

[SMK*05] Stoykovich M. P., Müller M., Kim S. O., Solak H. H., Edwards E. W., de Pablo J. J., Nealey P. F.: Directed assembly of block copolymer blends into nonregular device-oriented structures. *Science 308*, 2005, 1442.

[SPR*13] Schoberth H. G., Pester C. W., Ruppel M., Urban V. S., Böker A.: Orientation-Dependent OrderDisorder Transition of Block Copolymer Lamellae in Electric Fields. *ACS Macro Lett. 2*, 2013, 469–473.

[SPS*10] Schmidt K., Pester C. W., Schoberth H. G., Zettl H., Schindler K. A., Böker A.: Electric Field Induced Gyroid-to-Cylinder Transitions in Concentrated Diblock Copolymer Solutions. *Macromolecules 43*, 2010, 4268–4274.

[SSR*08] Schmidt K., Schoberth H. G., Ruppel M., Zettl H., Hänsel H., Weiss T. M., Urban V., Krausch G., Böker A.: Reversible tuning of a block-copolymer nanostructure via electric fields. *Nature Mater. 7*, 2008, 142–145.

[SSS*07] Schmidt K., Schoberth H. G., Schubert F., Hänsel H., Fischer F., Weiss T. M., Sevink G. J. A., Zvelindovsky A. V., Böker A., Krausch G.: Scaling behavior of the reorientation kinetics of block copolymers exposed to electric fields. *Soft Matter 3*, 2007, 448–453.

[SSSB09] Schoberth H. G., Schmidt K., Schindler K. A., Böker A.: Shifting the Order-Disorder Transition Temperature of Block Copolymer Systems with Electric Fields. *Macromolecules 42*, 2009, 3433–3436.

[STA09] Stepanow S., Thurn-Albrecht T.: Statistical mechanical description of liquid systems in an electric field. *Phys. Rev. E 79*, 2009, 41104–41106.

[SYK10] Segalman R. A., Yokoyama H., Kramer E. J.: Graphoepitaxy of Spherical Domain Block Copolymer Films. *Adv. Mater. 104*, 2010, 1152–1155.

[TA03] Tsori Y., Andelman D.: Thin film diblock copolymers in electric field: Transition from perpendicular to parallel lamellae. *Macromolecules 35*, 13, 2003, 5161–5170.

[TADRJ00] Thurn-Albrecht T., DeRouchey J., Russell T. P., Jaeger H. M.: Overcoming Interfacial Interactions with Electric Fields. *Macromolecules 33*, 2000, 3250–3253.

[TADRK02] Thurn-Albrecht T., DeRouchey J., Russell T. P., Kolb R.: Pathways toward Electric Field Induced Alignment of Block Copolymers. *Macromolecules 35*, 2002, 8106–8110.

[TE05] Tompkins H. G., Eugene A. I.: *Handbook of Ellipsometry.* William Andrew Inc., 2005.

[TGH*12] Tavakkoli K. G. A., Gotrik K. W., Hannon A. F., Alexander-Katz A., Ross C. A., Berggren K. K.: Templating Three-Dimensional Self-Assembled Structures in Bilayer Block Copolymer Films. *Science 336*, 2012, 1294–1298.

[TGMB01] Thompson R. B., Grinzburg V. V., Matsen M. W., Balazs A. C.:. *Science 292*, 2001, 2469.

[TGMB02] Thompson R. B., Grinzburg V. V., Matsen M. W., Balazs A. C.:. *Macromolecules 35*, 2002, 1060.

[THD02] Torquato S., Hyun S., Donev A.: Multifunctional composites: optimizing microstructures for simultaneous transport of heat and electricity. *Phy. Rev. Lett. 89*, 2002, 266601, 1–4.

[TPO*11] Tseng Y.-C., Peng Q., Ocola L. E., Elam J. W., Darling S. B.: Enhanced Block Copolymer Lithography Using Sequential Infiltration Synthesis. *J. Phys. Chem. C 115*, 2011, 17725–17729.

[TS14] Tong Q., Sibener S. J.: Electric-Field-Induced Control and Switching of Block Copolymer Domain Orientations in Nanoconfined Channel Architectures. *J. Phys. Chem. C 118*, 2014, 13752–13756.

[Tsa12] Tsarkova L.: Distortion of a Unit Cell versus Phase Transition to Non-bulk Morphology in Frustrated Films of Cylinder-Forming Polystyrene-b-polybutadiene Diblock Copolymers. *Macromolecules 50*, 2012, 7985–7994.

[Tso09] Tsori Y.: Colloquium: Phase transitions in polymers and liquids in electric fields. *Rev. Mod. Phys. 81*, 2009, 1471–1494.

[TTAL03] Tsori Y., Tournilhac F., Andelman D., Leibler L.: Structural changes in block copolymers: Coupling of electric field and mobile ions. *Phys. Rev. Lett. 90*, 14, 2003, 145504.

[TTL03] Tsori Y., Tournilhac F., Leibler L.: Orienting Ion-Containing Block Copolymers Using Ac Electric Fields. *Macromolecules 36*, 2003, 5873–5877.

[TWS*04] Takano A., Wada S., Sato S., Araki T., Hirahara K., Kazama T., Kawahara S., Isono Y., Ohno A., Tanaka N., Matsushita Y.: Observation of Cylinder-Based Microphase-Separated Structures from ABC Star-Shaped Terpolymers Investigated by Electron Computerized Tomography. *Macromolecules 37*, 2004, 9941–9946.

[TZOS07] Tao Y. F., Zohar H., Olsen B. D., Segalman R. A.: Hierarchical nanostructure control in rod-coil block copolymers with magnetic fields. *Nano Lett. 7*, 2007, 2742–2746.

[VAM*98] Vigild M. E., Almdal K., Mortensen K., Hamley I. W., Fairclough J. P. A., Ryan A. J.: Transformations to and from the Gyroid Phase in a Diblock Copolymer. *Macromolecules 31*, 1998, 5702–5716.

[WC96] Williams D. B., Cartner C. B.: *Transmission Electron Microscopy: a textbook for material science.* Plenum Press, 1996.

[WCR08] Wang J. Y., Chen W., Russell T. P.: Influence of interfacial energy on electric-field-induced sphere-to-cylinder transition in block copolymer thin films. *Macromolecules 41*, 19, 2008, 7227–7231.

[WD08] Wu X. F., Dzenis Y. A.: Phase-field modeling of the formation of lamellar nanostructures in diblock copolymer thin films under inplanar electric fields. *Phys. Rev. E 77*, 3, 2008, 31807.

[WF93] Wirtz D., Fuller G. G.: Phase Transitions Induced by Electric Fields in Near-Critical Polymer Solutions. *Phys. Rev. Lett. 71*, 14, 1993, 2236–2239.

[WLBSR06] Wang J. Y., Leiston-Belanger J. M., Sievert J. D., Russell T. P.: Grain rotation in ion-complexed symmetric diblock copolymer thin films under an electric field. *Macromolecules 39*, 24, 2006, 8487–8491.

[WNC*00] Wang H., Newstein M. C., Chang M. Y., Balsara N. P., Garetz B. A.: Birefringence and Depolarized Light Scattering of an Ordered Block Copolymer Melt under Shear Flow. *Macromolecules 33*, 2000, 4185–4195.

[WXLB*06] Wang J.-Y., Xu T., Leiston-Belanger J. M., Gupta S., Russell T. P.: Ion Complexation: A Route to Enhanced Block Copolymer Alignment with Electric Fields. *Phys. Rev. Lett. 96*, 2006, 128301–128304.

[XZGR04] Xu T., Zhu Y. Q., Gido S. P., Russell T. P.: Electric field alignment of symmetric diblock copolymer thin films. *Macromolecules 37*, 7, 2004, 2625–2629.

[XZS*04] Xu T., Zvelindovsky A. V., Sevink G. J. A., Gang O., Ocko B., Zhu Y. Q., Gido S. P., Russell T. P.: Electric field induced sphere-to-cylinder transition in diblock copolymer thin films. *Macromolecules 37*, 18, 2004, 6980–6984.

[YAH05] Yamauchi K., Akasaka S., Hasegawa H.: Blends of a 3-Miktoarm Stra Terpolymer (3-ISD) of Isoprene (I), Styrene (S), and Dimethylsiloxane (D) with PS and PDMS. Effect on Microdomain Morphology and Grain Size. *Macromolecules 38*, 2005, 8022–8027.

[YJ*10] Yang J. K., Jung Y. S., , Chang J. B., Mickiewicz R. A., Alexander-Katz A., Ross C. A., Berggren K. K.: Complex self-assembled patterns using sparse commensurate templates with locally varying motifs. *Nat. Nanotechnol. 5*, 2010, 256–260.

[YSB09] Yan L.-T., Schoberth H. G., Böker A.: Large-Scale Oriented Assembly of Nanoparticles in Diblock Copolymer Templates under Electric Fields. *Macromol. Chem. Phys. 210*, 2009, 1003–1010.

[YSB10] Yan L.-T., Schoberth H. G., Böker A.: Lamellar microstructure and dynamic behavior of diblock copolymer/nanoparticle composites under electric fields. *Soft Matter 6*, 2010, 5956–5964.

[YTH03] Yamauchi K., Takahashi K., Hasegawa H.: Microdomain Morphology in an ABC 3-Miktoarm Star Terpolymer: A Study by Energy-Filtering TEM and 3D Electron Tomography. *Macromolecules 36*, 2003, 6962–6966.

[ZFH*98] Zhao D., Feng J., Huo Q., Melosh N., Fredrickson G. H., Chmelka B. F., Stucky G. D.: Triblock Copolymer Syntheses of Mesoporous Silica with Periodic 50 to 300 Angstrom Pores. *Science 279*, 1998, 548–552.

[ZHC*03] Zhu L., Huang P., Chen W. Y., Weng X., Cheng S. Z. D., Ge Q., Quirk R. P., Senador T., Shaw M. T., Thomas E. L., Lotz B., Hsiao B. S., Yeh F., Liu L.: "Plastic Deformation" Mechanism and Phase Transformation in a Shear-Induced Metastable Hexagonally Perforated Layer Phase of a Polystyrene-b-poly(ethylene oxide) Diblock Copolymer. *Macromolecules 36*, 2003, 3180–3188.

[ZHSV06] Zou S., Hempenius M. A., Schnherr H., Vancso G. J.: Force Spectroscopy of Individual Stimulus-Responsive Poly(ferrocenyldimethylsilane) Chains: Towards a Redox-Driven Macromolecular Motor. *Macromol. Rapid Commun. 27*, 2006, 103–108.

[ZS03] Zvelindovsky A. V., Sevink G. J. A.: Comment on "Microscopic Mechanisms of Electric-Field-Induced Alignment of Block Copolymer Microdomains". *Phys. Rev. Lett. 90*, 4, 2003, 49601.

[ZWM14] Zhuo J., Whittell G. R., Manners I.: Metalloblock Copolymers: New Functional Nanomaterials. *Macromolecules 47*, 2014, 3529–3543.